Terahertz Spectroscopy and Modelling of Biotissue

by

Gretel Markris Png

Bachelor of Engineering (Electrical and Electronics Engineering, First Class Honours),
The University of Edinburgh, Scotland, UK, 1997

Master of Science (Electrical Engineering and Computer Science),
University of California at Irvine, USA, 2003

Thesis submitted for the degree of

Doctor of Philosophy

in

School of Electrical and Electronic Engineering,
Faculty of Engineering, Computer and Mathematical Sciences
The University of Adelaide, Australia

June, 2010

Chapter 6

Terahertz-Based Analysis of Protein Plaques in Biotissue

ONE medically inspired THz spectroscopic application, which emerges from combining the unique protein sensing with the biotissue differentiation capabilities of THz spectroscopy, is the analysis of diseases where an abnormal accumulation of protein occurs in biotissue. One example of such a disease is Alzheimer's disease (AD), where protein plaques ('senile plaques') accumulate in the cerebral cortex of the brain. This Chapter presents a novel study on the use of THz spectroscopy to distinguish between healthy and diseased biotissue samples excised from three regions of the human brain. The samples are neuropathologically diagnosed as containing abnormally high numbers of protein plaques consistent with AD, and are snap-frozen before measurements. Measurement of frozen samples have reduced uncertainties due to the decreased presence of water, aiding in revealing possible collective vibrational modes of the protein plaques in the THz frequency range. Our results show some distinction in the THz absorption spectra, which could be attributed to pathological changes in the diseased tissue.

6.1 Introduction

Among the wide range of medically inspired THz spectroscopic applications presented in Section 4.5, biomolecular protein sensing is one of the most active areas of THz research. It has thus far produced repeatable and promising results when probing the THz resonant signatures of various protein powders and solutions.

A more challenging scenario for THz protein sensing is the detection of protein in complex biological systems, such as biotissue. Terahertz has indeed been shown to be potentially useful as a diagnostic tool for sensing protein changes in freshly excised human biotissue containing basal cell carcinoma (Wallace *et al.* 2006).

Inspired by the promise of the THz carcinoma research, this Chapter aims to use THz protein sensing for diseases where an abnormal accumulation of protein occurs in biotissue. One example is the accumulation of protein plaques ('senile plaques') in the cerebral cortex of the brain due to Alzheimer's disease (AD).

The novelty of the experiments presented in this Chapter is threefold: first is the study of protein plaques in biotissue with THz radiation; second is the use of brain biotissue; third is the measurement of snap-frozen biotissue with THz radiation, requiring the establishment of new experimental protocols separate from those developed in Chapter 5 for fresh and lyophilised samples.

6.1.1 Motivation

Proteins in living organisms must fold in order to carry out their biological function, however some proteins misfold to become unwanted protein deposits. The accumulation of these extracellular deposits in biotissue is part of the natural process of ageing, but an unnaturally rapid accumulation of deposits can occur, resulting in a decline in the function of the biotissue. One class of diseases caused by protein misfolding is amyloidosis; two well known diseases in the family of amyloidoses are Alzheimer's disease (AD) and type II diabetes (Tan and Pepys 1994). In AD, the unwanted protein deposits are commonly referred to as plaques and tangles.

Alzheimer's disease is of particular interest in this Thesis because it lacks a diagnostic tool. Diagnosis of AD is currently made on the *postmortem* identification of high numbers of lesions (plaques and tangles) in the grey matter of cortical brain regions

(Braak and Braak 1990, Morris *et al.* 1996). The development of a non-invasive diagnostic tool for identifying the accumulation of protein plaques during the early stages of AD would greatly improve medical treatment of the disease, hence improving the quality of a patient's remaining lifetime.

In Chapter 9, mathematical models are presented to show that it is plausible to perform *in vivo* THz spectroscopy of the cerebral cortex, but at higher power levels than presently available. Therefore the most readily available analysis techniques at present are *ex vivo* THz spectroscopy of protein plaques in excised biotissue, and the constituents of plaques. Results from these studies will contribute towards expanding our limited understanding of AD pathogenesis.

6.1.2 Objective Summary

This Chapter presents a novel investigation involving THz spectroscopic examination of healthy and diseased snap-frozen human brain biotissue samples taken from three regions of the cerebral cortex. Frozen biotissue is, in theory, ideal because the strong THz resonant activity of liquid water is suspended when frozen (Ashworth *et al.* 2006, Hoshina *et al.* 2009), improving confidence that any resonant activity detected with THz radiation is caused solely by characteristics of the biotissue. Snap-frozen biotissue has the added advantage of containing smaller ice crystals than those in slow-frozen biotissue (frozen in a domestic freezer), thus snap-frozen biotissue samples are expected to suffer from less THz scattering. Results do indeed show differences between healthy and diseased biotissue, however many challenges exist and they will be highlighted in this Chapter.

Since this Chapter reports on THz spectroscopy of protein plaques specific to AD, a brief introduction into the pathogenesis of AD is first presented in Section 6.2. This introduction is necessary in order to interpret the results gained from the THz investigation, which will be presented from Section 6.4 onwards. A short discussion on the nature of the brain biotissue used in this study is also included in Section 6.3 in order to verify the observed results in Section 6.5.

6.1.3 Location of Experimental Work

The THz experiments described in this Chapter were performed at the National T-ray Facility at the University of Adelaide.

6.2 Background of Alzheimer's Disease

Alzheimer's disease (AD) is an age-related, progressive neurodegenerative disorder. Given that the demographic of the developed world has started moving towards a rise in the number of aged individuals ($\geq$ 65 years), the accompaniment of a rise in age-related diseases is expected (Cummings 2003, Willaert and Verhasselt 1998). Alzheimer's disease is of concern because of its prevalence as the main cause of dementia. This is evident in the graph presented in Fig. 6.1; similar findings have been reported in both developed and developing countries (Fratiglioni *et al.* 1999).

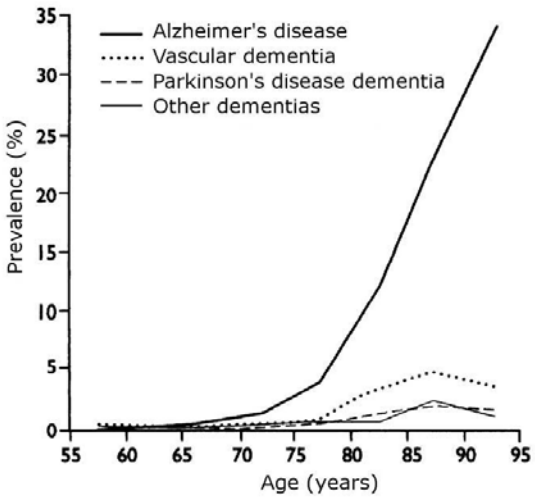

Figure 6.1: Prevalence of AD as the cause of dementia. This graph shows the result of a study conducted on 7528 participants aged between 55 and $\geq$90 years in Rotterdam, The Netherlands. Overall, 72% of all cases of dementia were attributed to AD, 16% were vascular, 6% were Parkinson's, and 5% were other dementia types. After Ott *et al.* (1995).

Alzheimer's disease belongs to a class of diseases called amyloidosis. One characteristic of amyloidosis is protein misfolding, resulting in the formation of insoluble extracellular deposits with fibrillar structures and internal β-pleated-sheets (Booth *et al.* 1997, Näslund *et al.* 2000). Figure 6.2 shows examples of these protein deposits, which are commonly referred to as amyloid-β (Aβ) plaques[57] and tangles in AD. Protein misfolding is elaborated on in the next Subsection.

It should be noted that the accumulation of protein deposits also occurs in other types of dementia. However the type of protein involved, and the location of accumulation can differ between dementia types (Cummings 2003). Table 6.1 highlights the difference between common dementias.

The location where the neuritic protein plaques and tangles accumulate in AD depends on the development stage of the disease. In the early stage, the entorhinal cortex (near the hippocampus) is affected—this region is deep inside the brain. In the middle and

[57] The term amyloid refers to any amorphous, extracellular protein deposit that contains protein fibrils that are 8 to 10 nm in diameter and can aggregate to form β-pleated sheets (Mackenzie 2007).

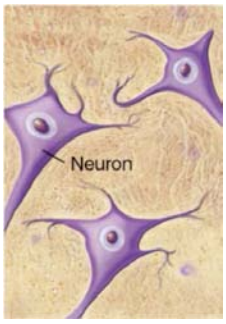

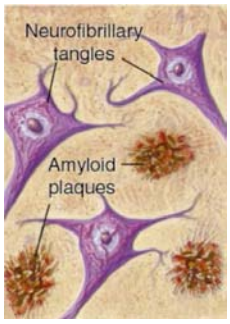

NOTE:
These figures are included on page 171 of the print copy of the thesis held in the University of Adelaide Library.

(a) Schematic of normal cerebral neocortex

(b) Schematic of AD-afflicted cerebral neocortex

(c) Neuritic plaques and neurofibrillary tangles

(d) Neurofibrillary tangle

Figure 6.2: Plaques and tangles. (a and b) Numerous neuritic plaques and tangles are characteristic of an AD-afflicted cerebral neocortex. Extracellular amyloid-β plaques are specific to AD, being one of the major hallmarks of the disease. Intracellular neurofibrillary tangles occupy cell bodies and apical dendrites of neurons, but are not specific to AD (tangles are present in many forms of dementia). After Alzheimer's Disease Research (2000) and Mirra and Hyman (2002); (c) Neuritic plaques with their characteristic amyloid cores, often with radial spikes of fibrillary amyloid. The black scale bar represents 100 μm. After Mackenzie (2007); (d) A neurofibrillary tangle with skein-like (thread-like) appearance. After Mirra and Hyman (2002).

NOTE:
This table is included on page 171 of the print copy of the thesis held in the University of Adelaide Library.

Table 6.1: Examples of human brain diseases caused by protein misfolding and aggregation. Accumulation of protein is common in many types of dementia, but the protein types and the location of accumulation varies as described in this Table. After Selkoe (2003).

late stages, plaques and tangles begin to spread to the uppermost layer of the brain, i.e. the cerebral cortex, or more specifically the neocortex[58].

The cerebral cortex is where neurons and axons are located (Nolte 2002), hence the presence of large numbers of plaques and tangles has a detrimental effect on brain function. More details of plaques and tangles in the neocortex is given in Section 6.3.1. It should be noted that brain atrophy usually follows the middle and late stages of AD, deteriorating the brain further. Brain atrophy will be discussed in Section 6.2.3.

6.2.1 Folding of β-Pleated Sheets

Neuritic plaques have characteristic amyloid cores with amyloid-β fibrillar structures as shown in Fig. 6.3(a). In amyloidosis, proteins with and without β-pleated sheets can misfold to create neuritic plaques (Fändrich *et al.* 2001), making it difficult to identify specific culprit proteins. An example of the difficulty in predicting when proteins will misfold is highlighted in the following two figures.

Fig. 6.3(b) shows lysozyme protein—present in human tears and saliva. Lysozyme contains β-pleated sheets but does not normally have the amyloid-β fibrillar structure. The unfolding and misfolding process of lysozyme is shown in Fig. 6.3(c). Protein folding differs significantly from protein denaturation in that denaturation causes proteins to lose their regular structure (e.g. α-helix segments), resulting in a 'random coil' configuration (stage *iii* of Fig. 6.3(c)). Conversely, proteins form new regular structures through folding and misfolding (e.g. fibrils in stage *v* of Fig. 6.3(c)).

The causes of protein misfolding are known for protein structures that are synthesised *in vitro*. However, the triggers for protein misfolding in the body are not yet known. In Chapter 7, protein misfolding is studied with THz spectroscopy through the use of protein structures that are synthesised *in vitro*.

6.2.2 Diagnosis of Alzheimer's Disease (AD)

Diagnosis of Alzheimer's disease [59] (AD) currently involves a series of tests and evaluations, generally with the intention of eliminating other possible conditions, such as vitamin B_{12} and folate deficiencies (Knopman and Jankowiak 2005). Oral questionnaires,

[58] The structure of the cerebral cortex varies across the brain. The neocortex, which is most visible, covers about 95% of the cerebral cortex (Nolte 2002).

[59] Discovered by Alois Alzheimer in 1906, and formally published in 1907.

NOTE:
This figure is included on page 173
of the print copy of the thesis held in
the University of Adelaide Library.

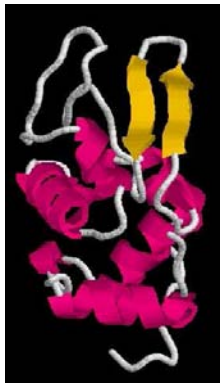

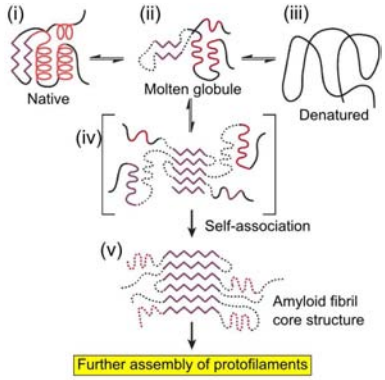

(a) Amyloid-β fibril in AD (b) Native lysozyme molecule (c) Folding of native lysozyme

Figure 6.3: Protein folding process. Cartoon diagrams of proteins obtained from the Protein Data Bank (PDB), and rendered using Rasmol (PDB ID: 1REX and 2BEG). The molecules are coloured according to their secondary structures: β-pleated sheets (yellow), α-helix segments (magenta), and other residues (white). (a) AD plaques have an amyloid core that has a characteristic fibrillar structure as shown by the β-pleated layers (yellow). After Lührs *et al.* (2005); (b) Native lysozyme protein also contains β-pleated sheets (yellow), but these sheets are not arranged like amyloid-β fibrils. After Muraki *et al.* (1996); (c) This schematic shows that lysozyme can misfold to form a core structure of fibrils similar to that of the amyloid-β fibril in AD. This schematic also highlights the difference between protein denaturation and protein folding. The zig-zagged lines correspond to the β-pleated sheets, and the red helices correspond to the α-helix segments. Stages *i-iii* occur during protein denaturation, whereas stages *i-ii-iv-v* occur during protein misfolding. The dotted lines denote undefined structures which may vary from process to process. After Booth *et al.* (1997) and Selkoe (2003).

such as the Mini Mental State Exam (MMSE) (Folstein *et al.* 1975) and the Modified Mini Mental State Exam (3MS) (Teng and Chui 1987), are usually administered to analyse the memory and alertness of a patient. Many other dementia related neuropsychological assessments are available (Fischer *et al.* 2004, Perani 2006), and although these assessments have an accuracy of about 90% in specialised medical centres, their accuracy is still disputed because the questions do not cater to all demographics (Tierney *et al.* 2003, O'Connell *et al.* 2004). The 3MS questionnaire is reproduced in Appendix E together with a list of dementia types.

Although brain imaging scans are often used in the diagnosis of AD, their purpose is also to rule out other possible causes of memory loss. For example, structural neuroimaging techniques such as computed tomography (CT) and magnetic resonance

imaging (MRI) are used to rule out brain tumours, blood clots, and brain atrophy. Functional neuroimaging techniques such as positron-emission tomography (PET) are used to identify brain activity via the uptake of luminous nuclear dye by active regions of the brain.

Since 2004, *in vivo* identification of plaques with PET is possible in humans through *in vivo* staining of plaques via intravenous administration of (N-Methyl-[^{11}C])2-(4'-methylaminophenyl)-6-hydroxy-benzothiazole, or [^{11}C]6-OH-BTA-1—also known as Pittsburgh compound-B, or [^{11}C]PIB (Klunk *et al.* 2004, Nordberg 2004). Note that [^{11}C]PIB, which is a derivative of Thioflavin-T (ThT), is better able to cross the blood-brain-barrier (BBB) than traditional dyes used to stain plaques, such as Congo red, ThT, and Thioflavin-S (Mathis *et al.* 2002, Mathis *et al.* 2003, Bacskai *et al.* 2003). As shown in Fig. 6.4, the ^{11}C radiolabel in [^{11}C]PIB is highly specific and acts as a luminous marker for plaques during a PET scan.

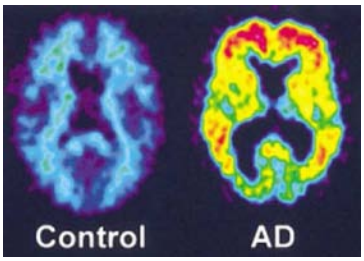

Figure 6.4: Uptake of PIB in healthy and AD-afflicted brains. Positron-emission tomography scans showing the top view of the two brains. Red regions correspond to high PIB uptake by amyloid-β plaques. The red regions are mostly located in the neocortex, which is where plaques are known to accumulate. After Klunk *et al.* (2004).

The use of PET and [^{11}C]PIB for *in vivo* identification of plaques is presently still undergoing human trials, hence is not yet an early diagnostic tool for Alzheimer's disease (Rowe *et al.* 2007, Pike *et al.* 2007). A more cost effective staining chemical based on ^{18}F (^{18}F-BAY94-9172) is also being investigated to replace PIB, which is too expensive for routine clinical use (Rowe *et al.* 2008).

Although PET scanning opens many exciting new possibilities for Alzheimer's disease diagnosis, access to PET equipment is limited due to its cost. In addition, the short half-life of the radiolabelled stains (e.g. 109 minutes for the ^{18}F isotope) means that they need to be delivered daily from cyclotrons (Cyclotek (Aust) Pty Ltd 2009). In Australia for instance, there is an acute shortage of PET scanners nationwide. Furthermore, only selected radiolabelled stains are available at each PET facility. In South Australia, no stains are available for scanning of plaques (Royal Adelaide Hospital 2008), thus patients have to travel interstate (e.g. to Victoria) to undergo PET plaque scans. Magnetic

resonance imaging, being more accessible than PET, is being explored as an alternative, but studies have not progressed beyond the use of animal models (Jack Jr. *et al.* 2005).

The problem of patient access to costly equipment, coupled with the inaccessibility of the brain to probing tools, has led to the search for AD biomarkers in blood and cerebrospinal fluid (CSF) (Qadi and Feldman 2007). The hypothesis is that protein levels in blood and/or CSF circulating around the body may be altered due to the unnatural accumulation of amyloid-β protein (and other proteins) in the brain. Results have shown some success, and immunoassays for detecting proteins related to AD are still being developed (Hampel and Buerger 2006).

The current absence of an AD diagnostic tool means that diagnosis of AD is never 100% certain until a *postmortem* autopsy is performed. The lack of certainty during the patient's life often causes delays in medical intervention as well as planning for the patient's eventual dependence on care givers.

Given the paucity of knowledge on the etiology of AD, any discovery will contribute to the small but growing pool of scientific knowledge that may facilitate advances in diagnosis and treatment of AD.

6.2.3 Atrophy in Brains Afflicted with Alzheimer's Disease

Symmetrical atrophy in both hemispheres of the brain is a common occurrence in AD (Chan *et al.* 2001, Burton *et al.* 2009). Figure 6.5 illustrates the visible differences between normal and AD-afflicted brains.

Diseased brains tend to be lighter in weight than healthy brains, with typical values reported between 0.95 to 1.1 kg compared to $\approx$ 1.3 kg for a healthy brain (Terry and Katzman 1983). Shrinkage in cerebral white matter has been associated to this decrease in weight. The poor condition of many AD brains poses many challenges when extracting biotissue for comparison with normal brains—an example of one such challenge is discussed in Section 6.5.1.

6.3 Background into Brain Samples Used

Human ethics clearance from the University of Adelaide was obtained for this study (approval H/037-2006). Biotissue was received from the South Australian Brain Bank,

NOTE:
These figures are included on page 176 of the print copy of the thesis held in the University of Adelaide Library.

Figure 6.5: Atrophy in an AD-afflicted brain. (a) Lateral view of a normal brain from a 73 year old male donor. The brain weighs 1.371 kg; (b) Medial view of the normal brain shows the compactness of the sulci (grooves) and gyri (ridges). (c) Lateral view of an AD afflicted brain from a 71 year old male donor. The brain weighs 1.063 kg. Comparing the yellow circled region with that of the normal brain, there is clear evidence of wide gaps between the gyri of the AD brain; (d) Medial view of the AD afflicted brain. A comparison of the red circled regions in the normal and AD brains again reveals the wide gaps between the gyri of the AD brain. After Mirra and Hyman (2002).

which is supported by the Australian National Health and Medical Research Council (NH&MRC).

The South Australian Brain Bank[60] (SA Brain Bank) is a repository for the storage of human brains donated for medical research. The majority of donors were patients suffering from neurological and/or psychiatric illnesses. The actual cause of death is only confirmed after *postmortem* autopsies are performed. Figure 6.6 presents an extract from the database of donations made to the SA Brain Bank. It is evident from Fig. 6.6 that the majority of cases are associated with AD. Healthy brains are also donated to the SA Brain Bank but in far fewer numbers than diseased brains.

When a brain is removed from a deceased donor, it is sliced along the coronal plane as shown in Fig. 6.7(a). All slices from one hemisphere of the brain are then fixed and stored in 10% buffered formalin (formaldehyde), while the slices from the other hemisphere are snap-frozen and stored at -80°C. An example of a frozen coronal slice is shown in Fig. 6.7(b).

[60] http://som.flinders.edu.au/FUSA/NEUROSCIENCE/SABrainBank.htm (last accessed: 2009-06-01)

NOTE:
This figure is included on page 177 of the print copy of the thesis held in the University of Adelaide Library.

Figure 6.6: Extract from the database of donations. The column titled 'PMI (hr)' indicates the number of hours between the time of death to the time of tissue fixing in buffered formalin (PMI stands for *postmortem* interval). *Postmortem* neuropathological diagnosis confirms the cause of death. Confidential information that may reveal the identity of donors has been removed.

6.3.1 Pathological Analysis of Biotissue

The two hemispheres of the human brain are bilaterally symmetric: physical and biochemical changes that occur in one hemisphere will also occur in the other hemisphere (Moossy *et al.* 1989, Demeter *et al.* 1989, Arnold *et al.* 1991, Braak and Braak 1991). As a result of bilateral symmetry, only the hemisphere that is fixed in formalin needs to be pathologically analysed to determine the cause of death.

In order to perform pathological examination, standard biotissue preparation techniques are employed in slicing and affixing thin (several micron thick) slices of brain biotissue to microscopic slides. Slicing tools for this purpose have been presented in Section 5.3.1. The regions of the brain examined are chosen to match known areas

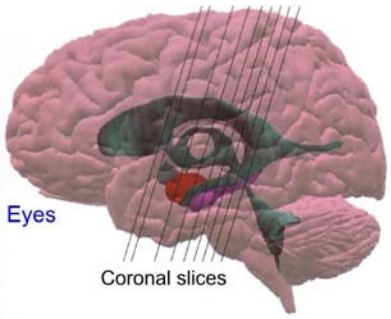

(a) Side view of brain with location of eyes shown

(b) A snap-frozen coronal brain slice

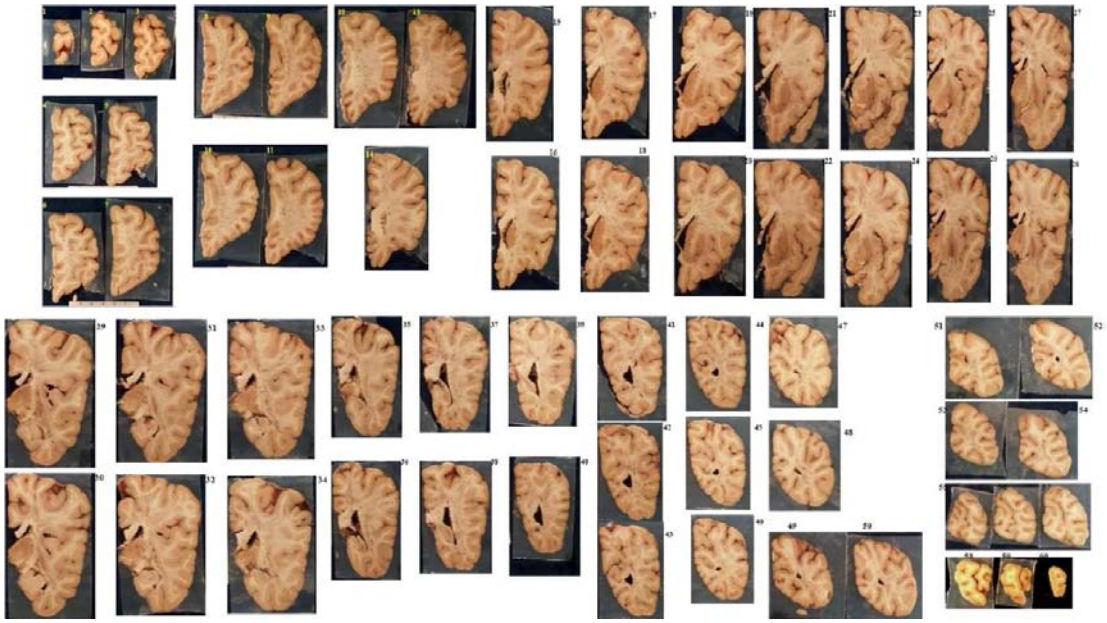

(c) Formalin-fixed coronal slices from the front to the back of brain

Figure 6.7: Coronal brain slices. (a) Upon removal from the deceased donor, both hemispheres of the brain are sliced coronally as shown by the black lines. One hemisphere is then fixed in formalin, while the other hemisphere is snap-frozen. Each formalin fixed coronal slice can therefore be matched to its snap-frozen counterpart. After Nolte and Angevine Jr. (2000); (b) Due to bilateral symmetry in the brain, results from pathological analysis of the formalin half of the brain are applicable to the snap-frozen half; (c) Each coronal slice is labelled, photographed, and individually stored. Photographs courtesy of R. Flook from the SA Brain Bank.

where plaques, tangles and other proteins tend to accumulate. As discussed in Section 6.2, the accumulation of proteins is common to several types of dementia, but the types of protein and the location of accumulation varies with dementia type. Thorough pathological analysis is therefore required to check all possible causes of dementia.

In order to visually identify neurofibrillary tangles, nerve fibres and senile plaques, Bielschowsky silver staining is employed. More detail on Bielschowsky silver staining is found in Litchfield and Nagy (2001). Figure 6.2(c) is an example of how Bielschowsky silver stained biotissue (with plaques) appears under a microscope.

After Bielschowsky silver staining, the number of plaques and tangles are usually graded according to the criterion established by the Consortium to Establish a Registry for Alzheimer's disease or CERAD (Mirra *et al.* 1991), and the Braak and Braak V–VI staging protocols (Braak and Braak 1991). To emphasise the grading procedure, extracts from two standard pathology reports are shown in Table 6.2. There is clear evidence that abnormally large numbers of plaques and/or tangles are present in the neocortex of the diseased brain (SA0178); the converse is true for the healthy brain (SA0162). Note that the accumulation of plaques and tangles in the diseased brain is mainly in the neocortex, which is a characteristic of middle and late stage AD.

Although both formalin-fixed and snap-frozen biotissue are available for this study, snap-frozen biotissue is chosen for the following reasons. First, in the discussion presented in Section 4.5.4 formalin cross-links proteins in biotissue. Since this study aims to sense protein plaques, formalin cross-linking is undesirable. Second, as mentioned in Section 6.1.2 snap-frozen biotissue have smaller ice crystals than those in biotissue frozen in a domestic freezer. The smaller ice crystals are expected to cause less THz scattering, and are more transparent to THz than liquid water or formalin. Third, the firmness of snap-frozen biotissue allows for easier handling and slicing than fresh biotissue used in Chapter 5. Finally, a study involving frozen biotissue complements the fresh biotissue study conducted in Chapter 5.

6.4 Sample Preparation

The protocol for preparing the snap-frozen samples for measurements is elaborated on in this Section.

6.4.1 Identifying Brain Regions

In order to maximise the chances of THz radiation illuminating plaques in the brain samples, regions of the brain where large numbers of plaques reside need to be identified. As described in Section 6.3.1, bilateral symmetry of the brain hemispheres

Cortical Region	Report
Brain Bank No: SA0162	
Right superior, middle and inferior frontal gyri	Normal for age. The Bielschowsky silver stains show no plaques and tangles.
Right cingulate gyrus	Normal. The Bielschowsky silver stain shows no plaques or tangles.
Right amygdaloid nuclei	Normal. The Bielschowsky silver stain shows no plaques or tangles.
Right hemi-medulla	Prominent neuroaxonal spheroids in the gracile and cuneate nuclei consistent with age.
Conclusion	Normal brain and spinal cord for age.
Brain Bank No: SA0178	
Left superior frontal gyrus, left middle frontal gyrus and left inferior frontal gyrus	Severe cortical atrophy with diffuse cortical neuronal loss, reactive gliosis and status spongiosus. The Bielschowsky silver stains show numerous neuritic plaques (type C on NIA-Reagan criteria). Approximately 102 senile plaques per $\times$250 filed are noted in some areas. Numerous neurofibrillary tangles are present.
Left cingulate gyrus	Cortical atrophy with diffuse neuronal loss and reactive fibrous gliosis. No cortical Lewy bodies. The Bielschowsky silver stain shows numerous plaques and tangles.
Right amygdaloid nuclei	The Bielschowsky silver stain shows numerous neuritic plaques (up to 22 per $\times$250 field) and numerous neurofibrillary and tangles.
Left hemi-medulla	Prominent neuroaxonal spheroids in the gracile and cuneate nuclei. Normal for age.
Left hemi-midbrain	Mild neuronal loss of the pigmented neurons of the substantia nigra. No Lewy bodies.
Left hemi-pons	Several neuronal loss pigmented neurons of the locus coeruleus. No Lewy bodies.
Conclusion	Alzheimer's disease according to Khachaturian and CERAD criteria. High likelihood Alzheimer's disease according to NIA-Reagan criteria. Braak & Braak stage 6.

Table 6.2: Microscopic Brain Report. Verbatim extracts of *postmortem* pathological reports from the Institute of Medical and Veterinary Science (IMVS) for two donor brains: healthy (SA0162) and diseased (SA0178). The pathological analysis looks for physical evidence of known neurological disorders. For example, the analysis of brain SA0178 identifies that Lewy bodies are absent but numerous plaques and tangles consistent with Alzheimer's disease are present. This observation leads to the determination that Alzheimer's disease is the cause of death.

Case number	Gender	Age (years)	Diagnosis	Region	PMI (hrs)	Run
SA0090	Female	70	AD	CG, IFG, SFG, MFG, IG	17	1
SA0154	Female	76	AD	CG, IFG, SFG, MFG, IG	23	1
SA0199	Male	80	AD and hippocampal sclerosis	CG, IFG, SFG, MFG, IG	6	1
SA0096	Female	73	Normal	CG, IFG, SFG, MFG, IG	48	1
SA0098	Male	63	No AD; cerebrovascular amyloidosis	CG, IFG, SFG, MFG, IG	38.5	1
SA0178	Female	55	AD	CG, IFG, SFG	23	2
SA0162	Male	72	Normal	CG, IFG, SFG	30	2

Table 6.3: List of cases used in this study. Three healthy brains and four diseased brains are used in this study. Samples are taken from from both male and female donors. As will be seen in Section 6.5, samples in run 1 are 2.41±0.05 mm thick; samples in run 2 are slightly thicker at 3.1±0.6 mm.

means that suitable cortical regions in the snap-frozen half can be identified by cross-referencing against the pathological report for the formalin fixed half. Referring to Table 6.2, the left formalin-fixed superior frontal gyrus, middle frontal gyrus, and inferior frontal gyrus of the diseased brain (SA0178) contain numerous plaques, with some areas having approximately 102 plaques per ×250 microscope magnification field. Due to bilateral symmetry, the same cortical regions in the snap-frozen right hemisphere can be assumed to also have numerous plaques.

Based on pathological reports, three healthy brains and four diseased brains are used in this study. All diseased brains available for this study have large numbers of plaques in the following cortical regions: the superior frontal gyrus (SFG), the inferior frontal gyrus (IFG), the cingulate gyrus (CG), the middle frontal gyrus (MFG), and the insular gyrus (IG). Four of these five regions are as highlighted by the blue text in Fig. 6.8. A summary of all seven brains is given in Table 6.3.

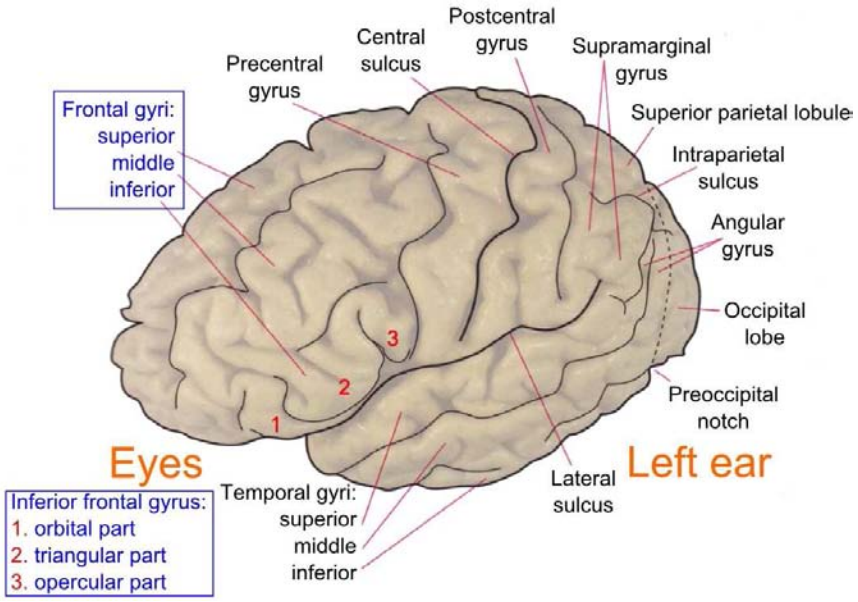

(a) Left hemisphere of the brain

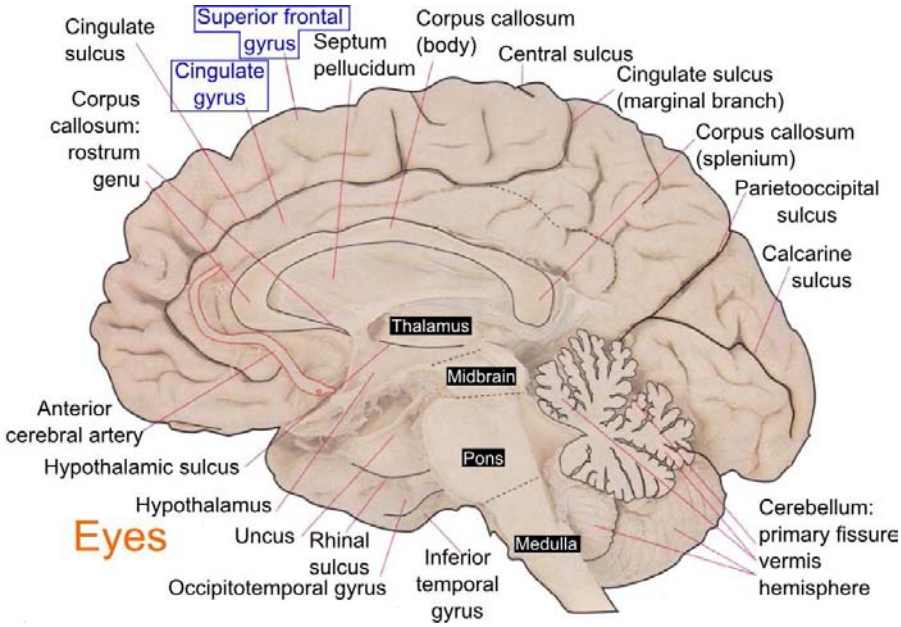

(b) Right brain hemisphere viewed from the left ear

Figure 6.8: Annotated views of the left and right brain hemispheres. Arrows with blue annotations point to regions of the brain where samples have been extracted for use in this study. These regions are all in the neocortex, which is where neuritic plaques and tangles associated with AD have been observed to accumulate during middle and late stages of the disease. The cingulate gyrus (CG) is located on the narrow bridge that connects the two hemispheres. The insular gyrus (IG) is hidden behind the opercular part of the inferior frontal gyrus. After Nolte and Angevine Jr. (2000).

6.4.2 Extraction of Biotissue

As described in Section 6.2, plaques and tangles in AD accumulate in the neocortex. The neocortex consists entirely of grey matter which has abundant blood supply, hence the neocortex has a pinkish-grey colouring (Nolte 2002) as shown in Fig. 6.9(a).

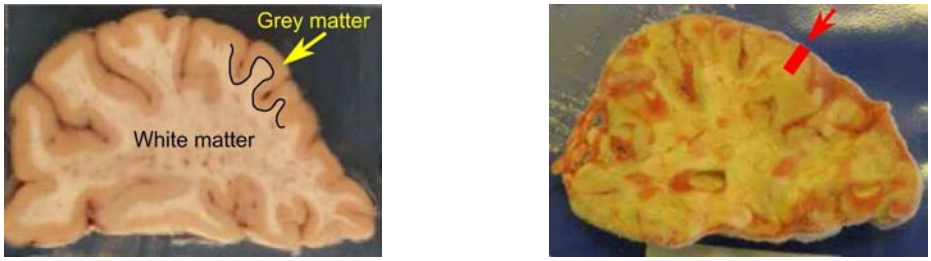

(a) Delineation between grey and white matter (b) Extraction site

Figure 6.9: Snap-frozen brain slice. (a) Blood supply in the grey matter gives it a pinkish-grey hue. Plaques and tangles only accumulate in grey matter; (b) Schematic of where a core is extracted relative to the rest of a brain slice; each core contains both grey and white matter. Original photographs courtesy of R. Flook from the SA Brain Bank.

The thickness of grey matter is reported as being between 1.5 and 4.5 mm; this large variation exists between measurements made from autopsies and those made *in vivo* using magnetic resonance imaging (Meyer *et al.* 1996, Fischl and Dale 2000, MacDonald *et al.* 2000, Nolte 2002, Fatterpekar *et al.* 2002, Narr *et al.* 2005). Direct measurement of grey matter in this study can only be approximated because in the snap-frozen state, it is not possible to confidently delineate between grey and white matter. Since excised biotissue used in this study are from autopsies, the thickness of grey matter is taken as 3.4 ± 0.3 mm based on values reported in Fischl and Dale (2000) and MacDonald *et al.* (2000). This thickness is important later in determining the width of the slicing tool.

Since grey matter is the sole region of interest in this study, only a very small quantity of tissue is needed from each brain slice. However, the snap-frozen slices are too firm to allow slicing of the grey matter. Thawing an entire slice is not an option because the freeze-thaw-freeze cycle may damage the slice, wasting valuable tissue not needed in this study. To prevent damage and to minimise wastage, each snap-frozen slice is seated on a dry ice bed to maintain the biotissue in optimal condition. A slow-speed trepanning drill with a 7 mm diameter hollow drill bit is then used to extract cores. A schematic of a core with respect to the slice is shown in Fig. 6.9(b); examples of drill bits and the drill are as shown in Figs. 6.10(a) and 6.10(b).

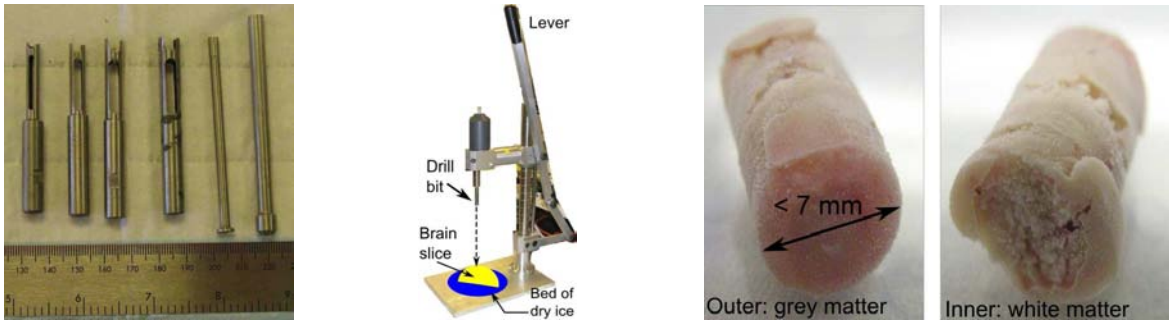

(a) Hollow drill bits (b) Drill for core extraction (c) Two views of a brain core

Figure 6.10: Extraction of cores from a snap-frozen brain slice. (a) Hollow drill bits of various diameters; the two metal rods on the right are used to push the brain cores out of the drill bits; (b) Drill used for core extraction; illustration shows the position of the bed of dry ice on which each brain slice sits; (c) The pinkish end of a core indicates grey matter whereas the paler end is the white matter. Only grey matter is of interest in this study. Original photographs for Figs. 6.10(a) and 6.10(b) courtesy of R. Flook from the SA Brain Bank.

The excised brain cores are approximately 15 mm in length and < 7 mm in diameter. As shown in Fig. 6.10(c), the end of the core where grey matter resides has a pinkish hue. The other end of the core has quite a rough surface because it is where the core is detached from the rest of the slice during excision. This rough end is also paler in colour because it consists of white matter. The excised core is longer than necessary but this length is the minimum length that can be excised without damaging the core and the brain slice.

Cores from healthy brains are also excised at the same five cortical regions to provide a control set of healthy brain cores for THz measurement and comparison.

Core excision is performed at the South Australian Brain Bank at Flinders University. Immediately after excision, each core is placed inside a marked test-tube and stored in a -80°C freezer. To transport the cores to the THz laboratory 25 km away, the cores are packed in an insulated box packed with dry ice (-79°C). The cores are then temporarily stored in a -80°C freezer at the Royal Adelaide Hospital's morgue, which is across the road from the THz facility. Prior to THz measurements, the cores are transported from the morgue in an insulated box packed with dry ice. The cores remain in the insulated box until the time of measurement; dry ice is replaced as necessary.

6.4.3 Slicing Tools

Since only the grey matter is of interest, excess white matter needs to be removed. As shown in Fig. 6.10(c), the surface of the grey matter is not flat because of the undulating surface of the neocortex. To reduce scattering of the incident THz radiation, a thin sliver of the neocortex's outer layer also needs to be removed.

Given that each core is dimensionally small and that the temperature gradient between its -80°C storage environment and room temperature is large, thawing occurs quickly once a core is placed at room temperature; slicing needs to be carried out quickly so as not to thaw out the cores completely.

In Section 5.3.1, a custom-built slicer consisting of two razor blades was introduced and shown in Figs. 5.6(a) and 5.6(b). The slicer's cutting width is easily adaptable by choosing washers of appropriate thickness. Furthermore the slicer is easy to use, allowing for fast slicing. By choosing washers that are slightly less thick than the average thickness of grey matter (3 mm based on the 1.5–4.5 mm range), small disk of grey matter can be sliced from the original 15 mm brain cores.

Figure 6.11 shows an example of a disk cut with razor blades spaced 2.41 ± 0.05 mm apart. This thickness is chosen because it is the minimum that allows easy slicing and handling of the disks. The disks are stored in dry ice until just prior to their transfer onto the sample mount. The next Subsection describes how the disks are mounted and measured.

6.4.4 Mounting Snap-Frozen Biotissue for Measurement

Terahertz measurements are performed on a Picometrix T-ray 2000 THz-TDS system in conjunction with a Janis CCS-450 closed-cycle cryostat enclosed inside a nitrogen-purged chamber.

The system, as shown in Fig. 6.12, operates in transmission-mode and receives ultrafast near-infrared laser pulses (pulsewidth = 90 fs, λ = 800 nm) from a Spectra-Physics Mai Tai laser. The nitrogen chamber shown in this Figure is different from the one used in the experiment; to accommodate the cryostat (which is positioned where the iris is located), the nitrogen chamber used in this study has a U-shaped groove cut into one of the side walls.

(a) View of brain disk laying flat on a dish (b) Side view of brain disk

Figure 6.11: Two views of brain disks. To reduce exposure of the disks to room temperature, photographs are only taken after THz measurements are made. (a) Multiple blood vessels, visible as red spots on the disk, are proof that grey matter is present. Frost formation is evident on the surface of the disk; (b) The disk stands on its side during THz measurements. This position is used because surfaces which encounter the incoming and outgoing THz beam are flat, minimising scattering. The space between the razor blades of the slicing tool is 2.41±0.05 mm.

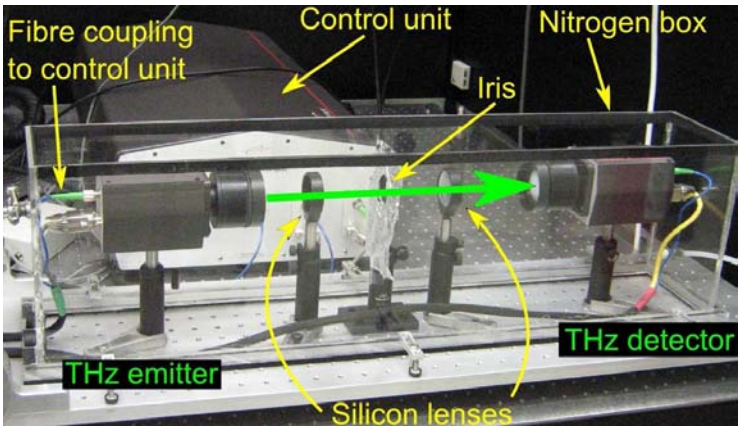

Figure 6.12: Picometrix T-ray 2000 System with a nitrogen-purged chamber. The actual nitrogen chamber used in this study has a U-shaped outlet in the side wall for fitting the cryostat head. The Picometrix system has a pair of fibre-coupled THz emitter-detector heads that operate in the same manner as a THz PCA system shown in Section 3.1.1. The delay stage, pump path and probe path are located inside the control unit. The emitted THz radiation is collimated, hence two silicon lenses are needed to focus the beam; the iris marks the focal point. The width of the THz beam at the focal point is ≈ 4 mm.

The cryostat head shown in Fig. 6.13(a) contains a metal sample mount. The cryostat is aligned so that the sample mount is at the THz focal point (marked by the iris in

Fig. 6.12). Terahertz radiation enters and exits the cryostat via two polyethylene windows. Recalling Fig. 4.12(b), polyethylene is a good window material because it is transparent to THz radiation.

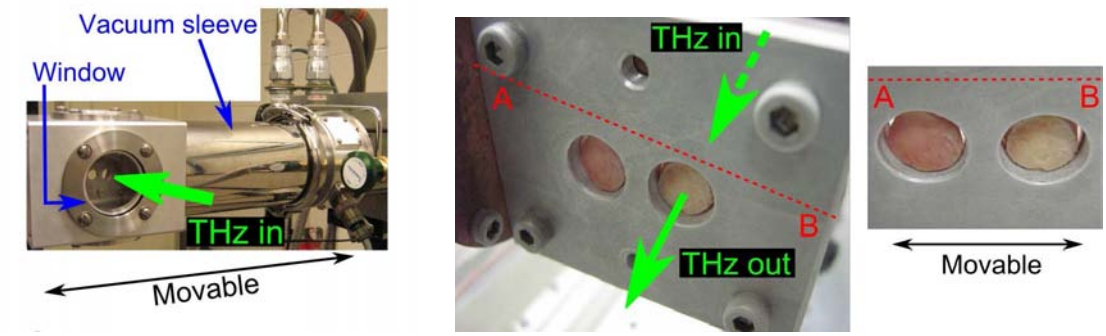

(a) Movable cryostat head with the sample mount

(b) Two views of the sample mount with the cryostat's vacuum jacket removed.

Figure 6.13: THz system setup for measuring brain disks. (a) To show the empty sample holder, a transparent glass window is used in this photograph. The actual windows used during THz measurements are made from polyethylene, which is opaque under visible light but transparent to THz radiation; (b) The disks stand upright on their sides. The movable cryostat head allows two samples to be mounted and measured consecutively, minimising the experiment time.

The cryostat is affixed onto a movable stage, allowing the cryostat head to move sideways. This not only aids in positioning the sample mount at the THz focal point, it also allows two samples to be alternately placed in the THz path. The option of having two samples in the cryostat is tremendously useful because of the long time the cryostat takes to cool down once the vacuum jacket is removed for mounting/removing samples. In this study, the cryostat takes around 50 minutes to cool down to -100°C (173 K) with vacuum evacuation.

The brain disks are mounted upright on their sides as shown in Figs. 6.11(b) and 6.13(b). The THz beam, which has a waist of $\approx$ 4 mm, is directed at the centre of each disk.

The mounting process needs to be very rapid to prevent the disks from thawing, and to prevent the cryostat from heating up excessively once its vacuum jacket is opened. The disks are stored in dry ice until the moment when the vacuum jacket is opened. Once opened, the disks are quickly transferred onto the sample mount with forceps,

and the vacuum jacket closed. Vacuum evacuation is not restored to prevent the disks from lyophilising in a low temperature, low pressure environment (Section 5.5.2).

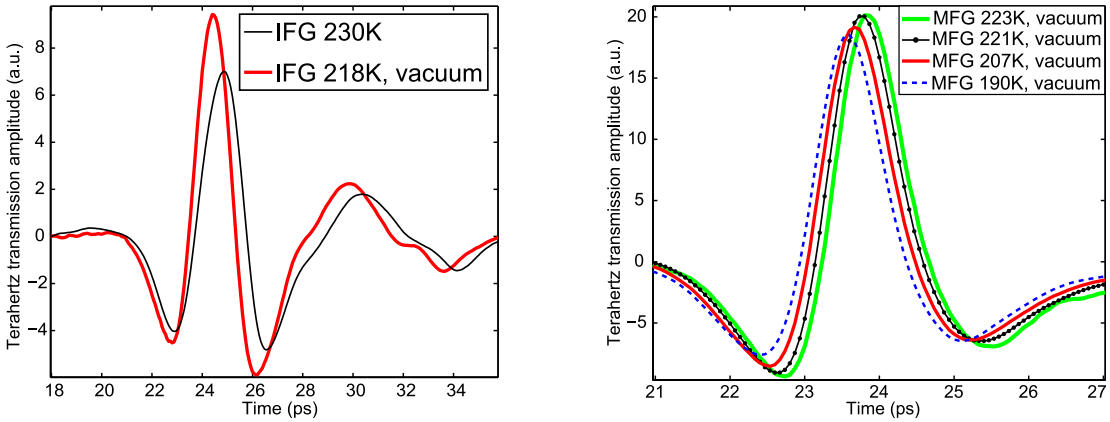

(a) Time domain profiles with and without vacuum evacuation

(b) Changes to the time domain profile with vacuum evacuation over a range of temperatures

Figure 6.14: Effect of vacuum evacuation on brain samples. (a) Vacuum evacuation allows the temperature in the cryostat to fall below 200 K, but causes lyophilisation of the brain sample. It is likely that ice is removed from the sample, which reduces THz scattering from ice crystals and increases the signal amplitude. The absence of ice crystals may also reduce the signal pathlength, hence shifting the time profile; (b) Observation of the detected THz signal from the vacuum evacuated cryostat shows inconsistencies over elapsed time. The signal's amplitude first rises as described in Fig. 6.14(a), but then falls. Since this variation cannot be explained satisfactorily, this study avoids the use of vacuum evacuation.

A comparison of the THz time domain profiles of a brain disk measured with and without vacuum is presented in Fig. 6.14(a). It is evident from this Figure that lyophilisation significantly shifts and increases the sample's THz amplitude, suggesting that ice has been removed from the brain disk. The absence of ice crystals causes less THz scattering by ice crystals, resulting in a stronger detected signal and shorter sample pathlength. However Fig. 6.14(b) presents the effect of lyophilisation over time, showing that the amplitude first increases but then decreases at low temperatures; this fluctuation is unexpected. Since the cryostat is not intended to operate as a lyophiliser, it is possible that the brain disks are not lyophilising consistently, hence lyophilisation is avoided in this study.

Without vacuum evacuation, the temperature of the cryostat rises to -37±10°C (236±10 K). This is the temperature at which THz measurements are made. Although

the measurement temperature is higher than the storage temperature, it is acceptable based on the finding by Ashworth *et al.* (2006) that the THz spectral profile of ice from $\approx$ 0.1–0.8 THz does not vary significantly between -180°C and -3°C (93–270 K). Water activity at -37$\pm$10°C is therefore not expected to interfere with the results reported in this study for the 0.1–0.8 THz frequency range.

6.4.5 Terahertz Data Analysis

The experimental setup of this study is similar to that described in Chapter 5 except that here the THz reference signal is that of the empty cryostat with polyethylene windows. Terahertz data is therefore analysed in the same way as described in Section 5.2.3. Equations (5.21) and (5.22) are used to extract the disks' absorption coefficients and refractive indices respectively. Results are presented in the next Section.

6.5 Results and Discussion

Figure 6.15 presents the THz absorption coefficients of 2.41$\pm$0.05 mm thick brain disks taken from the five regions in the neocortex (CG, IFG, SFG, MFG, and IG). Figure 6.16 presents the THz absorption coefficients of thicker (3.1$\pm$0.6 mm) brain disks taken from three regions in the neocortex (CG, IFG, and SFG). Two thicknesses are used because two sets of slicing tools (as described in Section 6.4.3) are required to maintain sterility over the course of the study. Both thicknesses are within the 3.4$\pm$0.3 mm range specified in Section 6.4.2 for grey matter thickness.

Referring to Fig. 6.15, all diseased tissue appear to have lower THz absorption than healthy tissue—this trend may indicate that the extraneous protein plaques absorb less THz radiation. This finding is surprising as it was expected that the protein plaques will absorb and/or scatter more THz radiation because protein plaques have complex spherical structures with diameters between 4 and 200 μm (Mirra and Hyman 2002), and contain laminated dense bodies of acid phosphatase (Suzuki and Terry 1967).

If the difference in THz absorption between healthy and diseased tissue is indeed due to the extraneous protein plaques, then the question arises as to whether the observed changes are due to specific protein(s) in plaques, or if several proteins collectively influence the changes. The varieties of known abnormal proteins present in AD are

amyloid-β, lipofuscin, tau, and glial fibrillary acidic protein (GFA) (Selkoe 2001). Comparing the diameter of protein plaques (4–200 μm) with the THz wavelength (λ = 3 mm to 300 μm for frequency = 0.1–1 THz), it is not possible to probe individual protein plaques as they are smaller than the THz wavelength. Therefore the observed changes are more likely due to the collective response of the proteins. Furthermore, tissue atrophy is a common occurrence in AD (Section 6.2.3), thus atrophy could have also contributed to the observed differences.

It is noted that the spectra of the healthy tissue in Fig. 6.15 are less smooth than those of diseased tissue. However the THz absorption spectra of healthy tissue in Fig. 6.16 is smoother than those in Fig. 6.15, suggesting that the artefacts in Fig. 6.15 are not unique to healthy tissue. Visual examination of the brain disks used in Fig. 6.15 reveals many blood clots which are likely due to ruptured blood vessels; these clots may scatter THz radiation and contribute to the observed artefacts.

The THz absorption coefficients of healthy CG and IFG tissue in both Figs. 6.15 and 6.16 are consistently higher than that of diseased CG and IFG tissue, however this is untrue for SFG tissue. Other repeat measurements of SFG tissue reveal wildly varying results in that the diseased SFG tissue shows stronger absorption than healthy SFG tissue for some measurements, but not for others. Findings for the SFG tissue are therefore inconclusive; the suitability of THz spectroscopy in examining SFG tissue requires further investigation beyond this Thesis.

There is no agreement in the absorption coefficient values of CG and IFG tissue in Figs. 6.15 and 6.16 even with correct substitution of appropriate sample thickness values in Equation (5.21). The only difference in the samples used in Figs. 6.15 and 6.16 is that they are derived from different donors. The lack of agreement in the absorption coefficient values may imply that the samples are highly variable from donor to donor, hence it is not possible to quantify the extent of THz absorption.

In summary, results show that healthy tissue from the CG and IFG regions of the brain absorb more THz radiation than diseased tissue. The difference in gradients between the THz absorption coefficient plots of healthy and diseased tissue is the only distinguishing feature. The observed difference may be due to the collective frequency responses of known abnormal proteins in AD. Another hypothesis is that tissue atrophy in diseased tissue results in samples that are less dense, hence these samples allow the transmission of more THz than denser healthy tissue.

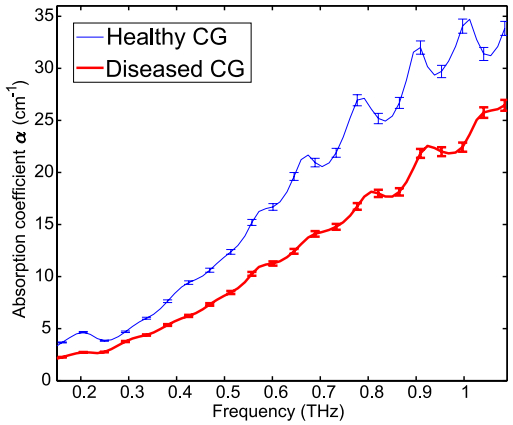

(a) Cingulate gyrus (CG)

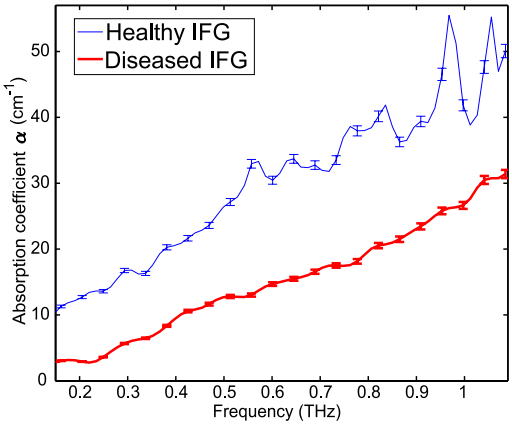

(b) Inferior frontal gyrus (IFG)

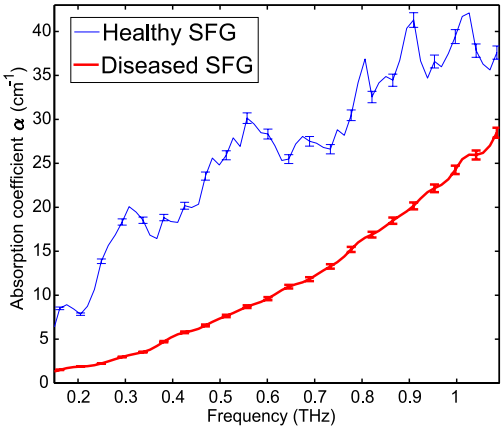

(c) Superior frontal gyrus (SFG)

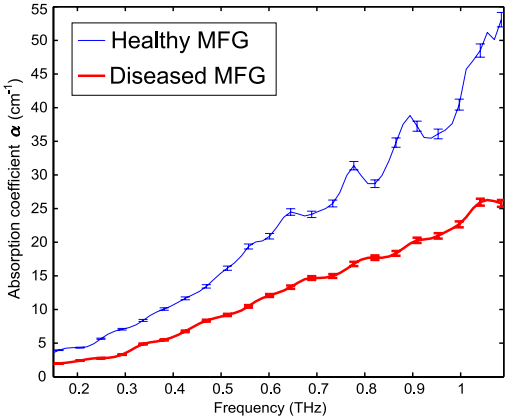

(d) Middle frontal gyrus (MFG)

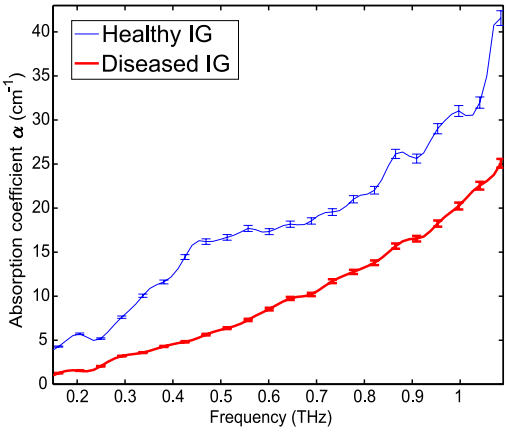

(e) Insular gyrus (IG)

Figure 6.15: THz absorption coefficients $\alpha(\omega)$ of various healthy and diseased brain disks 2.41±0.05 mm thick. The error bars account for the ±0.05 mm uncertainty in sample thickness. All diseased tissue absorb less THz radiation than healthy tissue. This finding is surprising as it was expected that the extraneous proteins in diseased tissue will absorb more THz radiation than healthy tissue. The weaker THz absorption characteristic may also be due to the density of the diseased tissue. Tissue atrophy, which is common in AD-afflicted brains, decreases tissue density.

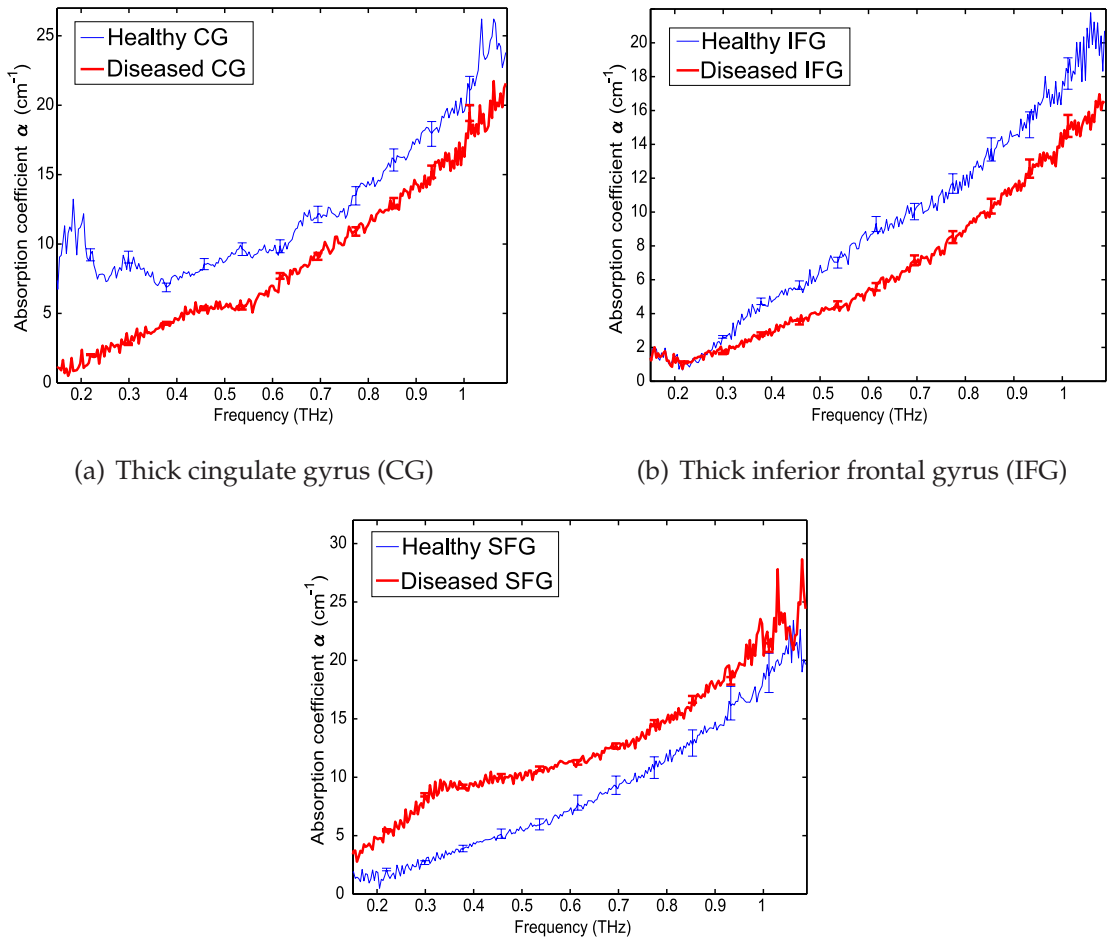

(a) Thick cingulate gyrus (CG)

(b) Thick inferior frontal gyrus (IFG)

(c) Thick superior frontal gyrus (SFG)

Figure 6.16: THz absorption coefficients $\alpha(\omega)$ of various healthy and diseased brain disks 3.1±0.6 mm thick. The error bars account for the ±0.6 mm uncertainty in sample thickness. Separate experiment involving thicker brain disks (CG, IFG, and SFG) from other donors. (a and b) The stronger THz absorption from healthy CG and IFG tissue is consistent with that shown in Fig. 6.15, however the values of $\alpha(\omega)$ does not agree with those in Figs. 6.15(a) and 6.15(b); (c) The absorption characteristic of SFG tissue measured in this experiment does not agree with that observed in Fig. 6.15(c), and this is the only case where the diseased tissue absorbs more THz radiation than healthy tissue.

6.5.1 Challenges

The results observed thus far may be improved if challenges encountered in this study are overcome. This Section highlights these challenges. Remedial action for several of the challenges raised will be proposed in Section 6.6.1.

Handling Issues

Given the small diameter of the brain cores (< 7 mm), minimal handling is paramount so as to reduce thawing caused by heat from contact with fingers/gloves, forceps, dishes, *etc*. This is a particularly difficult endeavour when cutting the cores to ensure flat incident surfaces to the THz signal.

Physical Condition of Brains

Anatomically matching healthy and diseased tissue samples is a challenge due to the poor physical condition of many diseased brains. Moreover the thickness of grey matter can vary on a case by case basis, and may be reduced in AD brains, resulting in a mixture of white and grey matter in a fixed length of core sample.

Healthy brain samples can also be in poor condition due to difficulties encountered during excision. For example, Fig. 6.17 illustrates a poor quality core from the inferior frontal gyrus (IFG). This core is extracted from a brain slice which is structurally weak due to numerous previous core extractions. The length of the core is insufficient for slicing good quality disks. Furthermore large areas of blood clots from ruptured blood vessels are expected to scatter THz radiation, erroneously manifesting in the measurement result as strong THz absorption.

Two images of blood vessels in the neocortex are shown in Fig. 6.18. Although the individual blood vessels are too small to be resolved in the THz frequency range, the abundance of blood vessels means that there may be structural variability between brain cores from different donors.

Measurement Temperature

Water activity is commonly accepted to be suspended completely below -79°C (193 K) (Smith 1961), but this temperature is unattainable in our cryostat without applying a vacuum. As highlighted in Section 6.4.4, vacuum cannot be used as lyophilisation of

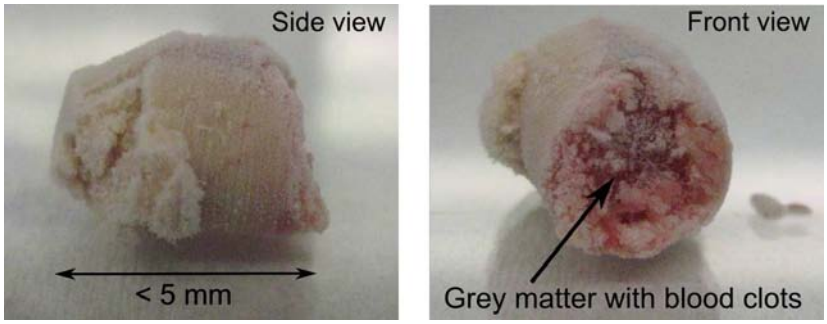

Figure 6.17: Poor quality core from a healthy donor. (Left) Insufficient core length prevents a good quality disk from being sliced; (Right) Large areas of clotted blood from ruptured blood vessels are present on and below the surface of the grey matter.

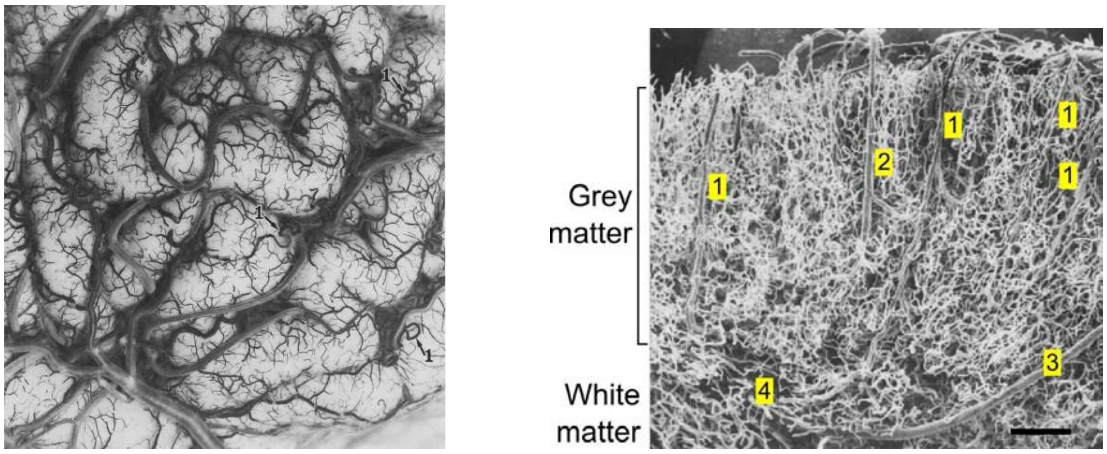

(a) Photograph of blood vessels and veins in the frontal lobe of a 60 year-old donor

(b) SEM of blood vessels, veins and arteries in the temporal pole of a 66 year-old donor

Figure 6.18: Photograph and scanning electron micrograph (SEM) of blood vessels in the neocortex of two male donors. (a) The fine strands are blood vessels; the wider strands are collecting veins and the thickest strands are cerebral veins. After Duvernoy *et al.* (1981); (b) The fine white strands are blood vessels; the wider strands are arteries and veins. The black scale bar represents 500 μm. Note that the blood vessels are packed more tightly in grey matter than in white matter. Regions highlighted in yellow are: (1) cortical arteries, (2) cortical vein, (3) medullary artery, and (4) white matter. After Duvernoy *et al.* (1981) and Nolte (2002).

the samples will occur. Although it is not expected that water activity will interfere with the results reported in this study (as discussed in Section 6.4.4), it is not known if the samples deteriorate or are permanently damaged in the -37$\pm$10°C (236$\pm$10 K) environment.

Small Sample Set

As listed in Table 6.3, the size of the sample set examined in this study is small. The reason for this small sample set is the limited number of brains available for this study. The South Australian Brain Bank has only 52 brains from donors with AD (as of July 2009); many regions in the neocortices are either not available (already used by other researchers), or their conditions are too poor for core extraction. Given the limited number of brains available nationwide, it was also difficult to justify the use of a large number of tissue samples for an exploratory study such as this.

It is not possible to perform statistical analysis of the results with this small sample set. Nonetheless, it is hoped that the early results presented here will aid in facilitating the procurement of more samples in the future so that a more extensive study may be conducted.

6.6 Conclusion

This novel study is a first foray into applying THz spectroscopy in understanding the pathogens and pathogenesis of AD. Early results reported in Section 6.5 are encouraging but many challenges, both experimental and histological as discussed, will need to be overcome before THz spectroscopy can be confidently used to analyse frozen brain tissue. The lessons learnt from this study will aid in developing the next phase of experiments and handling protocols. Discussions are underway with researchers working with AD protein plaques in snap-frozen brain tissue; their recommendations and proposals for future work are reported in the next Subsection.

6.6.1 Future Work

Owing to the challenges highlighted in Section 6.5.1, alternatives to whole brain tissue are sought. One alternative is to lyophilise the brain disks in a lyophiliser such as that described in Section 5.5.3. The lyophilised samples will be more mechanically robust, hence will be easier to handle. Furthermore, the samples can be measured at -80°C (193 K) in vacuum.

Another alternative is to isolate protein plaques through homogenisation of brain tissue. This process involves grinding and centrifuging whole brain tissue in order to

isolate the different components of the tissue, particularly protein plaques (Power *et al.* 2008). This process will aid in removing blood vessels, tissue and other particulate matter which may have interfered with the results in this study. The disadvantage of homogenisation is that large quantities of snap-frozen brain samples are needed.

Both alternatives are motivations for future exploration beyond this Thesis.

6.7 Chapter Summary

Current diagnosis of AD involves tests and evaluations as highlighted earlier in Section 6.2.2. These tests are generally performed with the intention of eliminating other possible medical conditions, such as vitamin deficiencies, blood clots and tumours. Even though PET scanning may in the near future become a diagnostic tool for AD, the coarse resolution of PET imaging ($\approx$ 2–4 mm full width at half maximum[61]) compared to the dimension of a single protein plaque (4–200 μm in diameter) means that diagnosis of AD can only be made in the middle to late stages of the disease when large numbers of plaques clump together in the neocortex (Section 6.2). The chemical triggers of AD and its early stage pathogenesis are still not observable via imaging.

Refinement of THz spectroscopic experiments of biotissue and fluids may one day lead to the discovery of a reliable and cost-effective means of identifying early stage AD (and possibly other diseases) through biomarkers in body fluids. The absence of complex biotissue structures in body fluids is expected to improve THz spectroscopic results, removing uncertainties caused by inextricable vascular bundles, such as blood vessels.

If abnormal levels of proteins associated with AD (e.g. amyloid-β) are present in body fluids, then it is useful to investigate if THz-TDS spectroscopy can indeed identify these proteins. This question is the impetus for the work to be presented in the next Chapter: simple protein microstructures that resemble those in AD are synthesised *in vitro* and examined with THz spectroscopy.

[61] (Judenhofer *et al.* 2008, Mourik *et al.* 2008, Rahmim and Zaidi 2008)

Chapter 7

Terahertz Spectroscopic Differentiation of Biological Microstructure

---

VARIABILITY in biotissue samples creates many challenges to producing consistent and repeatable THz measurements. Uncertainties arise when THz spectroscopy is relied upon to distinguish between biotissue types, such as between diseased and healthy biotissue. When compared to simple biomolecules such as proteins (measured in powdered form), biotissue is extremely complex, consisting of several sub-systems of proteins, lipids, water, *etc*. The collective responses of these sub-systems are sensed in THz spectroscopy, making it difficult to isolate the influence of a specific sub-system of biotissue.

One goal of this Thesis is the use of THz to investigate the pathogenesis of Alzheimer's disease. In the previous Chapter, the collective responses of Alzheimer's disease-related proteins in biotissue were investigated. This Chapter narrows the focus down to one of the alleged pathogens of Alzheimer's disease: protein plaques. The unique β-pleated structure of protein plaques is one of its most distinguishable features, thus this Chapter investigates whether this biological microstructure can be differentiated using THz spectroscopy. The results reveal differences between microstructures, which have several exciting implications for THz spectroscopy.

7.1 Introduction

Chapter 4 describes the work of several authors who have investigated vibrational and tortional modes, and dynamics of proteins and nucleic acids (Markelz *et al.* 2000, Fischer *et al.* 2002, Whitmire *et al.* 2003, Siegrist *et al.* 2006, Markelz *et al.* 2007). Terahertz-TDS has also been used to investigate the phonon resonances in three dimensional (3D) crystalline lattices of small organic molecules (polypeptides and polynucleotides) in various states: denatured, native, hydrated and dry (Zhang *et al.* 2004, Knab *et al.* 2005, Knab *et al.* 2006, Kistner *et al.* 2007). Results show that THz absorption is affected by molecular conformation (Markelz 2008). In addition, THz-TDS has been linked to solvation free energy changes induced by protein folding in bacteriophage λ_{6-85} (Ebbinghaus *et al.* 2008), implying that THz spectroscopy has the potential to indirectly probe protein folding through the examination of induced changes in the protein's hydration shell.

This Chapter explores whether THz spectroscopy can be used to probe uniform microstructures in biological materials. Soft (semi-rigid) microstructures formed by folding and aggregation in proteins are common in nature and in artificial environments. For example, the formation of protein-based 3D soft microstructures has been exploited in the preparation of food products such as cheeses and yoghurt (de Kruif *et al.* 1995). Protein-based 3D soft microstructures are also a type of contaminant in the dairy industry (Mercadé-Prieto and Chen 2006). In humans, the formation and accumulation of unnaturally large numbers of soft protein microstructures in biotissue can cause degenerative diseases such as Alzheimer's and Parkinson's (Selkoe 2003, Näslund *et al.* 2000, Tan and Pepys 1994). The widespread use and occurrence of protein-based soft microstructures make them ideal as a new class of biomaterials to be investigated with THz.

7.1.1 Motivation

One key area for advancing the reliability of THz medical diagnosis is the study of THz interaction with biological matter in the form of their simpler synthetic analogues. By understanding how these simple structures interact with THz, we can then explore more complex structures. Soft protein microstructures are simple synthetic analogues to biotissue and protein plaques introduced previously in Chapters 5 and 6.

The study of soft microstructures is currently limited due to the destructive nature of available investigative tools. For example, staining has been used to detect specific bonds, such as intermolecular β-pleated sheet interactions (Gosal *et al.* 2004a), whereas electron microscopy has been used to visualise microstructures (Gosal *et al.* 2004a, Resch *et al.* 2005). Being generally non-destructive, THz spectroscopy may therefore be a preferred technique for analysing soft microstructures.

7.1.2 Objective Summary

This Chapter presents a novel investigation that examines if THz spectroscopy allows differentiation between three protein microstructures: globular, fine fibrillar, and coarse fibrillar. These microstructures are good reproductions of those found in nature, such as in protein plaques associated with Alzheimer's disease. Results from spectroscopic measurements of thermally induced protein gels show that the type of protein microstructure has a direct influence on measured THz absorption. Globular β-lactoglobulin structures with diameters of 2 μm, and fibrillar structures with diameters less than 0.03 μm, are observed using radiation between 0.8 and 1.5 THz. Results show that the globular structures have a decline in THz transmission when compared to the fibrillar ones. The cause of this decline can be modelled as Rayleigh scattering from the globular microstructures.

Since this Chapter discusses the use of β-lactoglobulin gels, a background review to β-lactoglobulin is first provided in Section 7.2. A review of protein gels is then provided in Section 7.3. This is followed by a description of how β-lactoglobulin gels are synthesised in Section 7.4. Measured results, which are presented in Section 7.6, are accompanied with an in-depth discussion including theoretical verification of the observed results.

7.1.3 Location of Experimental Work

The THz experiments described in this Chapter were performed at the National T-ray Facility at the University of Adelaide.

7.2 Background to Biological Sub-Systems

In Chapter 6, grey matter from donor brains was measured intact with THz radiation. The complex biological composition of diseased grey matter can be divided into three simpler sub-systems: neurons[62], blood vessels, and protein plaques. Variability in the spatial distribution of any of these three sub-systems is expected between brain donors; the influence of such variability on the accuracy of THz measurements is unconfirmed, but is likely to be substantial.

Biological analogues of individual biotissue sub-systems of can be synthesised *in vitro*, allowing the study of one sub-system without interference from others. As these synthesised analogues exist in more controlled and simpler environments than the body (or excised biotissue), they allow researchers to focus on understanding the behaviour of one sub-system, allowing for refinement of experimental techniques. For complex environments such as grey matter, the sub-system approach appears to be favourable for novel investigations such as this one.

Examples of biological analogues relevant to grey matter are the NIH-3T3 cell line for modelling human fibroblast[63], and the PC12 cell line for modelling developing neurons (Bucciantini *et al.* 2002). To model the amyloid-β fibrils in protein plaques, protein aggregation is exploited to encourage protein misfolding, producing fibrillar microstructures indistinguishable from those in protein plaques (Gosal *et al.* 2002, Bromley *et al.* 2005, Krebs *et al.* 2007). These synthesised fibrillar microstructures have ultrastructures and tinctorial properties which are identical to those in natural amyloid-β fibrils. One example of a product created through protein aggregation is fibrillar gels containing β-pleated sheets, as discussed in the next Section.

7.3 Gels Containing β-Pleated Sheets

Fibrillar gels that contain fibrillar microstructures resembling those in amyloid-β fibrils can be synthesised *in vitro* using commercially purchased powdered proteins.

[62] The term *neurons* is used to refer to pyramidal cells (most numerous in the neocortex), and non-pyramidal cells. Dendritic spines and axons emanate from neurons (Nolte 2002).

[63] Fibroblast are cells in connective biotissue.

Examples of such proteins are β-lactoglobulin and lysozyme. This study utilises β-lactoglobulin to produce gels with various 3D microstructures through the manipulation of the gels' acidity. This Section introduces β-lactoglobulin and explains how different microstructures are synthesised.

7.3.1 What is β-Lactoglobulin?

Bovine milk contains the following main components: *(i)* milk fat, *(ii)* casein miscelles, *(iii)* whey proteins, and *(iv)* milk sugar (lactose) as well as salts (de Kruif *et al.* 1995). When milk fat is removed through centrifugation, skimmed milk is obtained. When casein miscelles are removed from skimmed milk, the colloidal liquid that remains is whey protein. Commercial whey protein is available in two forms: whole whey protein isolate (WPI) powder, or separated into its protein constituents consisting of 68% β-lactoglobulin, 17% α-lactalbumin, 7% bovine serum albumin, and 7% immunoglobulin G (Foegeding *et al.* 1992). The abundance of β-lactoglobulin and WPI make them popular choices in thermal gelation studies conducted by the food industry (Paulsson *et al.* 1986, Hudson *et al.* 2000).

Bovine β-lactoglobulin (or β-lg) exists either in its native form, or as one of two variants (β-lg A and B). The native form is used in this study. β-Lactoglobulin is so named because it has a secondary structure of antiparallel β-pleated sheets (Verheul *et al.* 1999) as shown in Fig. 7.1(a); the β-pleated sheet characteristic also exists in other proteins such as native lysozyme as shown in Fig. 6.3(b).

Thermal Gelation

When β-lg is heated above 65–70°C in a solution environment, one of several possible chemical processes occurs depending on the acidity of the solution environment (Hines and Foegeding 1993). Two examples—fibrillar and globular—are shown in Fig. 7.1(b). The heating and chemical changes in β-lg , called *thermal gelation*, results in the production of β-lg gel.

7.3.2 Influence of pH on Microstructure Formation in Gels

The isoelectric point (pI) of a protein is the pH value at which there is no net electrical charge on each individual protein molecule. For β-lg, the pI is reported to be between

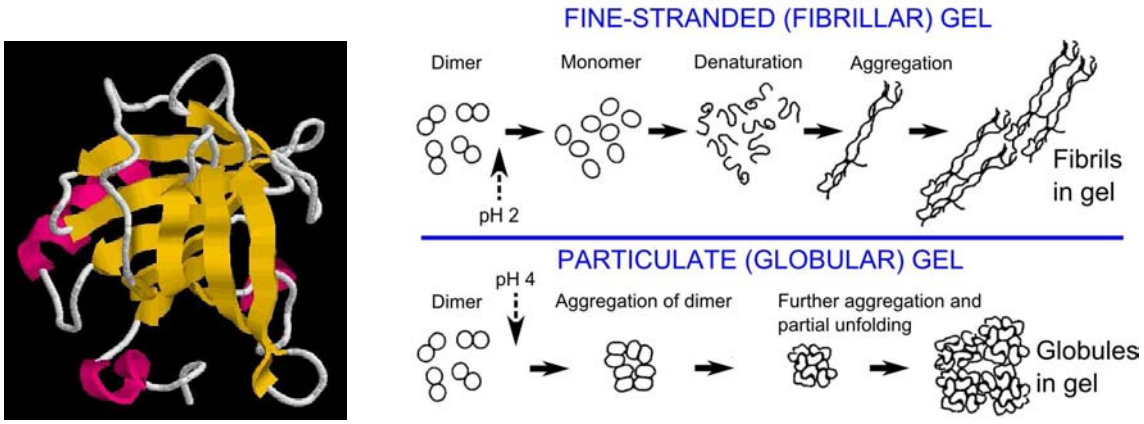

(a) Native β-lg molecule

(b) Formation of fibrillar and globular gels

Figure 7.1: Formation of fibrillar and globular microstructures in β-lg gels. (a) Cartoon diagram of a β-lg molecule obtained from the Protein Data Bank (PDB), and rendered using Rasmol (PDB ID: 1BSY). This molecule is coloured according to its secondary structures: eight antiparallel β-pleated sheets (yellow), α-helix segments (magenta), and other residues (white). After Qin *et al.* (1998). (b) Succession of steps leading to the formation of fibrillar and globular β-lg gels in a solution environment at $>$ 65–70°C. The process starts off with β-lg dimers (a dimer contains two β-lg molecules, each with structure as shown by the cartoon diagram on the left). Depending on the acidity of the solution environment, the dimer aggregates to form either fine fibrils (pH 2) or globules (pH 4). Coarse fibrils are formed at pH 7. Adapted from Lefèvre and Subirade (2000).

pH 4.8 and 5.1 (Bromley *et al.* 2005, Krebs *et al.* 2007). When β-lg protein is immersed in an aqueous environment, the acidity of this environment can be manipulated to be close to or away from β-lg's pI, resulting in manipulation of the net charge on each individual protein molecule. For example, at pH 2 the net charge is +20 (unitless); this large net charge affects the oligomerisation[64] process in β-lg such that more monomers than dimers exist (Bromley *et al.* 2005, Verheul *et al.* 1999). This oligomerisation condition, which also exists above pH 6 (Kavanagh *et al.* 2000), favours the formation of fibrillar microstructures during thermal gelation as illustrated in Fig. 7.1(b). Furthermore, the presence of large numbers of β-lg monomers causes the β-lg solution to appear visually clear at pH values away from its pI, which is between pH 4.8 and 5.1 as highlighted above.

[64]Oligomerisation is a chemical process in which a monomer unit is repeated in limited numbers and linked to become a more complex structure. Oligomerisation differs from polymerisation in that the monomer unit is repeated without limit during polymerisation.

Conversely, when the pH of the solution is close to the pI, there is only a small net charge on each molecule, resulting in the presence of more dimers than monomers after oligomerisation. These dimers can also associate to form larger oligomers called octamers (Verheul *et al.* 1999). This condition favours the formation of globular microstructures during thermal gelation as illustrated in Fig. 7.1(b). Additionally, the presence of large numbers of β-lg dimers causes the β-lg solution to appear turbid at pH values close to its pI.

Examples of fibrillar and globular microstructures are presented in Figs. 7.2–7.3. There is a clear visual distinction between fibrillar and globular microstructures: globular microstructures resemble balls whereas fibrils resemble strands. Fibrils synthesised at pH 2 are fine and 'worm-like' whereas those synthesised at pH 7 are also 'worm-like' but are coarser. Coarse fibrils are much thicker than fine fibrils, being $\approx$ 30 nm in diameter whereas fine fibrils are $\approx$ 4 nm in diameter (Takata *et al.* 2000). Coarse fibrils also tend to form tight clumps (Bromley *et al.* 2005). The size of globular microstructures has been reported by several authors as being between 100 nm and 2 μm (Resch *et al.* 2005, Krebs *et al.* 2007, Boye *et al.* 1997, Bromley *et al.* 2006). The large variation in diameters is due to different heating conditions used by each author; the heating condition employed in this study produces globules with diameters of 2 μm.

The protein microstructures in β-lg gel have a semi-rigid nature due to *(i)* covalent bonds linked by intermolecular disulphide bonds, *(ii)* intermolecular β-pleated sheets being held together by multiple hydrogen bonds, and *(iii)* hydrophobic interactions (Bryant and McClements 1998). The acidity of the solution environment during thermal gelation alters the strength of the bonds and interactions, creating the different types of microstructures mentioned above. Therefore, β-lg gels can be synthesised with desired microstructures by manipulating the acidity and temperature of the solution environment (Bromley *et al.* 2005, Lefèvre and Subirade 2000). Microstructures synthesised at pH 2 (fine fibrils), pH 4 (globules) and pH 7 (coarse fibrils) are most commonly encountered in literature; furthermore they are good reproductions of those occurring in nature, thus they are investigated in this study.

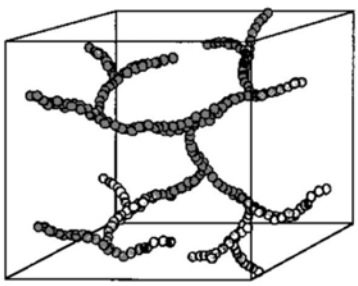

(a) Schematic representation of pH 2 gel microstructure

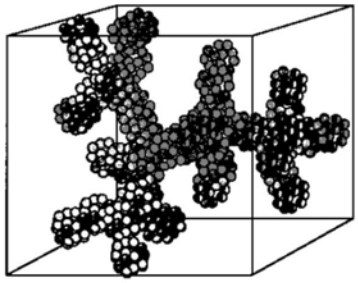

(b) Schematic representation of pH 7 gel microstructure

(c) Schematic representation of pH 4 gel microstructure

Figure 7.2: Schematic representations of microstructures in β-lg gels. (a, b) At pH 2, the β-lg monomers form chains that look 'worm-like', being typically between 100–200 nm in length and $\approx$ 4 nm in diameter. Alternatively at pH 7, the β-lg monomers tend to stick to each other, resulting in fractal aggregate formation. The fibrils also look 'worm-like' but are thicker than the ones seen at pH 2, being typically $\approx$ 30 nm in diameter. After Takata *et al.* (2000) and Gosal *et al.* (2004a). (c) This schematic of pH 4 globules is not drawn to the same scale as the figures to the left. The globules clearly resemble balls with diameter that varies with the rate of heating. Diameters reported in literature vary between 100 nm and 2 μm. After Le Bon *et al.* (1999) and Bromley *et al.* (2006).

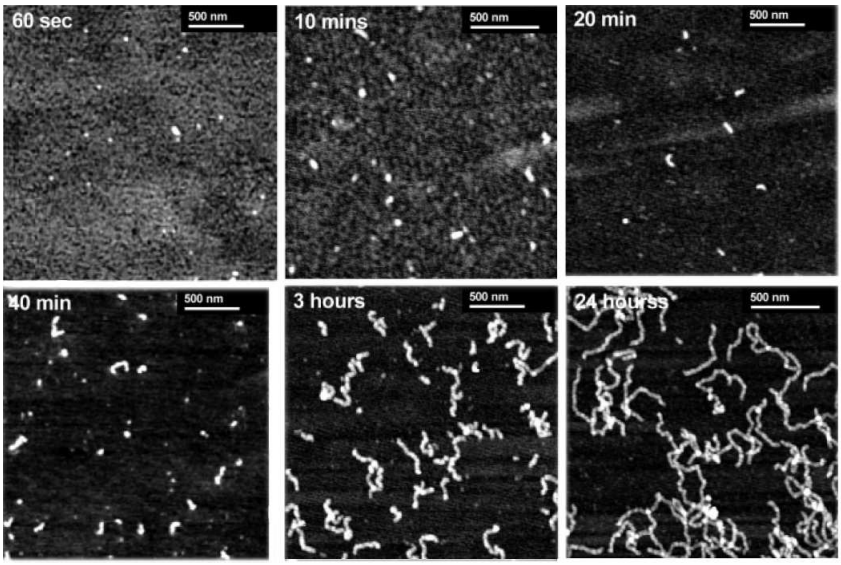

(a) Atomic force micrographs of pH 7 fibrils

Figure 7.3: Atomic force micrographs and electron micrograph of microstructures in β-lg gels. (a) Time-lapse AFM images of 4% w/w (weight/weight) β-lg gel aggregation at pH 7, incubated at 80°C from 1 minute to $>$ 24 hours. The fibrils formed after 24 hours also look 'worm-like' but are thicker than the ones seen at pH 2. In this Thesis, thick 'worm-like' fibrils are referred to as *coarse fibrils*. After Gosal *et al.* (2004a).

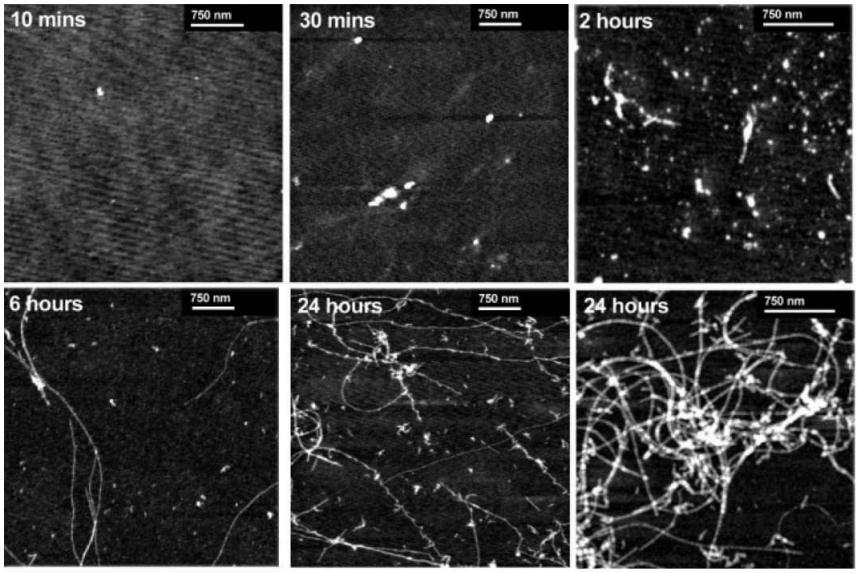

(b) Atomic force micrographs of pH 2 fibrils

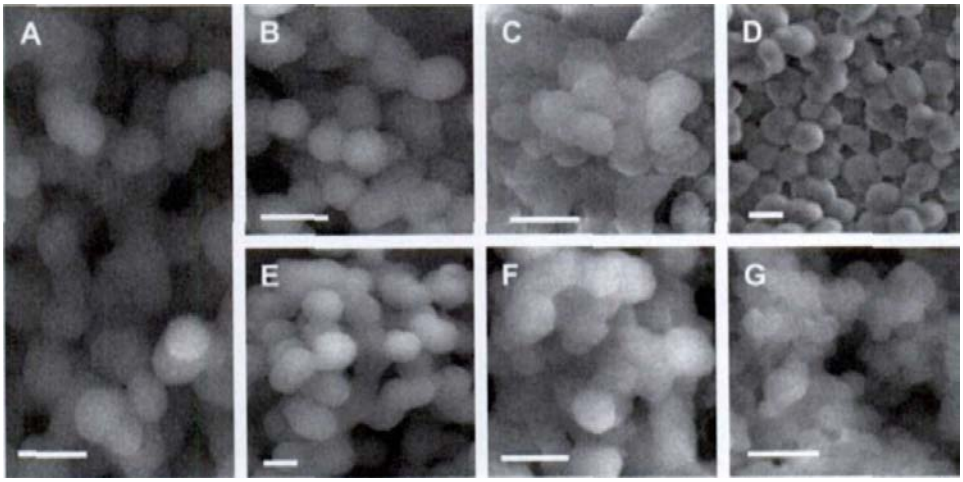

(c) Electron micrographs of pH 4 globular aggregates

Figure 7.3: Atomic force micrographs and electron micrograph of microstructures in β-lg gels (continued). (b) Time-lapse AFM images of 4% w/w β-lg gel aggregation at pH 2, incubated at 80°C from 10 minutes (top left) to $>$ 24 hours (bottom right). The fibrils formed after 24 hours look 'worm-like', being typically between 100–200 nm in length. In this Thesis, thin 'worm-like' fibrils are referred to as *fine fibrils*. After Gosal *et al.* (2004a). (c) The aggregates can be formed by thermal gelation of different types of proteins in NaCl. The white scale bar in each image represents 1 μm. The types of proteins used are: (A) bovine β-lg; (B) bovine serum albumin; (C) bovine insulin; (D) horse heart myoglobin; (E) chicken eggwhite lysozyme; (F) human transthyretin; and (G) human α-synuclein. After Krebs *et al.* (2007).

7.4 Synthesising β-Lactoglobulin Gels

The synthesis, gelation dynamics and kinetics of β-lg gels are discussed in detail in (Gosal *et al.* 2004a, Resch *et al.* 2005, Gosal *et al.* 2004b, Gosal *et al.* 2004c) and references therein. A summary of the steps taken to synthesise gels is as follows. Fifteen percent (weight/volume or w/v) of β-lg powder (Sigma-Aldrich, L0130) is dissolved in 20 mM, pH 6.865 phosphate buffer[65]. The protein mixture is then filtered with a 0.2 μm syringe filter to yield an optically clear solution. The pH is adjusted to 7.0, 4.0 and 2.0 with 1 M HCl. As highlighted in Section 7.3.2, the solution at pH 2 and 7 is clear whereas it is turbid at pH 4 (close to the pI: pH 4.8–5.1).

One millilitre of solution is dispensed into an epoxy-sealed polycarbonate petri dish, and then laid flat at 80°C for 3 hours to induce thermal gelation. The sealed dish prevents the gel from dehydrating during heating, ensuring consistent water content in all samples. As highlighted in Section 7.3.2, the size of the globules in the pH 4 gel is sensitive to the heating conditions, thus the same heater and heat settings have been used in this study to ensure consistency across samples.

After heating, the gel is allowed to cool at room temperature. The pH 2 and 7 gels appear clear, indicating uniform gel formation; the pH 4 gel appears turbid due to the globular nature of the microstructures. When cool, the gels are frozen at -20°C. Freezing is necessary because the gels hold water (Hudson *et al.* 2000). Since ice is more transparent than liquid water in the low THz (0.1–3 THz) frequency range (Ashworth *et al.* 2006), THz measurement of frozen gel (as opposed to that of non-frozen gel) will demonstrate improved dynamic range and bandwidth. All gels appear turbid when frozen as shown by the optical image of a frozen pH 2 gel in Fig. 7.4.

The temperature of the gels is further reduced to 123 K (-150°C) before measurements are made; the reason for choosing this temperature is discussed in Section 7.6.2. In order to measure the gels at this temperature, it is necessary to use a cryostat together with the THz system. The cryostat requires vacuum pumping in order to achieve low temperatures below 247 K. To prevent the gels from lyophilising (freeze-drying) in this environment, the gels are measured *in situ* in their sealed dishes.

[65] To make 1 litre of pH 6.865 phosphate buffer, 3.56 g of sodium phosphate ($Na_2 HPO_4 :2H_2 O$) powder is mixed with 1 litre of milliQ water. The buffer is adjusted to pH 7 by adding hydrochloric acid (HCl).

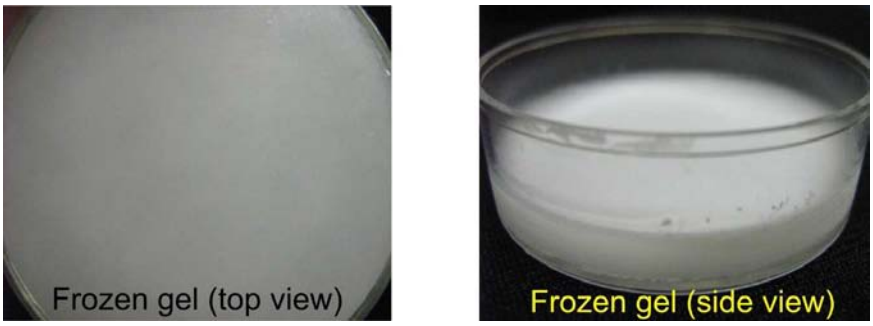

Figure 7.4: Optical image of frozen gel. Frozen pH 2 gel shown here as an example of the appearance of the gels. All the frozen gels appear turbid and opaque. For illustrative purposes, the frozen gel on the right is shown in its dish but without the sealed lid.

Since the sealed petri dishes are not resealable once opened, it is not possible to directly measure a gel's thickness without sacrificing it. Measurement of a gel's thickness cannot be made from the outside of the dish because of the meniscus effect along the wall of each petri dish. Consequently, thickness measurements are performed only after the samples have been probed with THz radiation, whereby the lids of the dishes are broken to access the gels.

Minimal handling of the frozen gels is critical to prevent thawing during thickness measurements. The use of a graduated rule allows fast and accurate measurements with minimal handling of the dishes. The rule is inserted into several positions in each dish in order to average the thickness of the sample. This process is repeated with several different batches of gels so as to obtain the overall average thickness of all frozen gels, which is 0.7 mm$\pm$0.1 mm.

7.4.1 Synthesising β-Lactoglobulin Solutions

β-Lactoglobulin solutions differ from β-lg gels in that they are not heat treated, thus thermal gelation does not occur. This means that β-lg solutions do not contain microstructures. The only two differences between the pH 2, 4 and 7 solutions are their acidity, and the turbidity of the pH 4 solution (the reason for its turbidity is explained in Section 7.3.2).

The β-lg solutions are synthesised at the same time as the gels, and frozen at -20°C. When frozen, the pH 2 and 7 solutions appear glassy, while the pH 4 solution remains

turbid. Prior to measurements, the temperature of the solutions are also further reduced to 123 K (-150°C). Like the gels, access to the solutions for the purpose of measuring their thickness is not possible due to the sealed dishes, thus thickness measurements are also only performed after the samples have been probed with THz radiation. The thickness of frozen solution is found to be 0.7 mm$\pm$0.1 mm after averaging over several different batches of solutions. This similarity in thickness to the gel is expected since the same volume of liquid is used in each dish. The presence of microstructures in the gel should not influence its thickness since the microstructures are too small to cause a difference at the sub-millimeter resolution used for measuring thickness in this study.

Results from THz measurements of both the gels and solutions at 123 K are presented in Section 7.6.

7.4.2 Verifying Microstructures in Gels used in this Study

The gels manufactured in this study are examined with an electron microscope to confirm that microstructures exist. As shown in Fig. 7.5, the gel structures observed in this study are not random accumulations of fibrils and globules but rather are well-organised, fixed 3D structures consistent with those shown in Fig. 7.3 and reported elsewhere (Gosal *et al.* 2004a, Resch *et al.* 2005, Krebs *et al.* 2007, de la Fuente *et al.* 2002, Arnaudov and de Vries 2005); the pH 2 gel has uniform fibrillar structure, the pH 7 gel has a uniform 3D matrix, and the pH 4 gel has a 3D globular matrix. Additionally, Thioflavin-T (ThT) dye tests on the gels confirm the presence of β-pleated sheets in both the fibrillar and globular gels, confirming that the gels synthesised in this study are consistent with those reported in literature. In summary, we have synthesised three gels with identical chemical composition but distinctly different microstructures.

7.5 Terahertz Spectroscopic Measurements and Results

This study utilises two different transmission-mode THz-TDS systems based on the generation of THz pulses using an ultrafast (pulsewidth = 90 fs, λ = 800 nm) near-infrared laser (Spectra-Physics Mai Tai). One system is the commercial T-ray-2000 from Picometrix as described in Section 6.4.4. The system used in this study differs from that used in Section 6.4.4 (shown in Fig. 6.12) in that the THz emitter and detector heads are mounted vertically as shown in Fig. 7.6.

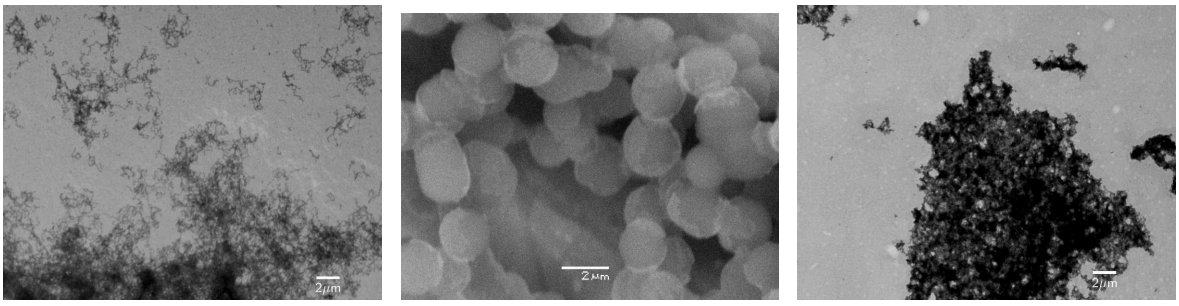

(a) pH 2 gel: fine fibrillar aggregates

(b) pH 4 gel: globular aggregates

(c) pH 7 gel: coarse fibrillar aggregates

Figure 7.5: Electron micrographs of gels synthesised in this study. The white scale bar at the bottom of each figure represents 2 μm. (a) Transmission electron micrograph (TEM) of pH 2 gel reveals fine fibrillar aggregates that are scattered loosely throughout the gel. (b) Scanning electron micrograph (SEM) of pH 4 gel reveals globular aggregates that cluster to form layers of balls. (c) TEM of pH 7 gel also reveals the presence of fibrillar aggregates but these fibrils are coarser than those at pH 2. Like the pH 4 globules, the pH 7 fibrils also cluster to form clumps.

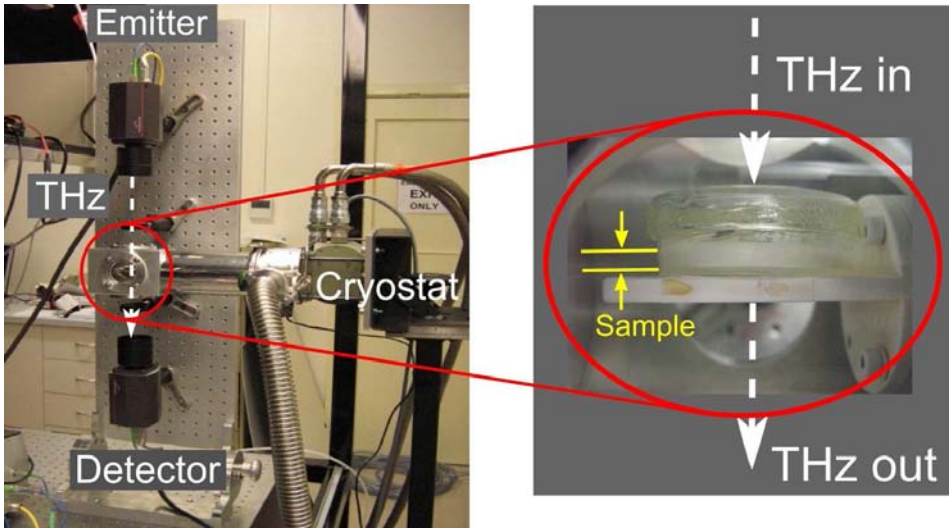

Figure 7.6: Picometrix T-ray-2000 system used in this study. Shown without the nitrogen-purged chamber. The upright arrangement of this system allows the dishes to be mounted quickly and easily on a horizontal platform without the need for clamps. A hole in the platform is wide enough to allow unobstructed THz transmission through the sample.

The other THz-TDS system—the custom photoconductive antenna (PCA) system—utilises GaAs PCAs for THz generation and coherent detection. The layout of this

system is similar to that shown schematically in Fig. 3.1(b), and an image of the system is shown in Fig. 7.7.

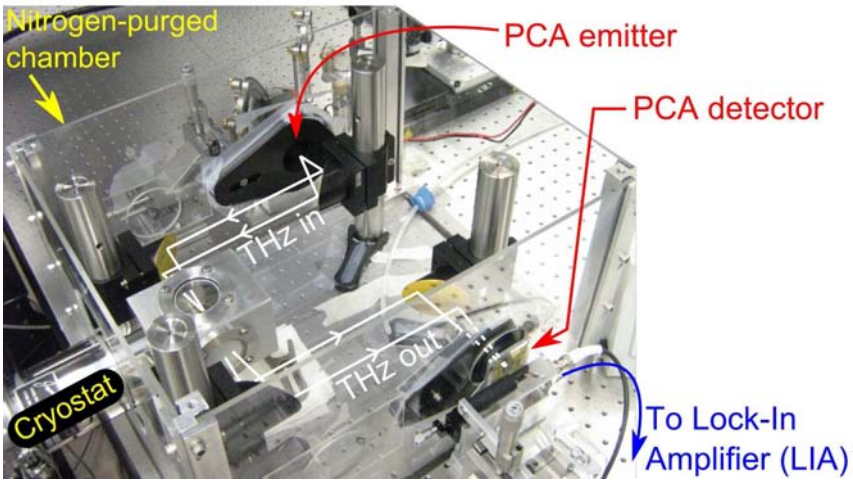

Figure 7.7: Custom PCA system used in this study. Shown with its nitrogen-purged chamber. The THz beam propagates in a path that is parallel to the optical bench, thus the samples are mounted perpendicular to the optical bench (in contrast to the Picometrix system).

A closed-cycle cryostat (Janis CCS-450) enclosed inside a nitrogen-purged chamber is used to keep the samples frozen during measurements. The samples are mounted inside the cryostat as shown in Fig. 7.6. Since the samples are sealed as described in Section 7.4, humidity and temperature are consistent across the measurements, thus reducing uncertainties caused by variations in the laboratory environment.

Since the samples are measured *in situ* in sealed dishes, the reference signal $E_{\text{ref}}(t)$ in Equation (5.1) is the transmitted THz signal through an empty sealed dish, and $E_{\text{sample+ref}}(t)$ in Equation (5.2) is the transmitted THz signal through a sample and its sealed dish. As described in Equations (5.1) and (5.2), the Fourier transforms of $E_{\text{ref}}(t)$ and $E_{\text{sample+ref}}(t)$ give $E_{\text{ref}}(\omega)$ and $E_{\text{sample+ref}}(\omega)$ respectively, with magnitude and phase components as denoted in Section 5.2.3. The sample's frequency response, $E_{\text{sample}}(\omega)$, is as described in Equation (5.3).

The presence of the dish in each THz measurement alters the calculation of the Fresnel coefficient $T(\omega)$ defined previously in Equation (5.10). In this study, the calculation of $T(\omega)$ needs to account for reflections in the base and lid of a dish, hence $T(\omega)$ is defined in this Chapter as:

$$T_{\text{dish}}(\omega) = \frac{2n_{\text{sample}}(\omega)[1+n_{\text{dish}}(\omega)]}{[1+n_{\text{sample}}(\omega)][n_{\text{dish}}(\omega)+n_{\text{sample}}(\omega)]}, \tag{7.1}$$

where $n_{\text{sample}}(\omega)$ is the refractive index of the β-lg gel or solution under investigation; $n_{\text{dish}}(\omega)$ is the refractive index of the polycarbonate petri dish.

Referring to Equation (5.21), the sample's absorption coefficient $\alpha_{\text{sample}}(\omega)$ is therefore defined in this Chapter as:

$$\begin{aligned} |E_{\text{sample+ref}}(\omega)| &= T_{\text{dish}}(\omega)\ |E_{\text{ref}}(\omega)|\, e^{-\alpha(\omega)d/2} \\ |E_{\text{sample}}(\omega)| &= \frac{|E_{\text{sample+ref}}(\omega)|}{|E_{\text{ref}}(\omega)|} = T_{\text{dish}}(\omega)\, e^{-\alpha(\omega)d/2} \\ \alpha_{\text{sample}}(\omega) &= -\frac{2}{d}\ln\left(\frac{|E_{\text{sample}}(\omega)|\,[1+n_{\text{sample}}(\omega)][n_{\text{dish}}(\omega)+n_{\text{sample}}(\omega)]}{2n_{\text{sample}}(\omega)[1+n_{\text{dish}}(\omega)]}\right), \end{aligned} \quad (7.2)$$

where d is the thickness of the β-lg gel or solution. The term *absorption coefficient* is replaced henceforth with the term *extinction coefficient* because it will be shown in Section 7.5.1 that both absorption and scattering are observed, hence *extinction coefficient* more accurately describes the observed physical phenomenon.

The sample's refractive index is as defined in Equation (5.22). Analysis of a sample's refractive index is necessary to ascertain if dispersion occurs inside the sample. If the profile of the refractive index is relatively flat over the frequencies of interest, then there is negligible dispersion in the material. The extinction coefficient provides a gauge of the strength of the detected THz signal. If extinction is high, then the test material strongly absorbs and/or scatters the incident THz signal, resulting in a weaker detected signal. Resonant frequencies of biomolecules manifest as peaks in the extinction coefficient plot, thus the extinction coefficient also helps in the identification of biomolecules. The slope of an extinction coefficient plot is another technique for differentiating between more complex biological systems such as gels and biotissue (Fitzgerald *et al.* 2003, Png *et al.* 2008a).

7.5.1 Rayleigh Scattering

In this study, Equation (7.2) is referred to as *extinction* instead of *absorption* because scattering is taken into account as being one of the contributors towards an increase or decrease in the measured THz signal strength. Extinction is therefore the sum of absorption in the material, and scattering from the material (Bohren and Huffman 1983).

Scattering is presented and discussed in detail in Chapter 8, therefore only a brief overview of scattering with sufficient depth for this Chapter is given below.

Given the small dimensions of the fibrils and globules in the gels compared to the THz wavelengths of interest in this study (wavelength λ = 750 μm–192 μm), Rayleigh scattering would be the dominant scattering encountered in experiments from this study. Rayleigh scattering is a special case of Mie scattering for small particles with size $\ll \lambda$. It is conventionally reported in terms of the scattering cross section (analogous to radar cross section or echo area) which is a measure of power scattered in a given direction when incident radiation illuminates a target object (van de Hulst 1957, Bohren and Huffman 1983, Knott *et al.* 2004). When the scattering cross section C_{sca} is normalised by the geometric cross section, the result is the scattering efficiency Q_{sca}. As given in (Bohren and Huffman 1983), the equations describing the Rayleigh scattering efficiencies for L spheres (representing globules), each with radius r, are:

$$Q_{sca}(\omega) = \frac{8\,L\,x^4}{3}\left|\frac{m^2-1}{m^2+2}\right|^2 \tag{7.3}$$

$$\text{where } m(\omega) = \frac{\hat{n}_{mst}(\omega)}{\hat{n}_{sm}(\omega)} \tag{7.4}$$

$$x(\omega) = \frac{2\pi\hat{n}_{mst}(\omega)\,r}{\lambda} \tag{7.5}$$

$$\begin{aligned}\hat{n}_{mst}(\omega) &= n_{mst}(\omega) + i\,\kappa_{mst}(\omega)\\ &= n_{mst}(\omega) + i\,\frac{\alpha_{mst}(\omega)\,c}{2\omega},\end{aligned} \tag{7.6}$$

where 'mst' denotes 'microstructure' and 'sm' denotes 'surrounding medium'; $n_{mst}(\omega)$ and $\alpha_{mst}(\omega)$ are averages of the experimental values $n_{sample}(\omega)$ and $\alpha_{sample}(\omega)$ respectively. In these models, we assume that the protein microstructure are suspended in air, hence $\hat{n}_{sm}(\omega) = \hat{n}_{air}(\omega) = 1.0003 \approx 1$. Since the models described above treat the gels as homogeneous media suspended in air, they are only approximations of the actual samples which contain more complex protein microstructures suspended in frozen solution.

If the incident THz radiation field is parallel to the long axis of an infinitely long cylinder, then the equations in (Bohren and Huffman 1983) that describe Rayleigh scattering efficiencies for P infinite cylinders (representing fibrils), each with radius r are:

$$Q_{sca}(\omega) = \frac{2P}{x}\left[\,|b_0(\omega)|^2 + 2\,|b_1(\omega)|^2\,\right] \tag{7.7}$$

$$\text{where } b_0(\omega) \approx \frac{-i\pi x^2(m^2-1)}{4} \tag{7.8}$$

$$b_1(\omega) \approx \frac{-i\pi x^4(m^2-1)}{32}. \tag{7.9}$$

Note that Equations (7.3) and (7.7) assume that scattering from multiple particles is a cumulative effect of scattering from individual particles, and that there is no coupling or multipath scattering between particles.

7.6 Results

The results in this study are presented as plots of the samples' THz extinction $\alpha(\omega)$ and refractive indices $n(\omega)$ over the usable frequency bandwidth of the systems, which spans from 0.4 to 1.56 THz. As defined in Equations (5.22) and (7.2), each $n(\omega)$ or $\alpha(\omega)$ plot presented is derived from $E_{\text{sample+ref}}(t)$ and $E_{\text{ref}}(t)$, averaged over 25 measurements. Measurements are made only after the desired temperature in the cryostat has stabilised for 15 minutes. Similar results are observed in both the Picometrix and custom PCA systems, hence only the Picometrix results are presented here.

7.6.1 Differentiation of Structures

The THz extinction coefficients $\alpha(\omega)$ of the pH 2, 4 and 7 gels at 123 K (-150°C) are presented in Fig. 7.8(a); $\alpha(\omega)$ of the pH 2, 4 and 7 solutions at the same temperature are shown in Fig. 7.8(b).

As seen in Fig. 7.8(a), the gradients of all three gel plots are similar in the lower THz range, but a distinct linear rise from the baseline occurs for the pH 4 gel from ≈ 0.8 THz onwards. Figure 7.8(b) shows that all three solutions have similar $\alpha(\omega)$ profiles which do not deviate significantly from the baseline. The linear rise in the $\alpha(\omega)$ profile of pH 4 gel is therefore distinct from the profiles of all solutions and the pH 2 and 7 gels. Similar results are observed in both the Picometrix and custom PCA systems.

The refractive indices of the gels and solutions are presented in Figs. 7.9(a) and 7.9(b) respectively. As shown in these Figures, the refractive index profiles of both the gels and solutions are relatively flat over the system bandwidth, indicating that there is no dispersion of the THz signal inside the samples. This means that the steep rise in THz extinction characteristic observed in the pH 4 gel is not an artifact caused by dispersion.

The error distribution of the solutions' refractive indices is large when compared to those of the gels', making refractive index an unreliable parameter for distinguishing between gels and solutions. However among the gels, the refractive index of the pH 4 gel is clearly higher than those of the pH 2 and 7 gels, but this difference is not as significant as that seen in the extinction coefficient $\alpha(\omega)$.

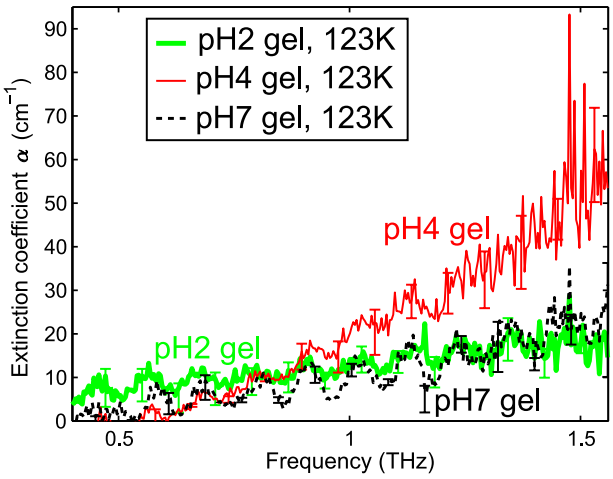

(a) THz extinction coefficients of gels at pH 2, 4 and 7

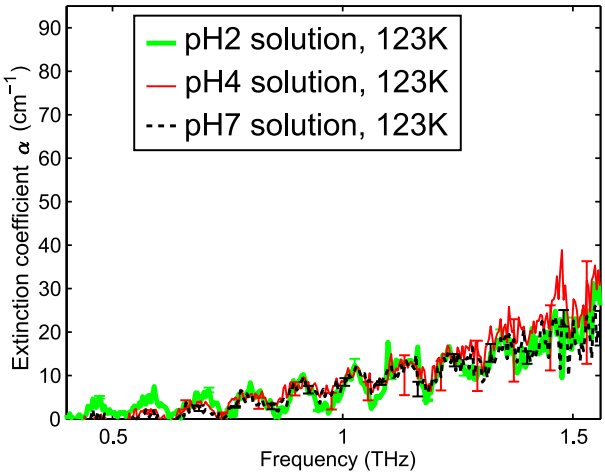

(b) THz extinction coefficients of solutions at pH 2, 4 and 7

Figure 7.8: Extinction coefficients of β-lg gels and solutions. The distinct rise in the THz extinction coefficient of pH 4 gel is likely due to the globular microstructure in the gel. The two different fibrillar structures in the pH 2 and 7 gels are indistinguishable from each other. Furthermore, the fibrils have the same THz response as the solutions, which lack any microstructures.

The steep rise in the extinction coefficient of the pH 4 gel could be explained through analysis of Rayleigh scattering from spherical and cylindrical scatterers that model the globular and fibrillar microstructures respectively. As discussed in Section 7.3.1, the ball-like structures are much larger than the fibrils in the pH 2 and 7 gels, hence they appear as spherical scatterers to the incident THz radiation.

Figure 7.10(a) presents a comparison of the Rayleigh scattering efficiencies $Q_{\text{sca}}(\omega)$ against the extinction coefficients $\alpha(\omega)$ of pH 4 and 7 gels. Equations (7.3) and (7.7) are

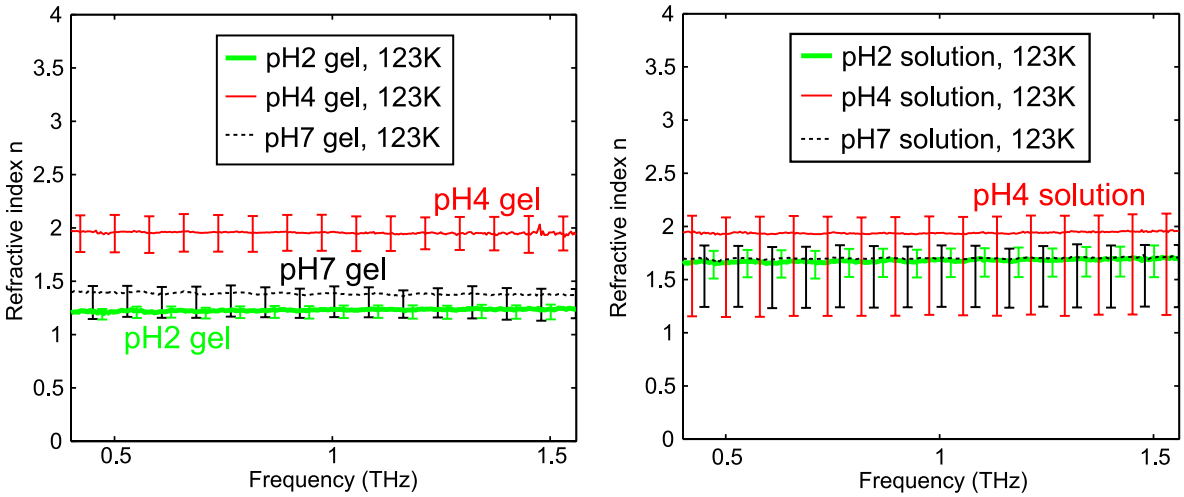

(a) Refractive indices of gels at pH 2, 4 and 7

(b) Refractive indices of solutions at pH 2, 4 and 7

Figure 7.9: Refractive indices of β-lg gels and solutions. The refractive indices $n(\omega)$ of both the gels and solutions do not vary much with frequency since their profiles are relatively flat over the system bandwidth. This means that there is no evidence of dispersion of the THz signal inside the samples. The error bars are generated based on $\pm$ 0.1 mm uncertainty in the measurement of sample thickness.

used to generate the $Q_{sca}(\omega)$ plots based on the following parameters: radius = 1 μm for a sphere (to model a pH 4 globule); radius = 15 nm and length = 2 μm for a wide cylinder (to model a pH 7 coarse fibril). Approximately $P = 2963$ cylinders will fit into $L = 1$ sphere, where L and P are as defined in Equations (7.3) and (7.7) respectively. The parameter P is necessary because scattering from one cylinder with the given dimensions is several orders smaller than that from one sphere, making it difficult to compare the extent of scattering on the same scale.

Although these Rayleigh scattering models for pH 4 and 7 gels are only approximations to the more elaborate microstructures in the gels, there is good agreement between the models and the experimental results. This therefore suggests that THz scattering is a possible mechanism for the observed differences in the extinction coefficients of the globular and fibrillar gels. However, when Fig. 7.8(a) is compared with Fig. 7.8(b), it might be argued that the profile of the pH 7 gel is not due to scattering by the fibrils but could be due to absorption of the solution, or scattering by ice. Therefore this preliminary result motivates future experiments to further explore the effect of scattering.

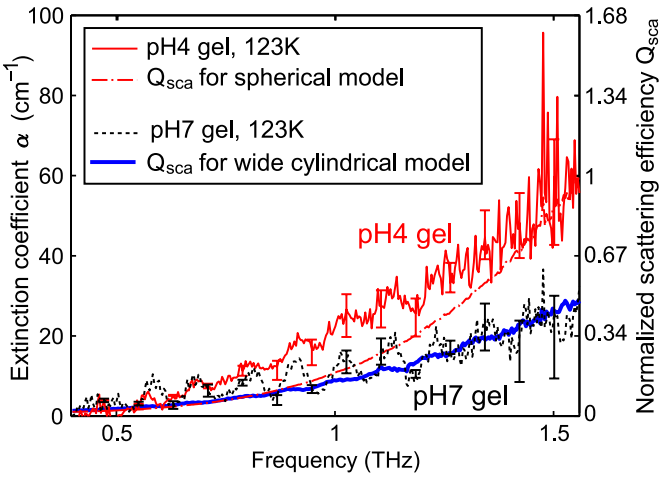

(a) Comparison of pH 4 and 7 gels' extinction coefficients with normalised Rayleigh scattering efficiencies $Q_{sca}(\omega)$

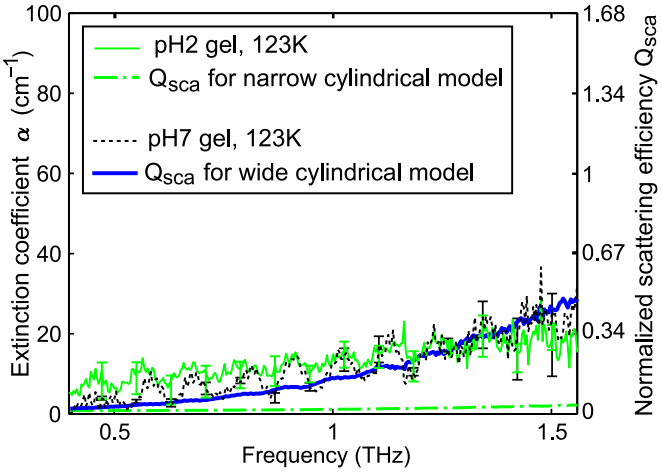

(b) Comparison of pH 2 and 7 gels' extinction coefficients with normalised Rayleigh scattering efficiencies $Q_{sca}(\omega)$

Figure 7.10: Normalised Rayleigh scattering efficiencies $Q_{sca}(\omega)$ versus extinction coefficients $\alpha(\omega)$ of fibrils and globules. Rayleigh scattering is a special case of Mie scattering, and is applicable in this study due to the small dimensions of the microstructures. (a) The plot of $Q_{sca}(\omega)$ for a single sphere model of a pH 4 globule, and the plot of $Q_{sca}(\omega)$ for clusters of wide cylinders modelling the pH 7 coarse fibrils reveal that the steep rise in the extinction coefficient of the pH 4 gel could be due to scattering. (b) There is good agreement between $Q_{sca}(\omega)$ for clusters of wide cylinders and the extinction coefficient of the coarse fibrils at pH 7, but no agreement between $Q_{sca}(\omega)$ for clusters of narrow cylinders and the extinction coefficient of fine fibrils at pH 2. This indicates that the existing spatial resolution of the THz-TDS systems used in this study is insufficient for differentiating between the fine and coarse fibrils.

For the pH 2 gel, parameters used in Equation (7.7) are: radius = 2 nm, length = 2 μm for a narrow cylinder (to model a pH 2 fine fibril). Approximately $P = 166700$ narrow cylinders will fit into $L = 1$ sphere, where L and P are as defined in Equations (7.3) and (7.7) respectively. The extinction coefficients of the pH 2 and 7 gels and solutions appear very similar over the system bandwidth, however as shown in Fig. 7.10(b) plots of $Q_{sca}(\omega)$ reveal that the scattering efficiencies are dissimilar. It can therefore be concluded that the fine and coarse fibrillar structures in pH 2 and 7 gels respectively are too small to be differentiated given the existing resolution of a THz-TDS system.

In summary, the distinct change in the extinction coefficient of the globular aggregate as compared to the negligible change for the fibrillar aggregates strongly indicates that THz-TDS can be employed as an effective non-destructive inspection tool for differentiating between globular and fibrillar microstructures in gels, but is ineffective at differentiating between coarse and fine fibrillar microstructures. In the context of this Thesis, this finding is encouraging as it is the first step in using THz spectroscopy to study fibrillar structures. With refinement of future THz spectroscopic techniques (e.g. THz microscopy), differentiating between the coarse and fine fibrillar microstructures may become a reality, paving the way for establishing specificity tests for detecting different types of fibrillar amyloid-β proteins in biotissue and/or biological fluid.

7.6.2 Influence of Sample Preparation and Measurement Conditions

To ensure results in this study are not biased by experimental conditions, this Subsection explores the effects of preparation techniques, measurement temperature, and type of test media on this study's findings.

Influence of Freezing Rate

The first issue addressed is the influence of freezing rate. Although ice is more transparent than liquid water in the THz frequency range, large ice crystals may still scatter THz radiation and cause a decrease in the measured THz signal. Furthermore, large ice crystals may destroy the 3D microstructure in protein gels. The size of ice crystals is related to the rate of cooling (Meryman 1956). As highlighted in Section 5.5.1, the freezing process in a laboratory freezer, such as the one used in this study, is considered *slow*, implying that large ice crystals are grown. Smaller ice crystals are grown through *snap-freezing* in cryogens, such as liquid nitrogen, propane and isobutane.

A separate batch of pH 4 gels and solutions is synthesised according to the steps detailed in Section 7.4 but is snap-frozen instead of slow frozen. The snap-frozen gels and solutions are then measured with THz in the same manner as the slow frozen samples (i.e. *in situ* in petri dishes).

Results of the extinction coefficients $\alpha(\omega)$ of slow and snap-frozen samples are presented in Fig. 7.11. It is noted that the spectrum of the snap-frozen pH 4 gel in Fig. 7.11(b) is noisier than the other three spectra in Fig. 7.11. A possible source of the noise is hairline cracks in the snap-frozen pH 4 gel. Regardless of snap-frozen pH 4 gel's noisy spectrum, a comparison of the gradients of all four plots reveals that the extinction coefficients $\alpha(\omega)$ of slow and snap-frozen samples are similar, indicating that freezing rate has no observable effect on the differing extinction coefficients seen in Section 7.6.1 for the pH 4 gels and the other samples.

Influence of Sample Holder

The next issue addressed is the influence of the sample holder. Since the gels and solutions are measured *in situ* in petri dishes, etalon reflections in the dishes are evident as oscillatory artifacts in the plots shown in Fig. 7.8. To eliminate the influence of the dishes and any other possible interference that may arise from the synthesis (e.g. air gaps between sample and dish, cracks, random ice crystals in the path of the THz beam), the pH 4 gels and solutions are lyophilised (freeze-dried) for 24 hours. Lyophilisation reduces water from the sample, leaving only a small amount of bound water. The lyophilised samples therefore have a powdered texture and can be pressed into pellets for measurement with THz. In this study, the lyophilised samples are mixed with polyethylene powder to create sufficient bulk for making pellets. The thickness of the pellets is 0.62 mm $\pm$ 0.03 mm, and measurements are made at 120 K.

Results of the extinction coefficients $\alpha(\omega)$ of pH 4 pellets are presented in Fig. 7.12. These results reveal that pH 4 gel experiences stronger THz extinction than pH 4 solution, however this difference is not as pronounced as that seen in Section 7.6.1 for the frozen gels and solutions that are measured *in situ* in dishes.

Influence of Temperature

The final issue addressed is the influence of measurement temperature. As shown in Fig. 7.13, a reduction in temperature results in the reduction of the extinction coefficient $\alpha(\omega)$ of pH 4 gel. The extent of reduction in $\alpha(\omega)$ is initially large at higher

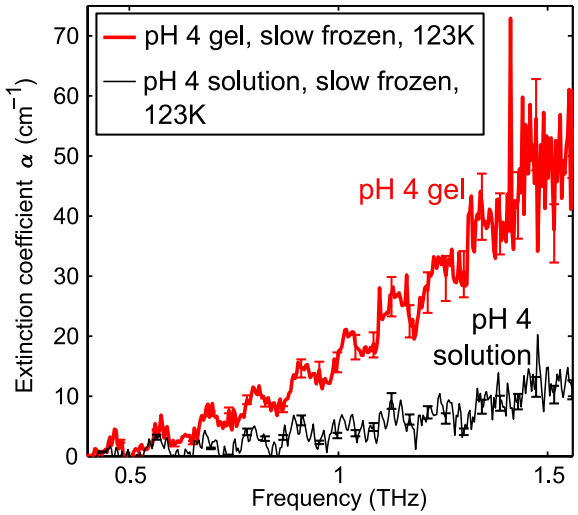

(a) Slow frozen pH 4 gel and solution

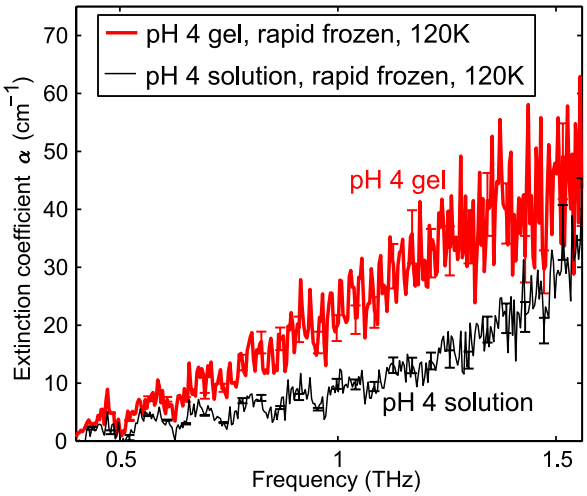

(b) Snap-frozen pH 4 gel and solution

Figure 7.11: Comparison of slow and snap-frozen pH 4 gels. The slopes of both the slow and snap-frozen pH 4 gels are similar despite scattering from hairline cracks in the snap-frozen pH 4 gel sample which manifest as jagged artefacts.

temperatures (e.g. from 250 K to 220 K), but stabilises at low temperatures. This phenomenon can be explained by the reduction in the extinction coefficient of ice at low temperatures (Ashworth *et al.* 2006); water activity at higher temperatures results in stronger attenuation of the incident THz signal. It is therefore important to identify a temperature at which measurements are stable.

The cryostat used in this study can be cooled down to 4 K (-269°C) but the cooling time required to attain this extremely low temperature results in extended experimental time. As evident from the 120 K and 20 K plots in Fig. 7.13, the bandwidth and

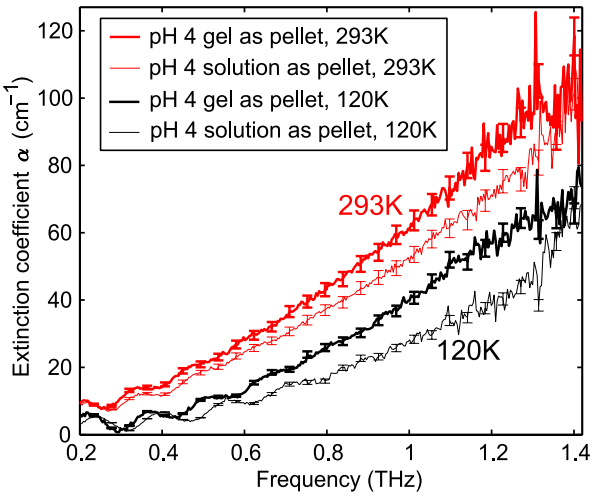

Figure 7.12: Effect of lyophilisation on extinction coefficient. The pH 4 gel and solution are lyophilised, mixed with polyethylene powder and pressed into pellets. At room temperature (293 K), the difference between pH 4 gel and solution is apparent but is more significant at 120 K.

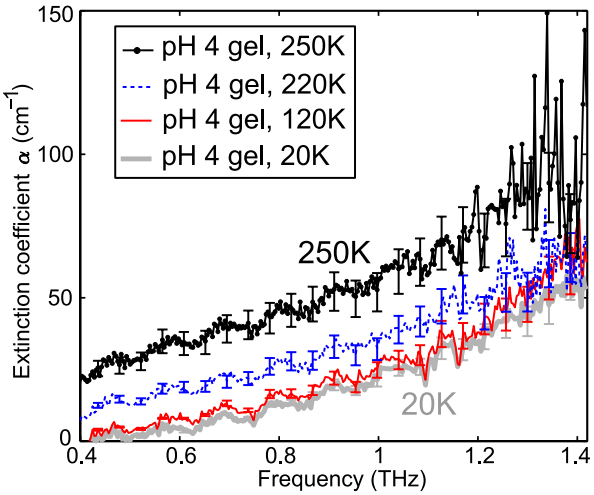

Figure 7.13: Influence of measurement temperature on extinction coefficients. The frequency bandwidth and dynamic range of the pH 4 gel measurements improve with decreasing temperatures, but begin to convergence at 180 K. There is no significant difference between the measurements made at 120 K and 20 K.

dynamic range of the measurements are similar at these two temperatures, hence measurements at extremely low temperatures, such as 20 K, are superfluous. Measurements in this study are conducted at 123 K (-150°C), thus the observation for pH 4 gel seen in Section 7.6.1 is not due to water/ice activity or temperature fluctuations, but is more likely due to scattering.

7.7 Conclusion

This study has demonstrated that THz-TDS can be used at low temperatures as a non-destructive differentiation tool for microstructures in gels derived from whey protein. Three dimensional globular (pH 4.0) and fibrillar (pH 2.0 and 7.0) microstructures have been synthesised via thermal gelation of β-lg solution at different pH values. When examined between 0.8 and 1.5 THz, the globular β-lg structures with diameters of 2 μm have a decline in transmission (rise in extinction coefficient) when compared to fibrillar structures with similar lengths but with diameters less than 0.03 μm. The decline in transmission for the globular β-lg structures is attributed to Rayleigh scattering. Globular and fibrillar microstructures are shown to have distinct extinction coefficient gradients; the relative difference provides a good means of differentiating between the two microstructures. The best results are obtained for frozen protein gels, with lyophilised pH 4 gels showing a less pronounced change. This change in extinction coefficient for globular microstructures compared to fibrillar microstructures is shown to be independent of temperature, freezing rate and type of sample holder.

7.7.1 Future Work

One potential application of this work is the morphological study of highly cytotoxic granular protein aggregates with THz-TDS. Such granular protein aggregates can form fibrillar aggregates that are classified as amyloid fibrils, which are associated with Alzheimer's disease (Bucciantini *et al.* 2002). Future work will explore this avenue in addition to improving sample preparation and spectroscopic techniques with the aim of differentiating between fibrillar structures with different diameters.

7.8 Chapter Summary

This study has shown that THz-TDS can be used to differentiate between the fibrillar and globular microstructures in protein gels; this result is encouraging because both fibrillar gels have β-pleated sheets resembling those in amyloid-β fibrils. This means that it is possible to use THz spectroscopy to identify amyloid-β fibrils in brain tissue if the tissue is devoid of blood vessels and other granular matter. This ideal tissue environment is realistically not possible unless the tissue is homogenised as described in Section 6.6.1 to isolate the fibrillar amyloid-β proteins. Homogenisation of brain

tissue may indeed be a feasible option given that the outcome from this study has shown it is possible to probe isolated fibrillar structures with THz radiation.

Before embarking on homogenising more donor tissue, it is useful to first gain an understanding of how THz radiation interacts with fibrillar structures. Amyloid-β fibrils have been reported to be birefringent to optical light (Sipe and Cohen 2000); green birefringence is exhibited when the fibrils are stained with Congo red dye (Rosenblum 2002). Characterising the scattering and transmission profiles from fibrillar structures is the impetus for the work to be presented in the next Chapter.

Chapter 8

Scattering from Subwavelength Fibrils in the Terahertz Regime

FIBRILLAR structures are common in both natural and artificial forms. Strands of hair and natural fabric are fibrillar, and fibrillar microstructures with β-pleated sheets are believed to be responsible for amyloidosis diseases in humans. Glass fibres of various dimensions are manufactured for a wide range of industrial, medical and domestic applications. There is a need to better understand how THz radiation interacts with these structures, specifically the extent of scattering. Understanding scattering is crucial in many potential THz applications, which rely on the detection of reflected/scattered THz signals, such as *in vivo* skin cancer detection, quality control, and security.

As described in the previous Chapter, small fibrillar microstructures in synthesised gels require observation with microscopic aids such as a scanning electron microscope (SEM), hence the alignment of the microstructures is not easily determined. In this Chapter, larger fibrillar structures, which can be manually aligned, are used. Knowledge of the fibrils' alignment allows experimental THz measurements to be compared with numerical and analytical models that simulate the experimental conditions, allowing for the characterisation of a generic fibrillar structure in the THz frequency range.

8.1 Introduction

In Chapter 3, two THz spectroscopic configurations were introduced: transmission and reflection. For the reflection configuration, scattering from a sample is the basis for which the THz signal is detected, hence scattering is an obvious concern. For the transmission configuration, there is a less obvious but equally important need to understand how scattering from a sample alters the transmitted THz signal.

Terahertz research into scattering from samples measured in transmission mode has mainly focused on powders (Zurk *et al.* 2007, Bandyopadhyay *et al.* 2007, Shen *et al.* 2008, Franz *et al.* 2008), and fibres from clothing (Bjarnason *et al.* 2004, Kaliteevski *et al.* 2006, Fletcher *et al.* 2007). The reason for this focus may be due to the large body of studies involving protein-polyethylene powder mixtures pressed into pellets, as well as THz security applications (e.g. drug or weapon detection through clothing or baggage).

Other materials used in THz scattering studies include cork enclosures (Hor *et al.* 2008), pork-fat and onion cells (Han *et al.* 2000), wood and paper (Reid and Fedosejevs 2006), polymers (Beckmann *et al.* 2006), fibreglass cloth (Naito *et al.* 2009a, Naito *et al.* 2009b), and hollow fibre with a film of absorptive dielectric inner-coating (Tang *et al.* 2009). In the study on wood, THz birefringence in wood was discovered as a result from scattering studies.

Surface roughness studies have also emerged from reflection mode THz scattering studies for communication purposes (Dikmelik *et al.* 2006, Kleine-Ostmann *et al.* 2007, Piesiewicz *et al.* 2007). Statistical studies of THz scattering in random media (Pearce *et al.* 2003, Pearce and Mittleman 2003, Jian *et al.* 2003), and computer models for THz scattering (Fletcher *et al.* 2007, Zhong *et al.* 2007) are also areas of research. Terahertz ranging akin to that used in radar ranging is another topic of interest (Cheville *et al.* 2003).

8.1.1 Motivation

Within the overall body of literature pertaining to cylindrical scatterers, few theoretical models have been presented to explain the fibrillar scattering phenomena observed. One notable exception is in Fletcher *et al.* (2007), where a phase distribution function is used to model the random structure of various fabrics. Although more literature exists

for theoretical modelling of spherical scatters, the overall landscape of THz scattering studies, regardless of the samples' shapes, is sparse. This gap in knowledge is the first of two motivations for the study to be presented in this Chapter.

The second motivation for this study stems from Chapters 5 and 7 of this Thesis. The influence of hair and hair follicles was highlighted in Section 5.3.1. In Section 7.6.1, the different extent of scattering from fibrillar microstructures as opposed to that from globular microstructures facilitated their differentiation. Experimental results could be explained to some extent using exact theory, i.e. Rayleigh scattering. Although there was good agreement between experimental results and theory, questions still exist with regards to whether scattering is solely due to the microstructures. It is therefore important to now focus on scattering from fibrillar structures in the THz frequency range. The study presented in this Chapter will therefore answer as well as complement the work reported in Chapters 5 and 7.

8.1.2 Objective Summary

In order to focus on scattering from fibrillar microstructures, it is useful to implement a test environment that is not only easy to fabricate, but can also be verified using mathematical theory. One such environment contains fibrillar structures that have a known orientation, such as all fibrils being aligned parallel to the polarisation of the incoming THz beam. Terahertz measurements from this contrived environment can then be compared with exact theory as well as solutions from simulations using full-vectorial solvers (e.g. High Frequency Structure Simulator or HFSS from Ansoft).

This Chapter presents a novel study involving THz experiments, analytical solutions, and numerical solutions using HFSS to analyse scattering from fibrillar structures. This study shows that analytical solutions do not satisfactorily verify measurements because they ignore the contributions of mutual coupling between structures. Conversely, results from HFSS not only elucidate the measurements, they provide an important insight into how the scattering behaviour of cylindrical scatterers is influenced by test conditions.

A large extent of the analytical solutions presented in this Chapter are based on scattering models developed for other frequency ranges, hence a quick review of literature is provided in the next Section. The mathematics of scattering salient to this Thesis is

presented in Section 8.3. Results from this study are presented from Section 8.4 onwards.

8.1.3 Location of Experimental Work

The THz experiments described in this Chapter were performed at the University of Leeds in the UK, and at the University of Adelaide. The MATLAB and HFSS computer simulations were performed at the University of Adelaide.

8.2 Brief Review of Scattering-Related Literature

As highlighted in Section 8.1, THz scattering studies have mainly involved powders and cloth; the majority of studies has relied upon Mie scattering to explain the observed scattering phenomena.

The amount of scattering-related THz studies is small when compared to studies involving scattering at frequencies outside the THz range. Meteorology and astronomy are areas where scattering from rain, snow, interstellar dust clouds, *etc.* are of major interest (van de Hulst 1980a, van de Hulst 1980b, Huang *et al.* 2005). Another active area of research is scattering of light at various frequencies for medical diagnostic purposes, such as MRI, CT, near-IR tomography, and optical coherence tomography or OCT (Bickel *et al.* 1976, van Staveren *et al.* 1991, Tuchin 2000, Wang *et al.* 2005, Wang *et al.* 2006).

While there is a scarcity of THz literature on scattering from fibrillar (cylindrical) scatterers, this is not so for frequencies outside the THz frequency range; over the past 5 decades, both spherical and cylindrical scatterers have been thoroughly investigated. Although these studies are not specifically for the THz frequency range, the mathematical concepts introduced in many of these studies are, in theory, scalable to the THz range. A summary of studies are presented as follows:

Spheres

- ground glass (Bennett 1963);
- spheroidal particle (Asano and Yamamoto 1975, Asano and Sato 1980);
- cells (Drezek *et al.* 1999);
- turbid medium with large particles (Gorodnichev *et al.* 2006);

Cylinders

- wires (Richmond 1965c, Richmond 1965b, Richmond 1966a, Richmond 1966b);
- fibres (Bickel *et al.* 1980);
- single fibre (Bell and Bickel 1981);
- fibrils (Freund *et al.* 1986);
- stratified cylinders (Barabás 1987);
- dielectric cylinders (Ruppin 1990);
- inhomogeneous cylindrical layers (Swathi *et al.* 1991);
- coated cylindrical fibres (Cunnington Jr. *et al.* 1992);
- wire grids (Wait 1955);
- tenuous cylindrical membranes (Zhou and Knighton 1995);
- cylinders close to planes (Videen and Ngo 1997);
- parallel cylindrical arrays (Zhou and Knighton 1997);
- embedded cylindrical targets (Belkebir *et al.* 1997); and
- Mie scattering at near-infrared frequencies (Wang *et al.* 2005, Wang *et al.* 2006).

Mathematical models have been developed to describe the effect of scattering in the optical frequency range (Chandrasekhar 1960, Richmond 1965a, Budko and van der Berg 1999). One particular area of research that has produced a host of mathematical models for optical light scattering is computer graphics. Shading of objects in a virtual world is an important consideration for realistic rendering of computer graphics. Examples of well-known shading models for uneven surfaces are Beckmann (1963), Torrance and Sparrow (1967), Gouraud (1971), and Phong (1975). In Appendix F, an example of the use of the Beckmann model to study the impact of skin surface roughness in the THz regime is presented.

The next Section presents an overview of mathematics relevant to exact Mie theory, of which Rayleigh theory is a special case. A summary of the equations used in Mie theory was presented in Section 7.5.1 to explain the observed results in that Section—those equations will be revisited in Section 8.3.2 for completeness.

8.3 Overview: Mie Scattering

This Section presents an overview of the mathematical theory of Mie[66] (and Rayleigh) scattering. The equations presented below are from texts dealing with general scattering theory, namely van de Hulst (1957) and Bohren and Huffman (1983). Derivations of these scattering-related equations are included in Appendix F together with mathematics pertaining to spherical scatterers, Rayleigh-Gans scattering, geometrical optics, and the Beckmann model.

8.3.1 Definition: An Infinitely Long Right Circular Cylinder

In Bohren and Huffman (1983), an *infinitely long right circular cylinder* is defined as a circular cylinder which has length $l \gg$ diameter $2r$, and is orientated orthogonal to the direction of propagation of an incident electromagnetic beam as shown in Fig. 8.1(a).

Many naturally occurring organisms and minerals, such as some viruses and asbestos, can be modelled accurately by infinitely long circular cylinders. Equally common in everyday life are synthetic objects that can be represented as infinitely long cylinders, such as fabric fibres or hairline scratches on hard surfaces. Arrays of infinitely long cylindrical objects can display distinct scattering and transmission characteristics, such as birefringence or dichroism, which allow for their detection and identification (e.g. birefringent proteins are luminous when dyed appropriately). The prevalence of infinitely long circular cylinders make them interesting and useful objects to study.

If the infinitely long right circular cylinder is orientated as shown in Fig. 8.1(a) such that the cylinder is parallel with respect to the vertically polarised THz beam, then this orientation is termed *parallel* in this Thesis, and is denoted by the symbol $\parallel$. This orientation is known as transverse magnetic[67] or TM. If the cylinder is orientated perpendicular to the vertically polarised THz beam as shown in Fig. 8.1(b), then this orientation is termed *perpendicular* in this Thesis, and is denoted by the symbol $\perp$. This orientation is known as transverse electric[68] or TE. The parallel and perpendicular terminologies are used throughout this Chapter.

[66] Named after Gustav Mie.

[67] TM^z is used in some literature, where the z superscript indicates the axis of reference.

[68] TE^z is used in some literature, where the z superscript indicates the axis of reference.

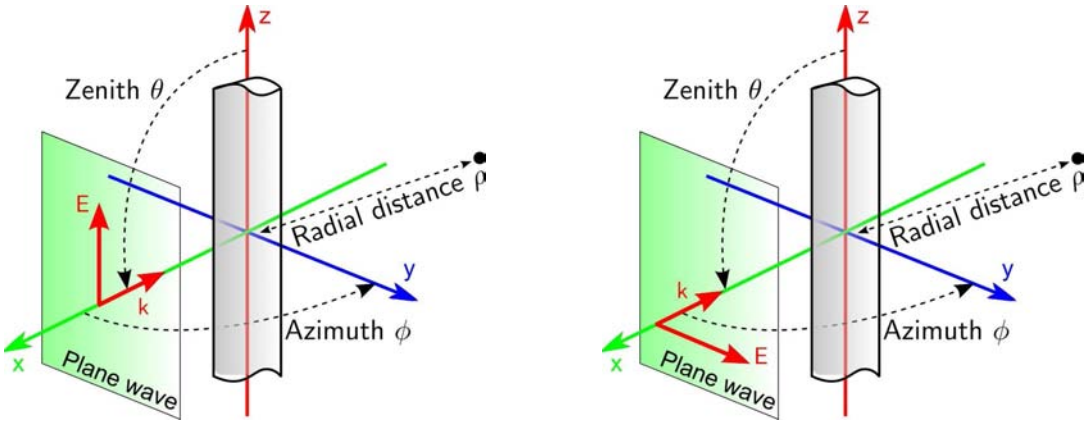

(a) Infinite right circular cylinder orientated parallel to the incident beam (TM)

(b) Infinite right circular cylinder orientated perpendicular to the incident beam (TE)

Figure 8.1: Schematic diagram of cylinders' orientations with respect to the THz polarisation. (a) An infinite right circular cylinder illuminated by a plane wave at $\theta = 90°$, with propagation vector $\mathbf{k}$ normal to the long axis of the cylinder (z-axis). The electric field vector $\mathbf{E}$ is parallel to the z-axis—this direction is termed *parallel* in this Thesis. (b) If the cylinder is rotated by 90°, then its long axis is now the y-axis. Vector $\mathbf{k}$ remains in the same direction but $\mathbf{E}$ is now normal to the y-axis—this is referred to as the *perpendicular* orientation in this Thesis. After Bohren and Huffman (1983)

8.3.2 Analytical (Exact) Solutions for Mie Scattering

Analytical (exact) solutions for Mie scattering—of which Rayleigh scattering is a special case where object size $\ll \lambda$—can be found in numerous pieces of literature (van de Hulst 1957, Kerker 1969, Bohren and Huffman 1983). A summary of salient equations is provided as follows. With reference to Fig. 8.1, when an electromagnetic wave $\mathbf{E}_{\text{inc}}$ propagating in a medium with complex refractive index $\hat{n}_i$ is incident normal ($\theta = 90°$) to the long (z) axis of an infinitely long cylinder with complex refractive index $\hat{n}_t$, some of the incident wave's power is scattered back by the target object ("backscatter"). The measure of this backscattered power is the scattering cross section C_{sca} (units: m^2), which is analogous to the monostatic radar cross section (or echo area) (Knott *et al.* 2004). The backscattering cross sections for the parallel and perpendicular cases are defined in Equations (8.1) and (8.2):

$$C_{\text{sca},\parallel} = \frac{4l}{k}\left[|b_{0,\parallel}|^2 + 2\sum_{s=1}^{\infty}|b_{s,\parallel}|^2\right] \tag{8.1}$$

$$C_{\text{sca},\perp} = \frac{4l}{k}\left[|a_{0,\perp}|^2 + 2\sum_{s=1}^{\infty}|a_{s,\perp}|^2\right] \tag{8.2}$$

$$a_{s,\perp} = \frac{\left[\frac{D_s(mkr)}{m} + \frac{s}{kr}\right] J_s(kr) - J_{s-1}(kr)}{\left[\frac{D_s(mkr)}{m} + \frac{s}{kr}\right] H_s^{(1)}(kr) - H_{s-1}^{(1)}(kr)} \tag{8.3}$$

$$b_{s,\parallel} = \frac{\left[mD_s(mkr) + \frac{s}{kr}\right] J_s(kr) - J_{s-1}(kr)}{\left[mD_s(mkr) + \frac{s}{kr}\right] H_s^{(1)}(kr) - H_{s-1}^{(1)}(kr)} \tag{8.4}$$

$$D_s(mkr) = \frac{J_s'(mkr)}{J_s(mkr)}, \tag{8.5}$$

where wavenumber $k = 2\pi/\lambda$, r = cylinder's radius, l = cylinder's length, $\hat{n} = n - i\kappa$, n = real component of the refractive index, κ = imaginary component of the refractive index or absorption index = $\alpha\lambda/(4\pi)$, α= absorption coefficient, $m = \hat{n}_t/\hat{n}_i$, $J_s(p)$ and $Y_s(p)$ are the Bessel functions of the first and second kind respectively with integral order $s \in \mathbb{R}$, $J_s'(p)$ is the first derivative of $J_s(p)$, and $H_s^{(1)}(p) = J_s(p) + iY_s(p)$ is the Hankel function.

In literature relevant to scattering, there is generally no distinction made between the effective and the bulk refractive indices of a material, regardless of the material's shape or size (van de Hulst 1957, Kerker 1969, Bohren and Huffman 1983). In Kerker (1969), examples seem to suggest the use of the bulk refractive index. In this study, the real and imaginary components of the refractive index, n and κ respectively, are treated as being equal to those of the bulk material. The reason for this choice is elaborated on in Section 8.5.2.

In addition to $C_{sca,\parallel}$ and $C_{sca,\perp}$, the relationship between the amplitude of E_{inc} and the scattered field $E_{sca}\ \forall\ \Theta = \pi - \phi$ for both the parallel and perpendicular cases can be defined as:

$$\begin{bmatrix} E_{sca,\parallel} \\ E_{sca,\perp} \end{bmatrix} = e^{\frac{i3\pi}{4}} \sqrt{\frac{2}{\pi k\rho}}\, e^{ik\rho} \begin{bmatrix} T_1 & 0 \\ 0 & T_2 \end{bmatrix} \begin{bmatrix} E_{inc,\parallel} \\ E_{inc,\perp} \end{bmatrix} \tag{8.6}$$

$$T_1 = \sum_{s=-\infty}^{\infty} b_{s,\parallel}\, e^{-is\Theta} = b_{0,\parallel} + 2\sum_{s=1}^{\infty} b_{s,\parallel} \cos(s\Theta) \tag{8.7}$$

$$T_2 = \sum_{s=-\infty}^{\infty} a_{s,\perp}\, e^{-is\Theta} = a_{0,\perp} + 2\sum_{s=1}^{\infty} a_{s,\perp} \cos(s\Theta), \tag{8.8}$$

where ρ = radial distance from the origin. Radiation patterns of $E_{sca,\parallel}$ and $E_{sca,\perp}$ at different values of frequency will be plotted in Section 8.6.

8.4 Fibrillar Samples and Experiment

The transmission mode time domain spectroscopy (TDS) THz system used in the experiments described in this Chapter is based on the generation of a THz pulse using

an ultrafast (90 fs) near-infrared laser (Spectra Physics Tsunami) and a photoconductive antenna, with coherent detection via electro-optic (EO) sampling. As this system utilises a photoconductive antenna emitter and an EO detector, its 'emission front end' is similar to that shown in Fig. 3.1(b), whereas its 'detection back end' is similar to that in Fig. 3.1(a). The THz beamwidth is ≈ 5 mm based on estimations with an iris placed in the path of the THz beam prior to the commencement[69] of measurements.

Recalling Fig. 5.2(b), identification of the system bandwidth aids in confidently determining the range of frequencies over which measurements are valid. In accordance with the techniques discussed in Section 5.2.2, the system bandwidth spans from ≈ 0.2–2.5 THz.

Cylindrical (fibrillar) scatterers used in this study are made from fibreglass strands obtained from woven fibreglass cloth (plain weave E-glass[70] with weight 7.5 oz/yd^2) as shown in Fig. 8.2(a). Each fibreglass strand is approximately 10 μm in diameter and 15 mm long. Since the length of each strand is 1500 times larger than the diameter, then each strand is an infinite cylinder according to the definition given in Section 8.3.1. The strands are aligned in a single layer with each strand placed as close as possible to its adjacent strands, creating a *near-periodic* array as shown in Fig. 8.2(b). The term *near-periodic* is used as it is acknowledged that some imperfections exist in the structure. These imperfections are taken into consideration later in Section 8.7.

Four identical arrays are built in this study. Each array is clamped between two polyethylene frames with a rectangular aperture of size 20 mm$\times$21 mm. By using the frame as shown in Fig. 8.2(c), the array is only exposed to air in the region of the incident THz beam. One of the polyethylene frames is covered with aluminium foil to prevent transmission of THz through the frames. As illustrated in Fig. 8.2(d), the incident THz beam is vertically polarised with respect to the z-axis of the sample, which is orthogonal to the surface of the optical bench. The array is placed orthogonally in the path of beam in either the parallel or perpendicular orientation as discussed in Section 8.3.1. The four arrays built for this study can be used in either orientation.

[69] The eye of the iris is enlarged during measurements to avoid diffraction of the THz beam.
[70] E-glass is electrical grade glass.

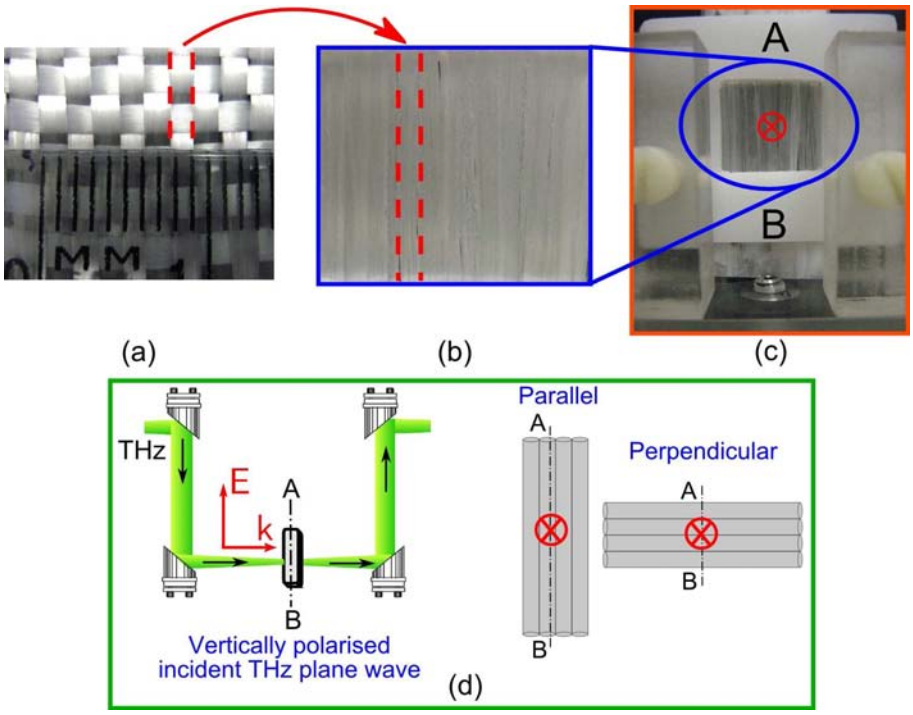

Figure 8.2: Experimental setup. (a–b) Strands of fibreglass are taken from woven fibreglass cloth, and aligned as a near-periodic array. (c) The array is clamped between two polyethylene frames, with a rectangular aperture of size 20 mm×21 mm. One of the polyethylene frames is covered with aluminium foil to prevent transmission of THz through the frames. The frame is placed orthogonal to the incident THz beam, which is vertically polarised with respect to the z-axis of the sample. The z-axis of the sample is orthogonal to the surface of the optical bench. The red circle with a cross illustrates the cross-section of the incident THz beam with respect to the plane of the array, i.e. the incident THz beam travels into the plane of the array. The THz beamwidth is $\approx$ 5 mm based on estimations with an iris placed in the path of the THz beam prior to commencement of measurements. (d) The frame is placed orthogonal to the incident THz beam, which is vertically polarised (i.e. the same orientation as the A-B line). The parallel and perpendicular orientations of the arrays with respect to the THz beam are as shown.

8.5 Experimental Results

Experimental results presented in this Section are verified using two different THz-TDS systems (at the University of Adelaide, and the University of Leeds). Each THz measurement is averaged between 16 to 25 scans.

The THz frequency responses of two of the four fibreglass array samples are presented in Figure 8.3(a). Calculations of the THz frequency response are performed using Equation (5.3). The measured optical properties are presented in Figures 8.3(b)

and 8.3(c). The calculations of absorption coefficient and refractive index are based on Equations (5.21) and (5.22) respectively. In accordance with the notation used in Section 7.5, the term *extinction coefficient* is used henceforth instead of *absorption coefficient* because both absorption and scattering effects are present.

8.5.1 Observations From the Perpendicular Samples

The two samples perpendicular to the THz beam have very similar THz frequency responses. The similarity is also evident in their extinction coefficients. The profiles of their real refractive indices n is fairly flat, varying only slightly over the frequencies of interest (sample 1: $n_{\perp} = 1.71$ at 0.5 THz; 1.63 at 2 THz).

8.5.2 Observations From the Parallel Samples

Both parallel samples block more THz transmission than the perpendicular samples, suggesting agreement with the filtering capabilities of grid arrays, such as wire grid arrays in the transverse magnetic (TM) orientation (Hecht 2002). However, the two parallel samples have differing THz frequency responses, resulting in differing extinction coefficient profiles. Sample 1 not only appears to block more THz transmission, its extinction coefficient profile slopes downwards beyond 2 THz. This slope is not observed in sample 2. Visual checks of both samples do not reveal any significant physical variations in the two samples. Repeat measurements of all four samples in the both orientations reveal similar inconsistencies for the parallel orientation.

The decrement in the extinction coefficient profile of sample 1 occurs within the estimated system bandwidth of $\approx$ 0.2–2.5 THz, hence it can be argued that the decrement is not an artefact of the THz-TDS system. However, observation of all four plots over a wider range of frequencies as presented in Fig. 8.4(a) reveals all plots have the same trend as sample 1 at higher frequencies, suggesting that the decrement in the extinction coefficient profile is an artefact. Further investigations are necessary to ascertain if the sloping feature is an artefact, and to answer the question as to why the parallel orientation appears more susceptible to inconsistencies. Outcome of investigations will be presented in Section 8.8.

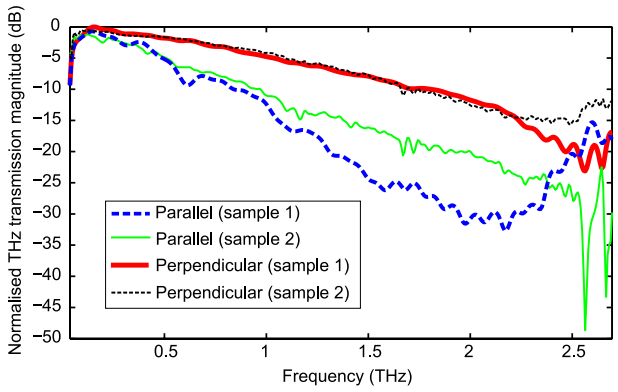

(a) Measured THz transmission magnitudes (normalised) of the arrays

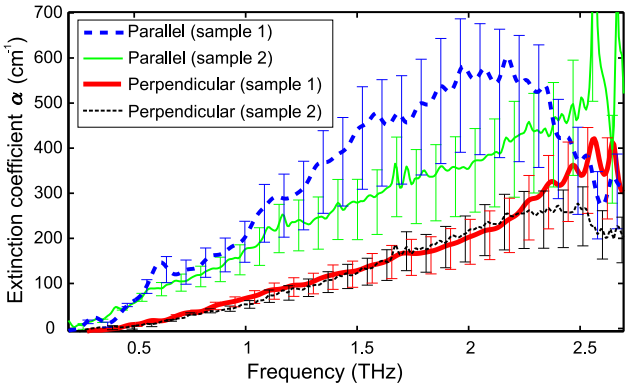

(b) Measured extinction coefficients α of the arrays

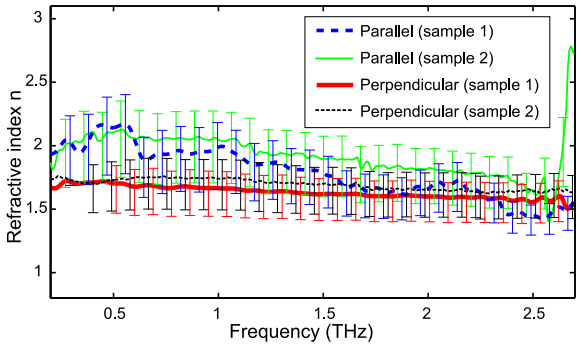

(c) Measured real refractive indices n of the arrays

Figure 8.3: Experimental results. (a) Terahertz transmission magnitudes (normalised) of two of the four arrays. The perpendicular arrays have similar magnitudes, unlike the parallel arrays where the magnitudes vary from sample to sample. (b) The measured extinction properties α. The error bars account for uncertainties in the samples' thicknesses when substituted into Equation (5.21). For sample 1, its α plot changes directions beyond 2 THz, raising the question of whether this change is an artefact. (c) The measured refractive indices n of the fibreglass arrays varies slightly between the two orientations, suggesting birefringence.

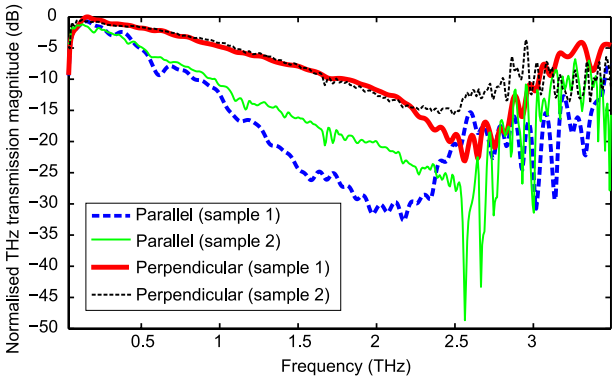

(a) Observations over a wider range of frequencies

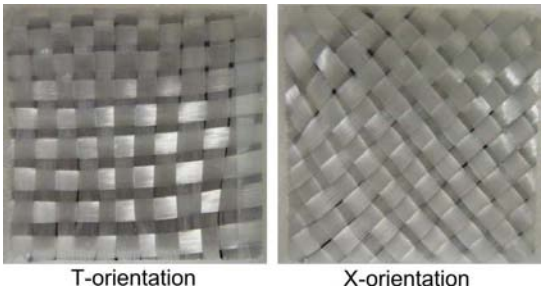

(b) Two possible orientations of bulk fibreglass cloth encountered by the incident THz beam

Figure 8.4: Plots over a wider range of frequencies. (a) When the arrays' THz transmission magnitudes (normalised) are observed over a wider range of frequencies, the slopes of all plots behave similarly to that of sample 1, changing directions at higher frequencies. This may indicate the regions after the turning points are not valid for analysis. (b) Bulk fibreglass cloth is measured in order to derive optical properties that are independent of orientation. However, some birefringence is also observed between the T- and X-orientations.

The parallel arrays have uneven n profiles that vary more over frequency (sample 1: $n_{\parallel} = 2.13$ at 0.5 THz; 1.74 at 2 THz), indicating dispersion in the fibreglass strands. The difference in refractive index between the parallel and perpendicular orientations suggests that the strands are birefringent. Furthermore, given the more significant increase in extinction for the parallel samples, the strands may also be dichroic. Alternatively, the increase in α could be due to strong THz scattering in this orientation.

In order to determine if scattering causes the increase in α for the parallel orientation, and to investigate why the two parallel samples have differing transmission profiles, $C_{\text{sca},\parallel}$ and $C_{\text{sca},\perp}$ in Equations (8.1) and (8.2) are investigated in the next Section, allowing comparison between α, $C_{\text{sca},\parallel}$ and $C_{\text{sca},\perp}$.

8.6 Comparison of Experimental and Analytical Results

In order to solve for $C_{\text{sca},\parallel}$ and $C_{\text{sca},\perp}$ in Equations (8.1) and (8.2), knowledge of $\hat{n}$ is needed for m in Equations (8.3–8.5). The orientation dependence of n and α complicates the substitution of a suitable $\hat{n}_t$ value into m because the use of two different sets of optical properties could bias the analytical results. One possible alternative is to

substitute the n and α values from fibreglass strands with those of bulk glass reported in literature. A second alternative is to use n and α of bulk fibreglass cloth.

8.6.1 Optical Properties of Bulk Glass

Properties of a wide range of bulk glass ranging from optical grade glass to commercially available window glass has been reported in literature. Optical grade glass, such as BK7, is been reported to have $n = 2.5$, $\kappa = 0.043$ at 1 THz; Pyrex is reported to have $n = 2.1$, $\kappa = 0.036$ at 1 THz (Naftaly and Miles 2005). Commercially available window glass is reported to have $n = 2.6$, $\kappa = 0.060$ at 0.2 THz, and $n = 2.6$, $\kappa = 0.089$ at 0.35 THz (Piesiewicz *et al.* 2005). Bulk silica is reported to have $n = 1.95$, $\kappa = 0.003$ at 0.5 THz, and $n = 1.963$, $\kappa = 0.006$ at 1 THz (Naftaly and Miles 2007b), whereas Kojima *et al.* (2005) has reported the optical properties of bulk silica as $n = 1.98$, $\kappa = 0.002$ at 0.5 THz, and $n = 1.98$, $\kappa = 0.006$ at 1 THz.

8.6.2 Optical Properties of Bulk Fibreglass Cloth

The number of publications related to bulk fibreglass cloth is sparse, hence measurements of bulk fibreglass cloth are included in this study to supplement existing data. As shown in Fig. 8.4(b), the orientation of bulk fibreglass cloth needs to be considered should birefringence exist between the T- and X-orientations because a small difference in n can be observed. Since this study relates to fibreglass strands that are oriented parallel and perpendicular to the THz beam, only the T-orientation is considered. The optical properties of bulk fibreglass cloth measured in this study are: (at 0.2 THz) $n = 2.1$, $\kappa = 0.096$, or expressed as electric permittivity $\epsilon' = 4.401$, $\epsilon'' = 0.401$; (at 1 THz) $n = 1.95$, $\kappa = 0.287$, $\epsilon' = 3.72$, $\epsilon'' = 1.117$. The real and imaginary permittivities (ϵ' and ϵ'' respectively, $\epsilon' - i\epsilon'' = (n - i\kappa)^2$) are lower than those reported in Naito *et al.* (2009a); the difference is possibly due to the use of plain weave E-glass cloth in this study, whereas eight-harness-stain E-glass cloth with unreported orientation is used in Naito *et al.* (2009a).

8.6.3 Comparison of Bulk Optical Properties

A comparison of the optical properties of the various types of bulk glass with that of bulk fibreglass glass measured in this study reveals that the real refractive indices

n are similar, but the measured imaginary component κ is one order of magnitude higher. However, when only fibreglass cloth measurements are compared, measurements from this study are slightly lower than those obtained by Naito *et al.* (2009a). This indicates that the measurements made in this study are valid as they are within the reported range for bulk glass and fibreglass cloth in literature.

The significant difference in optical properties between bulk glass and fibreglass cloth suggests that fibreglass cloth strongly scatters THz radiation. Given that this study utilises strands from fibreglass cloth, the use of optical properties from bulk fibreglass cloth is preferred over those of bulk glass.

8.6.4 Scattering Cross Section

Due to the small dimension of each fibreglass strand, it is found that there is no observable change in $C_{\text{sca},\parallel}$ and $C_{\text{sca},\perp}$ regardless if the optical properties are derived from the parallel strands, perpendicular strands, T-orientated or X-orientated bulk fibreglass cloth. Nonetheless, the usefulness of the bulk fibreglass cloth optical properties will become apparent in Section 8.7.

Figure 8.5(a) presents resultant $C_{\text{sca},\parallel}$ and $C_{\text{sca},\perp}$ plots for $\mathbf{E}_{inc}$ polarised parallel to the z-axis in Fig. 8.2, and $E_{\text{inc}} = 1$ V. For the frequencies under investigation $C_{\text{sca},\perp} \ll C_{\text{sca},\parallel}$. This means that a fibre oriented perpendicular to the incident E field has a much smaller scattering area than one that is oriented parallel to E. In accordance with the definition of scattering cross section in Section 8.3.2, a smaller scattering area implies that a weaker signal is scattered back to the illumination source, resulting in a stronger transmitted signal. This trend is supported by the far-field[71] radiation patterns of E_{sca} as defined in Equation (8.6). Radiation patterns of E_{sca} for $-180^\circ \leq \phi < 180^\circ$ using Equation (8.6) are plotted in Fig. 8.6; the maximum scattering magnitude for the perpendicular case is at least 20 dB lower than for the parallel case for all frequencies. The results of $C_{\text{sca},\parallel}$, $C_{\text{sca},\perp}$, and E_{sca} are consistent with the observations in Figs. 8.3(a) and 8.3(b) where lower material extinction α for the perpendicular case results in the detection of a stronger transmitted THz signal.

[71] Calculated at the far-field radial distance $\rho = 1$ mm from the origin as shown in Fig. 8.1. This distance is greater than the Fraunhofer diffraction region $2A^2/\lambda_{\text{min}}$ (Balanis 1989), where aperture A is taken as the length $l = 100$ μm of a cylinder, and $\lambda_{\text{min}} = 0.1$ mm. Modifying ρ in the calculations results in the scaling of the scattering magnitudes without affecting the shape of the patterns, indicating that the Mie scattering equations are only valid for far-field analysis.

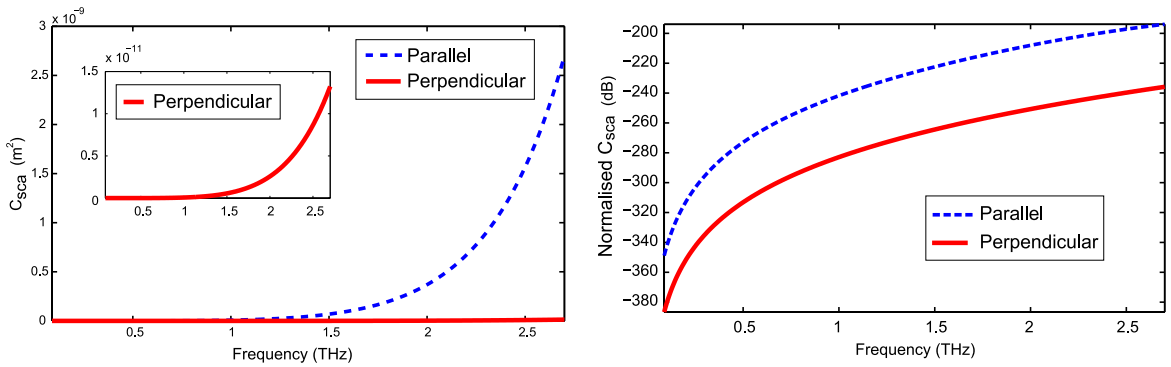

(a) $C_{sca,\parallel}$ and $C_{sca,\perp}$ plotted on a linear scale

(b) $C_{sca,\parallel}$ and $C_{sca,\perp}$ plotted on a logarithmic scale

Figure 8.5: Calculated $C_{sca,\parallel}$ and $C_{sca,\perp}$. (a) To determine if the large difference in α is due to material absorption or scattering from the material, $C_{sca,\parallel}$ and $C_{sca,\perp}$ are found. The steep rise in $C_{sca,\parallel}$ is similar to the rise in α, suggesting that scattering is the dominant cause of THz signal loss in the arrays. (b) $C_{sca,\parallel}$ and $C_{sca,\perp}$ normalised by 1 m^2, and plotted on a logarithmic y-axis.

The radiation patterns also reveal that for the frequencies under investigation, scattering is nearly isotropic for the parallel case—this is consistent with antenna theory for an isotropic point source radiating in space. For the perpendicular case, there is strong forward scatter (towards 180°) at lower frequencies, but increasing backscatter (towards 0°) at the higher frequencies.

8.6.5 Modelling an Array with Analytical Solutions

The analytical model presented thus far only accounts for one cylinder, whereas the experiments presented in this Chapter involves multiple cylinders. In one technique used to model multiple scatterers, Mie scattering equations are usually multiplied by a scaling factor equal to the number of scatterers under test (Bandyopadhyay *et al.* 2007, Png *et al.* 2009a), assuming constructive interference from all scatterers. However, when a scaling factor is applied to both plots in Fig. 8.5(a), the resulting plots still do not resemble the measurements in Fig. 8.3(b).

An alternative technique for accounting for multiple scatterers is to use antenna array models, such as the array factor (AF) for N isotropic sources (Balanis 1989):

$$\mathrm{AF} = \sum_{s=1}^{N} e^{i(s-1)[kd\cos(\phi)+\beta]} \tag{8.9}$$

$$C_{\text{sca, total}} = C_{\text{sca, single}} \times \mathrm{AF}, \tag{8.10}$$

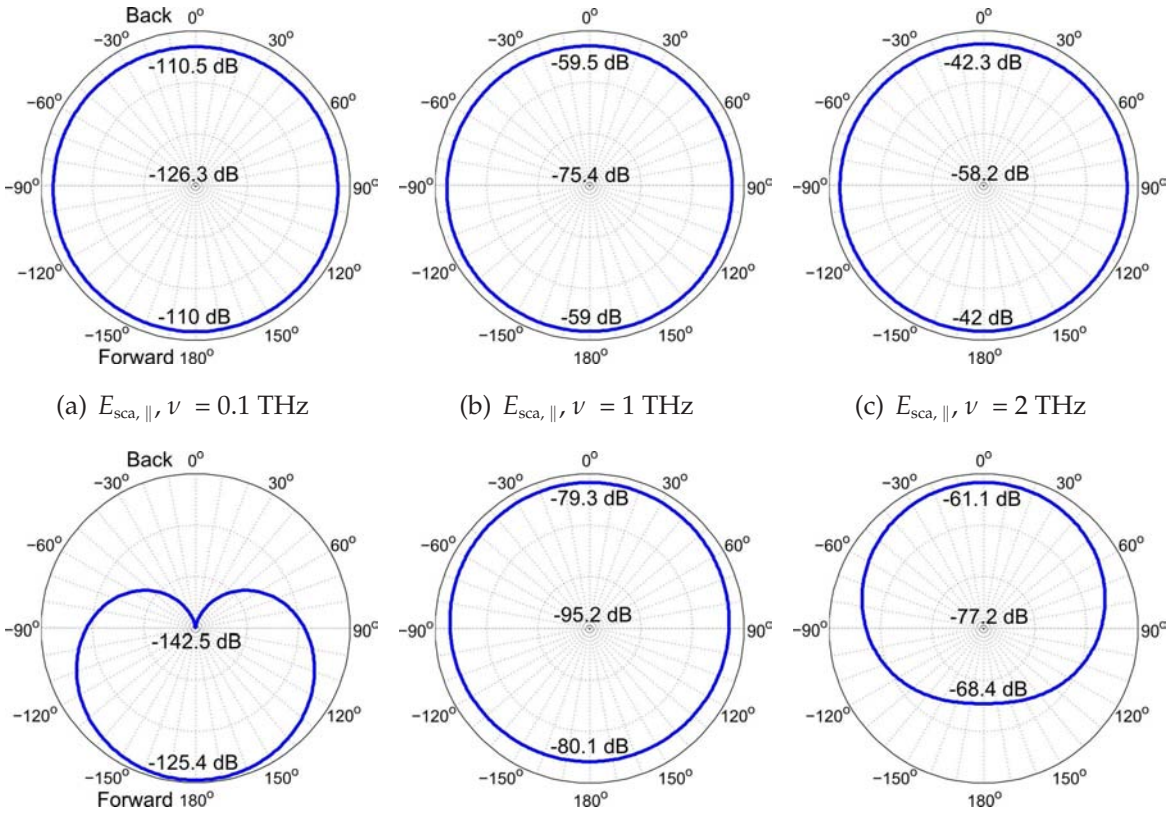

(a) $E_{\text{sca},\parallel}, \nu = 0.1$ THz (b) $E_{\text{sca},\parallel}, \nu = 1$ THz (c) $E_{\text{sca},\parallel}, \nu = 2$ THz

(d) $E_{\text{sca},\perp}, \nu = 0.1$ THz (e) $E_{\text{sca},\perp}, \nu = 1$ THz (f) $E_{\text{sca},\perp}, \nu = 2$ THz

Figure 8.6: Far-field radiation patterns. Radiation patterns of unnormalised $E_{\text{sca}}(\phi, \omega)$ as defined in Equation (8.6) for $-180° \leq \phi < 180°$, $\theta = 90°$, at three THz frequencies ν, for both the parallel $\parallel$ and perpendicular $\perp$ orientations as shown in Fig. 8.1. The scale of each pattern is ≈ 27 dB from maximum to minimum. The backscatter direction (location of incident plane wave) is 0°; the forward scatter direction (location of the detector) is 180°. The radiation patterns of $E_{\text{sca},\parallel}$ are nearly isotropic for the range of frequencies under investigation, indicating that there is almost equal scattering in both the forward and backward directions. The radiation patterns of $E_{\text{sca},\perp}$ are less isotropic, with increasing forward scatter as the wavelength λ increases (ν decreases).

where $k = 2\pi\nu\sqrt{\epsilon_t\mu_t} = 2\pi\nu\hat{n}_t\sqrt{\epsilon_0\mu_0\mu_r}$, d is the distance between adjacent scattering sources, β is the difference in phase excitation between adjacent scattering sources, ϕ is the azimuth (with -90° being the forward scatter direction, and 90° being the backscatter direction), ϵ_0 is the electric permittivity *in vacuo*, μ_0 is the magnetic permeability *in vacuo*, and $\mu_r = 1$ is the relative magnetic permeability of fibreglass. Assuming that all the fibreglass strands are excited simultaneously by the incident THz plane wave, then $\beta = 0$.

An AF radiation pattern modelled using $\nu = 2$ THz and $d = 1$ μm ($\approx \lambda_{min}/100$, where $\nu_{max} = 2.788$ THz), and the plot of $C_{sca,\,total}$ are presented in Fig. 8.7. The effect of multiplying C_{sca} by AF becomes evident when Figs. 8.5(a) and 8.7(b) are compared, showing that AF scales C_{sca} up by two orders of magnitude. The inclusion of AF still does not explain the dip in α above $\nu = 2$ THz for the parallel case (Fig. 8.3(b)). The difference may be due to the small dimension of d in this study, which is estimated to be $\lambda/150$ at 2 THz compared to most antenna applications that utilise $d = \lambda/2$ or $\lambda/4$; hence the models for AF may be inaccurate at $\lambda/150$. Furthermore, AF does not account for the polarisation of $\mathbf{E}_{inc}$, the cylinders' extinction properties α (or κ), nor slight misalignments in the array. We conclude, therefore, that the inclusion of AF is probably inadequate for modelling THz scattering for the test scenarios presented in this study.

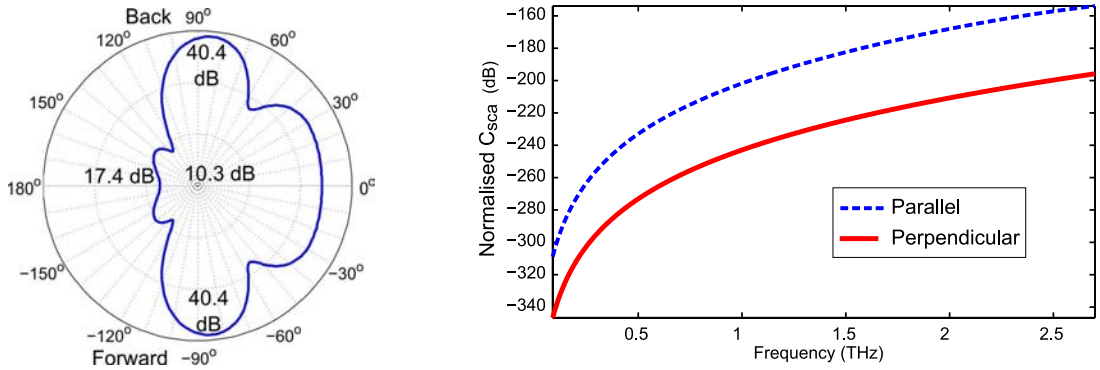

(a) AF radiation pattern of $N = 100$ isotropic sources, $\beta = 0$, $\nu = 2$ THz, $d = 1$ μm

(b) Scattering cross sections $C_{sca,\parallel}$ and $C_{sca,\perp}$ multiplied by AF; the result is a scaling effect across all frequencies

Figure 8.7: Influence of array factor on C_{sca}. (a) The directions of forward and backscatter are -90° and 90° respectively. The array factor (AF) accounts for multiple scatterers in an array. (b) Despite the unique radiation pattern of AF, when compared with Fig. 8.5(b), multiplying C_{sca} by AF only results in a scaling effect across all frequencies.

8.6.6 Limitations of the Analytical Solutions

Although the trend in Fig. 8.5(a) is consistent with that in Fig. 8.3(b), the relative difference between $C_{sca,\parallel}$ and $C_{sca,\perp}$ is exaggerated in the analytical model. Furthermore, the analytical model neither satisfactorily explains why the measured α differ for the two parallel cases, nor verifies if the decrement in α for sample 1 from 2 THz onwards is an artefact (Section 8.5.2).

These gaps[72] in the analytical model motivate use of a numerical electromagnetic simulation tool to model mutual coupling between array elements. In the next Section, a full-wave electromagnetic field simulation is presented. This electromagnetic simulation tool allows for a more thorough analysis of scattering, resulting in a better match between the simulation and the experimental observation.

8.7 Full-Wave Electromagnetic Field Solver

The High Frequency Structure Simulator (HFSS, versions 10.1 and 11, produced by Ansoft) is an electromagnetic field simulator that utilises the Finite Element Method (FEM) as a three dimensional (3D) full-wave numerical solver of Maxwell's equations. The FEM solver finely meshes the virtual problem space to achieve accuracy, but this often leads to heavy utilisation of available random access memory (RAM) on a computer. In order to significantly reduce memory use, symmetry and periodicity can be applied in HFSS. This is a practice that has been used by other authors investigating periodic structures in the microwave and THz frequency ranges (Chattopadhyay *et al.* 2003, Liu *et al.* 2005, Makarov and Puzella 2007).

8.7.1 The HFSS Model

Figure 8.8(a) shows a HFSS model which utilises symmetric and periodic boundaries to represent a test environment containing many infinitely long fibreglass strands. Since the far-field response is of interest in this study, the incident THz beam is modelled in HFSS as a plane wave as described in Fig. 8.2 instead of as a Gaussian beam.

The walls of the vacuum airbox that are parallel to the y-z plane are at a distance of $\lambda_{max}/2$ away from the cylinders, where $\nu_{min} = 0.088$ THz. As illustrated in Figs. 8.8(b) and 8.8(c), these walls are assigned perfectly matched layers (PML) as boundaries in order to reduce the problem space. However, due to limitations inherent in HFSS, the PML boundaries excludes the airbox from being used for far-field calculations. In order to create a suitable surface for far-field calculations, a second vacuum airbox is used. Not visible in Fig. 8.8(a) is the second, shorter (along the x-axis) airbox seated

[72] Another gap in our knowledge is the inability to analyse near-field behaviour using Mie scattering theory, although other analytical models may exist for the near-field. Near-field studies are outside the scope of this Thesis.

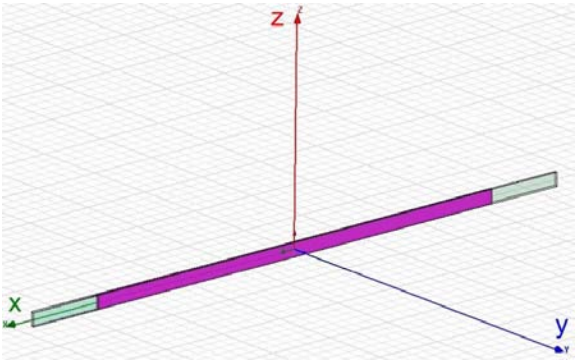

(a) HFSS simulation with airbox highlighted

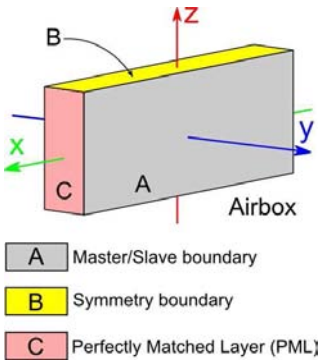

(b) Schematic of radiation boundaries

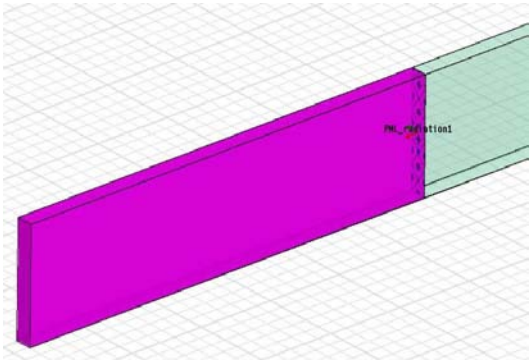

(c) PML boundary with corresponding PML box highlighted

Figure 8.8: Near-periodic HFSS model and its radiation boundaries. (a) Overview of the HFSS simulation with the cylinders located about the origin, and the surrounding airbox highlighted. The airbox walls which are parallel to the y-z plane are $\lambda_{max}/2$ away from the cylinders. (b) Three different radiation boundaries are used on the airbox. The master/slave boundaries create the periodic effect; the symmetry boundaries give the cylinders the infinitely long effect; the PML boundaries reduce the problem space. (c) One of the two PML boundaries with depth of $\lambda_{max}/6$; this depth ensures that fields at the PML boundaries do not reflect back into the problem space.

tightly inside the first airbox. This airbox is similar in shape to the first, except the walls that are parallel to the y-z plane are at a shorter distance ($\lambda_{max}/2.05$) from the cylinders, meaning they do not touch the PML boundaries. None of the walls of the second airbox are assigned specific boundary types.

The 0.05 factor used in the length of the second airbox (i.e. the difference in the denominators of $\lambda_{max}/2.05$ and $\lambda_{max}/2$) is chosen because it is a small number. If another small number is used, such as 0.01, similar results are generated.

As illustrated in Figs. 8.9(a) and 8.9(b), this HFSS model contains a vacuum airbox containing two 100 μm long strands (each 10 μm in diameter) seated between periodic master/slave side boundaries. Two strands are used in order to account for the imperfection in aligning the fibreglass strands, such as a slight offset between adjacent strands as shown in Fig. 8.9(c).

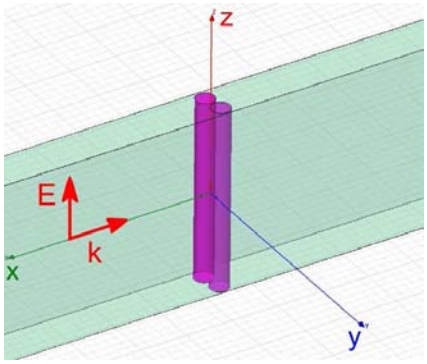

(a) Parallel case

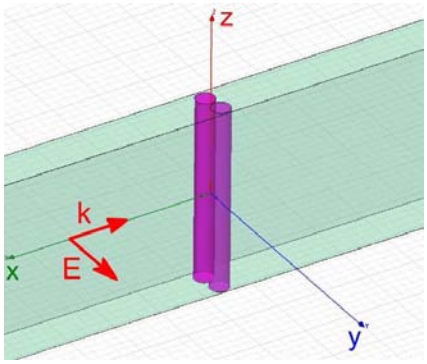

(b) Perpendicular case

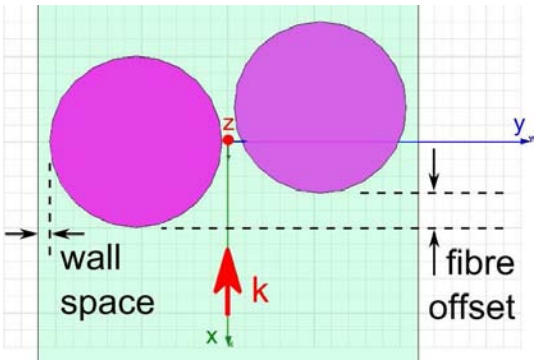

(c) Offset between adjacent fibres

Figure 8.9: Near-periodic cylindrical array in airbox. (a–b) Zoomed view showing two cylinders enclosed inside the airbox. The two airbox walls that lie parallel to the x-z plane are assigned master/slave boundaries in order to model the periodic array that extends all along the y-z plane. In order to model each cylinder's infinite length with respect to its diameter, the walls parallel to the x-y plane are assigned symmetrical $\mathbf{E}$ boundaries for the parallel case (symmetrical $\mathbf{H}$ for the perpendicular case). (c) Plan view of the double cylinder structure with a 2 μm offset to account for misalignments in the fibreglass array used in the THz experiment. To create a small 1 μm gap between adjacent cylinders, a 0.5 μm wallspace is introduced between each cylinder and the airbox walls which are parallel to the x-z plane. These walls are assigned master/slave boundaries so that the double cylinder structure is repeated along the y axis.

To create the infinitely long cylinders along the z-axis, symmetrical boundaries are applied to the top and bottom airbox walls which touch the ends of the cylinders (symmetrical **E** for the parallel case; symmetrical **H** for the perpendicular case). Given that HFSS utilises a 3D solver, the symmetrical boundaries also serve the dual purpose of reducing the problem space into a 2D one, simplifying and speeding up the simulation. The boundaries used around the airbox are illustrated in Fig. 8.8(b).

8.7.2 Calculation of S-Parameters

One advantage of HFSS is that it allows the reflection and transmission characteristics of the model to be extracted in terms of the S-parameters S_{11} and S_{21}, which are the reflection and transmission coefficients respectively. The coefficient S_{11} has the same meaning as the Fresnel reflection coefficient R, whereas the coefficient S_{21} has the same meaning as the Fresnel transmission coefficients T (Orfanidis 2008). Both R and T are defined in Balanis (1989) either in terms of the electric field E or magnetic field H of a plane wave transmitting at normal incidence angle from medium 1 into medium 2:

$$R = \frac{\eta_2 - \eta_1}{\eta_2 + \eta_1} = \frac{E_{\text{reflected}}}{E_{\text{incident}}} = -\frac{H_{\text{reflected}}}{H_{\text{incident}}} \tag{8.11}$$

$$T = \frac{2\eta_2}{\eta_1 + \eta_2} = \frac{E_{\text{transmitted}}}{E_{\text{incident}}} = \frac{\eta_2 H_{\text{transmitted}}}{\eta_1 H_{\text{incident}}}, \tag{8.12}$$

$$\text{where} \quad \eta_1 = \sqrt{\frac{\mu_1}{\epsilon_1}}, \quad \eta_2 = \sqrt{\frac{\mu_2}{\epsilon_2}}.$$

The S-parameters S_{11} and S_{21} are usually expressed in decibels, whereas R and T are usually expressed linearly.

As shown in Fig. 8.10, the values of S_{11} describe backscattering, whereas the values of S_{21} describe transmission; S_{21} therefore provides a means for elucidating the behaviour of the α plots in Fig. 8.3(b). If $S_{21} = 1$ (or $S_{21} = 0$ dB), then the incident THz signal is 100% transmitted, implying $\alpha \to 0$. If $S_{11} = 1$ (or $S_{11} = 0$ dB), then the signal is 100% reflected, implying $\alpha \to \infty$. In an ideal condition with no losses and no gain, $|S_{21}|^2 + |S_{11}|^2 = 1$, reverse transmission $S_{12} = 0$, and output reflection $S_{22} = 0$.

The next Section presents the S-parameters from the model in Fig. 8.8 and compares them with the measured THz transmission magnitudes. To verify the consistency of the model shown in Fig. 8.8, Section 8.9 compares the S-parameters from the model

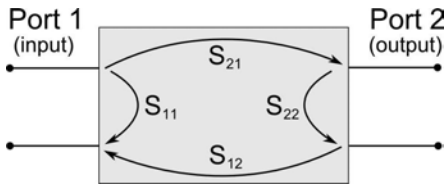

Figure 8.10: S-parameters of a 2 port network. The coefficient S_{11} describes backscattering, S_{21} describes transmission, S_{12} describes reverse transmission, and S_{22} describes output reflection.

in Fig. 8.8 with those generated by other HFSS models that contain structural variations. Finally, other types of reports generated by the HFSS program are presented in Section 8.9.1 to support and aid in elucidating the measurements.

8.8 Comparison of Experimental and Numerical Results

Simulations of the HFSS model described in Section 8.7 cover the frequency range from 0.088 THz to 2.788 THz, at a frequency resolution of 30 GHz. The mesh size on the side of each cylinder is set at one eighth the length of the cylinder; the mesh size at the top and bottom ends is set at a third of the cylinder's diameter. As a result, approximately 160,000 tetrahedra are created by HFSS to cover the problem space.

8.8.1 Shape of Plots at Lower THz Frequencies

Figure 8.11 presents the S_{21} results obtained with this model. Compared with the shape of the measured THz transmission magnitude in Fig. 8.3(a), it is evident that there is a good qualitative match between the S_{21} results for both the parallel and perpendicular cases with the measurements for all frequencies. This match is superior to the poor match between $C_{sca,\parallel}$ and $C_{sca,\perp}$ plots in Fig. 8.5(a) with the measured extinction coefficient in Fig. 8.3(b).

For the parallel case, the S_{21} plot also matches the shape of the THz transmission magnitude measurement more accurately for the lower THz frequencies; this is unlike the $C_{sca,\parallel}$, which is almost equal to zero for frequencies below 1 THz.

It is noted that when Figs. 8.3(a) and 8.11 are compared quantitatively, the magnitudes of the plots in Fig. 8.3(a) are approximately 10 to 15 times larger than those in Fig. 8.11. For example, the magnitude of the perpendicular sample at 1 THz in Fig. 8.3(a) is $\approx$ -5 dB, whereas the S_{21} value of the perpendicular sample in Fig. 8.11 is $\approx$ -0.5 dB. This difference may be due to overlapping cylinders in the arrays used in the THz

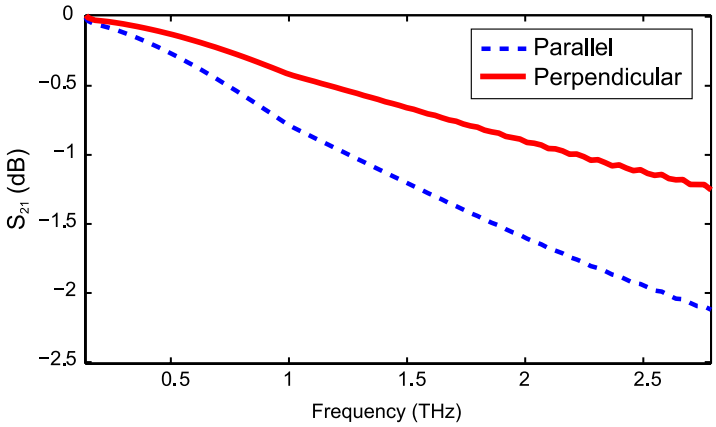

Figure 8.11: S_{21} plots for both orientations with 1 μm space between adjacent cylinders. The larger S_{21} values for the perpendicular case indicates stronger THz transmission than for the parallel case, agreeing well with the THz transmission magnitude plots in Fig. 8.3(a) particularly for frequencies below 1 THz.

measurements. Referring to Fig. 8.2(b), overlapping of the fine fibre threads is likely, therefore this hypothesis will be tested in Section 8.8.3.

8.8.2 Shape of Plots at Higher THz Frequencies

Referring to the parallel case in Fig. 8.11, the S_{21} plot still does not explain whether the curve seen in Fig. 8.3(a) after 2 THz for sample 1 in the parallel orientation is an artefact. To ascertain if the feature is an artefact, we explored the effect of changing the space between the cylinders in our HFSS simulation. This scenario is realistic, as the fibreglass strands are not secured very tightly to the polyethylene frame in order to prevent them from snapping. The strands may therefore have moved out of place prior to measurements, creating spaces between the strands that are wider than anticipated.

Two values, 5 μm and 10 μm, were arbitrarily chosen to examine the effect of varying the space between adjacent strands. The S_{21} plots generated from these new scenarios are presented together with the 1 μm case in Fig. 8.12. Comparing only the perpendicular cases, the S_{21} plots shift upwards as the strand spacing increases, with similar profiles except a change in gradient; the changes in gradients are less significant between the 5 μm and 10 μm cases than between the 1 μm and 5 μm cases. These observations for the perpendicular case suggests that the the fibreglass arrays in the perpendicular orientation are fairly robust to small changes to strand spacing, possibly explaining

why no difference in THz transmission magnitude is measured in Fig. 8.3(a) for the two perpendicular samples.

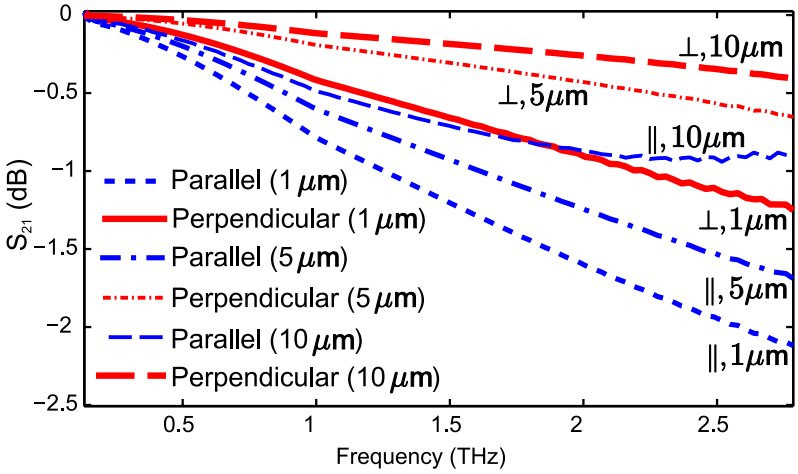

Figure 8.12: S_{21} plots for both orientations with 1, 5 and 10 μm spaces between adjacent cylinders. When the space between adjacent strands increases, the S_{21} plots for both orientations shift upwards, indicating stronger THz transmission due to 'leakage' through the wider spacing. However, the parallel case appears to be more sensitive to the change in strand spacing, shifting more significantly than for the perpendicular case. This resembles the inconsistencies seen in Fig. 8.3(a) for the two parallel samples.

Comparing only the parallel cases, the S_{21} plots also shift upwards as the strand spacing increases, but the extent of shifting and the changes in profiles are significantly different for the three strand spacings. The most significant change in profile is when the strand spacing is 10 μm: the S_{21} plot appears to plateau from 2 THz onwards. Comparing with the magnitude response of sample 1 in Fig. 8.3(a), the start of the plateau effect bears some resemblance to the start of the curve at 2 THz for the sample 1 magnitude plot in Fig. 8.3(a), but there is no evidence of a turning point in the S_{21} plot.

These observations for the parallel case suggests that *(i)* the fibreglass arrays in the parallel orientation are particularly sensitive to small changes in the strand spacing, manifesting as different THz transmission magnitudes as reported in Section 8.5.2 for the two parallel samples; *(ii)* the turning point seen in sample 1 in Fig. 8.3(a) cannot be reproduced in the HFSS model, hence it can be concluded that the upwards-turning curve beyond $\approx$ 2.2 THz in Fig. 8.3(a) is an artefact, possibly due to the noise floor of the THz system. However, the lower THz transmission magnitude of sample 1 when compared to sample 2 at 2 THz is well explained by the aforementioned sensitivity to strand spacing.

8.8.3 Influence of Overlapping Cylinders in the Array

As highlighted in Section 8.8.1, when Figs. 8.3(a) and 8.11 are compared quantitatively, the magnitudes of the plots in Fig. 8.3(a) are approximately five time larger than those in Fig. 8.11. This difference is hypothesised to be due to overlapping cylinders in the arrays used in the THz measurements.

To verify this hypothesis, a simple periodic model containing only one cylinder is compared with a second model containing two cylinders placed back-to-back in the airbox. The two models are as shown in Figs. 8.13(a) and 8.13(b). The reason why the models shown in Figs. 8.13(a) and 8.13(b) are used in this test is because the HFSS simulations run most efficiently in this study when up to two cylinders are used in the problem space. Simulations involving three and four cylinders are attempted, but errors in HFSS necessitated varying test variables, such as the wallspace distance, resulting in inconsistencies between the one-, two-, three- and four-cylinder models.

Figure 8.13(c) presents the S_{21} plots from the models in Figs. 8.13(a) and 8.13(b). At 1 THz, the difference between the two S_{21} plots is approximately 1.8 dB/0.8 dB ≈ 2. This suggests that each cylinder layer approximately doubles the S_{21} value across all THz frequencies. Referring to Figs. 8.3(a) and 8.11, the ≈ 4.5 dB difference at 1 THz suggests that there are at least 3-cylinder layers in the arrays. Therefore, the earlier assumption in Section 8.4 that the arrays consist of single layer of fibres is incorrect. By scaling the S_{21} plots in Fig. 8.11 by 10 to 15, the S_{21} values approach those in Fig. 8.3(a), allowing for a better quantitative match between the experimental and modelled results.

8.9 Verifying Consistency in Periodic Models

Although the good agreement between experimental and numerical results in Section 8.8.1 is encouraging, its success necessitates a check on whether the numerical result is biased by unexpected inconsistencies in the model and/or simulation. One check is to compare the numerical results obtained from the model in Fig. 8.8 with those generated by other HFSS models that vary slightly in their structures. For example, structures with only one cylinder, or having two cylinders but with no offset.

The first model to be compared with is shown in Fig. 8.14(a), which contains only one cylinder enclosed inside similar periodic and symmetric boundaries as Fig. 8.8. The

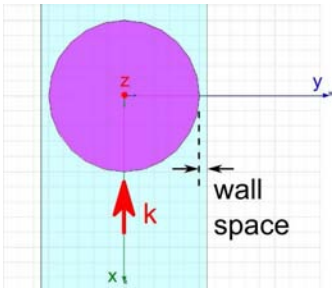

(a) Periodic model containing only one cylinder

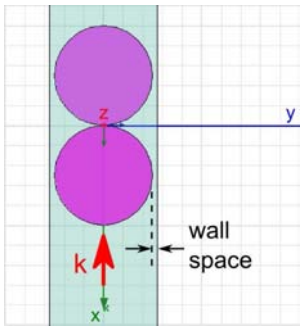

(b) Periodic model containing two cylinders placed back-to-back

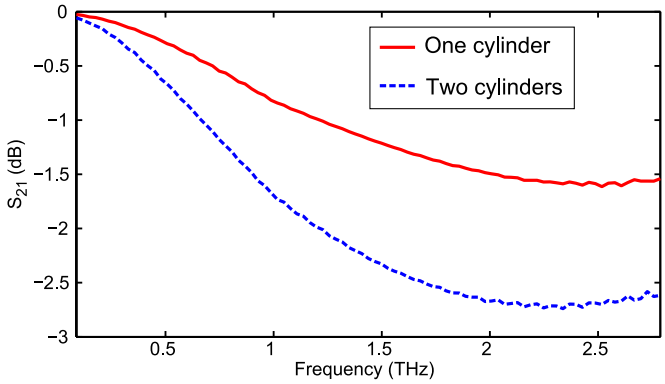

(c) S_{21} plots from the two periodic models shown above

Figure 8.13: S_{21} plots for single-layered and double-layered arrays. (a) Simplest periodic model containing only one cylinder. (b) Periodic model containing two layers of cylinders. (c) The extra cylinder layer appears to approximately double the S_{21} values across all THz frequencies.

second model shown in Fig. 8.14(b) is more similar to Fig. 8.8 except that there is no offset between the two cylinders.

The reason for using Fig. 8.14(a) is because it is structurally simple. It contains only one cylinder, reducing any errors that may arise from the presence of multiple cylinders in the problem space. Figure 8.14(b) is included because it is equivalent to Fig. 8.14(a), therefore their S-parameters should be similar with only small differences that arise from meshing. If the presence of multiple cylinders causes any significant problem, then the two sets of S-parameters will differ noticeably.

In Fig. 8.14(c), the S_{21} plots of the single- and double-cylinder (no offset) periodic models nearly overlap when plotted together, with only a slight displacement due to meshing differences between the two models. The similarities between the two S_{21} plots

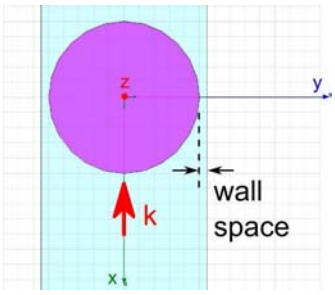

(a) Periodic model containing only one cylinder

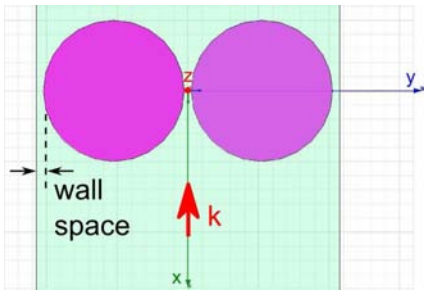

(b) Periodic model containing two cylinders, but with no offset between cylinders

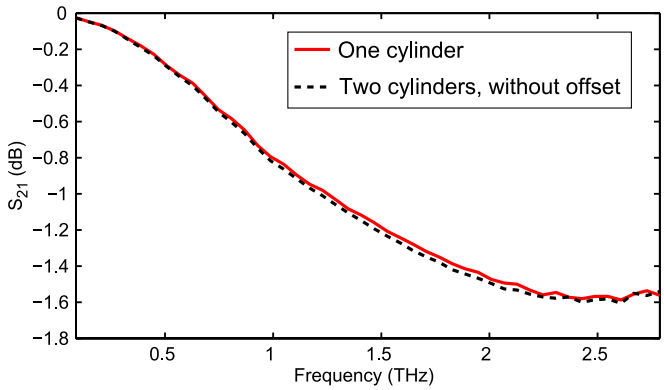

(c) S_{21} plots from the two periodic models shown above

Figure 8.14: Comparison of similar periodic models. (a) Reproduced from Fig. 8.13(a). Simplest periodic model containing only one cylinder. (b) Equivalent model to Fig. 8.14(a), but with two cylinders and no offset between cylinders. (c) Comparison of the S_{21} plots from the single cylinder in Fig. 8.14(a), and the double cylinders in Fig. 8.14(b). The plots from the single- and double-cylinder models mostly overlap with only a slight displacement due to meshing differences between the models. The overlap shows consistency in the HFSS simulations, with no unexpected artefacts arising from the presence of multiple cylinders in the problem space.

indicate that the models are generally equivalent, and that artefacts have not been introduced from the presence of multiple cylinders in the problem space. It can therefore be concluded with confidence that the numerical results generated by HFSS thus far are not corrupted by meshing inconsistencies.

One other issue pertaining to checking for inconsistencies in HFSS is the effectiveness of the periodic boundaries on simulating periodicity. In the next Subsection, the influence of the periodic boundaries on the simulation is demonstrated by comparing the periodic models with the non-periodic ones, i.e. without periodic boundaries. The non-periodic models should, in theory, behave according to Mie scattering described

in Section 8.3. In order to make the comparison, electric field overlay patterns are used instead of the S-parameters because the patterns allow ease of comparison with the radiation patterns presented earlier in Fig. 8.6.

8.9.1 Field Overlay Patterns

Figure 8.15 presents the scattered and total field overlay patterns of the periodic HFSS model (with offset between cylinders), in both the parallel and perpendicular orientations. In order to appreciate the scattering behaviour of the periodic arrays, similar results from parallel and perpendicular non-periodic models are provided in Figs. 8.16 and 8.17 respectively for comparison.

Non-Periodic HFSS Model

The parallel non-periodic model is excited by an incident THz beam with parallel polarisation as shown in Fig. 8.16(a), whereas the perpendicular non-periodic model is excited by an incident THz beam which is perpendicular to the long axis of the cylinders as shown in Fig. 8.17(a).

Each non-periodic model consists of two cylinders in an airbox but without periodic master/slave boundaries—airbox side walls at distance $\lambda_{max}/2$ away from the cylinders are used instead. Like the periodic model, all side walls are assigned PML boundaries, and symmetrical boundaries are applied to the top and bottom faces of the airbox to create infinitely long cylinders along the z-axis. As explained in Section 8.7.1, a second smaller airbox that does not touch the PML boundaries is used for far-field calculations.

Comparison of Field Overlay Patterns

Comparing the scattered field overlay patterns at 1 THz from the two parallel orientations in Figs. 8.15(a) and 8.16(b), the scattered E field of the non-periodic model is clearly radial, agreeing with the Mie analytical solution presented in Fig. 8.6(b) which is consistent with the behaviour of an isotropic point source in space. Furthermore, the magnitude of the scattered E field differs considerably between the periodic and non-periodic models: the scattered E field of the non-periodic model is approximately one order of magnitude lower than the periodic model.

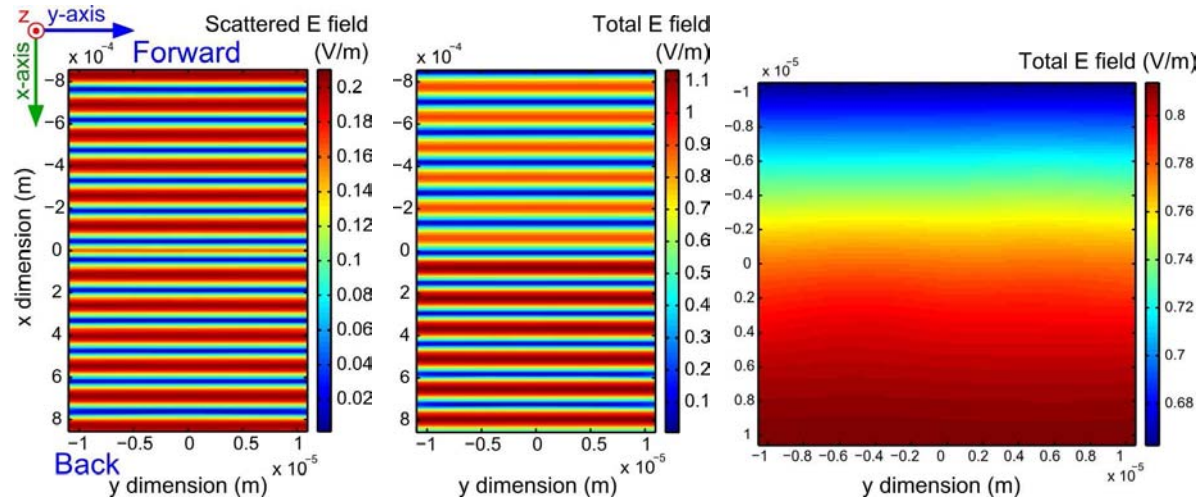

(a) Scattered E field for the parallel orientation

(b) Total E field for the parallel orientation

(c) Total E field (parallel orientation) in the vicinity of the cylinders

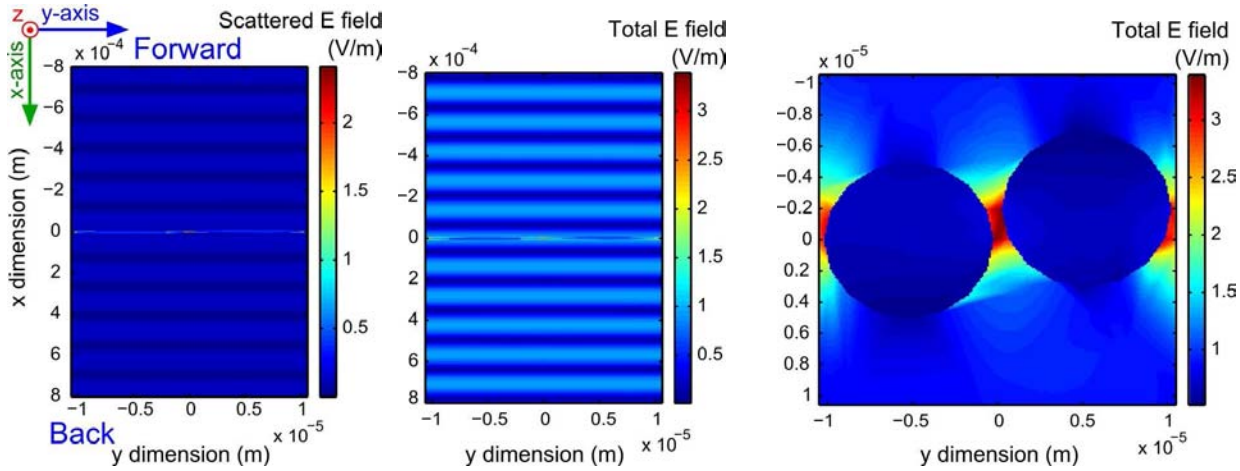

(d) Scattered E field for the perpendicular orientation

(e) Total E field for the perpendicular orientation

(f) Total E field (perpendicular orientation) in the vicinity of the cylinders

Figure 8.15: Field overlay and directivity patterns. (a–b) Field overlay patterns of the total and scattered E field at 1 THz for the parallel orientation, excited by an incident E field of 1 V/m. The array is located along $x = 0$. There is a distinct reduction in the total E field after transmission through the array, evidence of the filtering effect when the array is aligned parallel to the polarisation of the incident E field. (c) Zoomed view of the total E field in the vicinity of the cylinders shows that the cylinders act like a porous barrier to the incident E field, reducing the field strength of the transmitted field. (d–e) Field overlay patterns of the same fields at the same settings for the perpendicular orientation. There is no visible reduction in the total E field after transmission through the array. However, the E field is particularly strong in the vicinity of the cylinders. (f) Zoomed view in the vicinity of the cylinders show the strong E field between the cylinders.

The extent of scattering becomes more apparent when the total E field is observed in Figs. 8.15(b) and 8.16(c). There is no observable change in the total E field before and after transmission through the non-periodic model in Fig. 8.16(c). Conversely, there is a distinct reduction in the E field for the periodic model in Fig. 8.15(b), suggesting less transmission of the E field due to strong scattering. This outcome is consistent with the notion that the parallel array filters out some of the the incident THz radiation in the forward direction. Finally, the maximum total E field in the backscatter direction of Fig. 8.15(b) is 1.1 V/m, which is larger than the incident field E_{inc} = 1 V/m. The reason for the stronger E field in the backscatter direction is either constructive interference between the backscattered E field and the incident field, or the formation of standing waves in the backscatter direction due to reflections at the boundaries of the airbox.

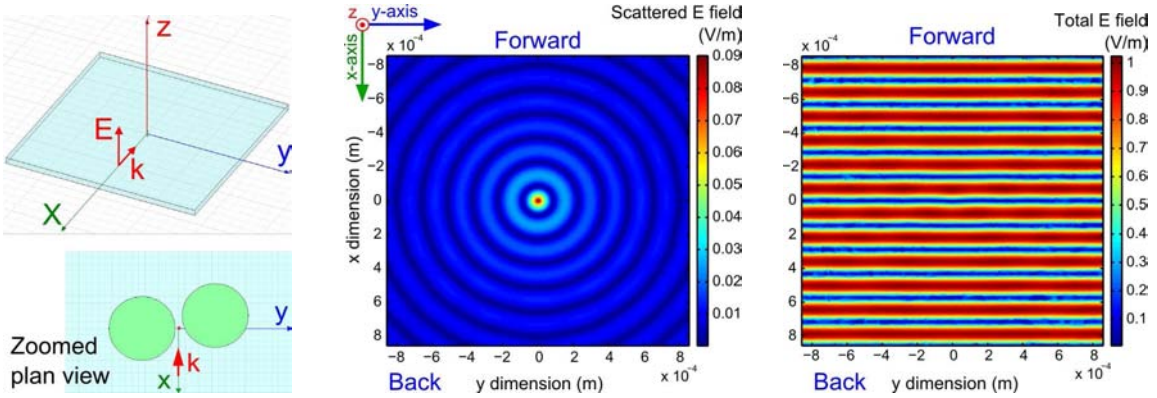

(a) Non-periodic parallel model

(b) Scattered E field from the non-periodic parallel model

(c) Total E field transmitting through the non-periodic parallel model

Figure 8.16: Non-periodic parallel HFSS model. (a) HFSS model containing only two cylinders without periodicity, orientated parallel to the polarisation of the incident THz beam. Zoomed plan view shows the cylinders are similar to those in Fig. 8.9(c) but without the periodic master/slave boundaries to the left and right of the cylinders. (b–c) Field overlay patterns of the total and scattered E field at 1 THz, excited by an incident E field of 1 V/m. This model has a radial scattered field pattern similar to the radiation pattern derived from analytical solutions in Fig. 8.6(b). Unlike the periodic model in Fig. 8.15(a), the total field after transmitting through the cylinders appears unaltered by the small magnitude of scattered field.

Comparison of the scattered E field of the perpendicular periodic and non-periodic models in Figs. 8.15(d) and 8.17(c) suggests the non-periodic model behaves like an

oscillating electric dipole in space. However, the extent of scattering is small compared with the strength of the incident E field. A comparison of the total E fields in Figs. 8.15(e) and 8.17(c) do not reveal significant differences apart from the strong E field for the periodic model in the vicinity of the cylinders as shown in Figs. 8.15(e) and 8.15(f). The E field is not hindered by the cylinders and is transmitted with no significant decrease in signal strength.

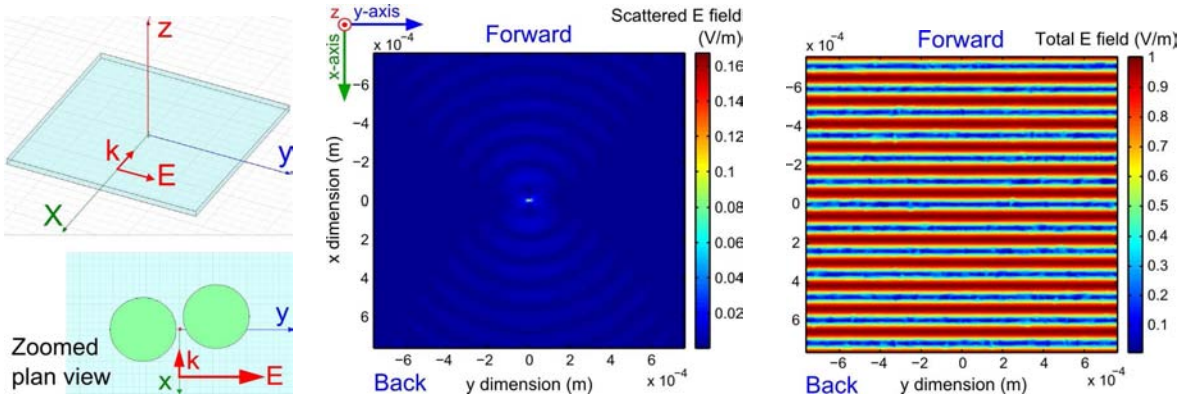

(a) Non-periodic perpendicular model

(b) Scattered E field from the non-periodic perpendicular model

(c) Total E field from the non-periodic perpendicular model

Figure 8.17: Non-periodic perpendicular HFSS model. (a) Similar HFSS model to that in Fig. 8.16(a), but orientated perpendicular to the incident THz beam. (b–c) Field overlay patterns of the total and scattered E field at 1 THz. The scattered field pattern differs from the parallel case, but the magnitude of the scattered field is similarly small. Consequently, the total field after transmitting through the cylinders also appears unaltered. The scattered field pattern has the distinct shape of an oscillating electric dipole.

8.10 Precautions Needed When Using HFSS

Several precautions need to be taken when using HFSS, particularly when modelling a 2D problem with symmetry in one dimension such as the one presented in this study. Being a 3D solver, HFSS is most appropriate for analysing 3D problems, with built-in capabilities for plotting 3D polar plots. However, when HFSS is used to model a 2D problem, plots that involve the 3D space need to be used with caution because of the near-field to far-field transformations utilised by HFSS to solve far-field problems. In a 2D problem with symmetrical surfaces, it is not known how HFSS performs far-field

to near-field transformations on the symmetrical surfaces. This issue is lacking from HFSS documentation as it is not common practice to utilise HFSS for 2D modelling.

Another precaution needed when using HFSS is *a priori* knowledge of settings and limitations of boundary condition needs to be researched. The HFSS software does not report errors if incorrect settings are used; simulations can run to completion with incorrect settings with no indication of error. For example, the second airbox used for far-field calculations as described in Section 8.7.1 was initially not included in this study; the airbox which touched the PML surfaces was used instead. The resultant S_{21} plot for the parallel case with strand space set at 10 μm had a profile that matched the THz transmission magnitude of sample 1 in Fig. 8.3(a), including the upwards-turning curve beyond 2.2 THz. However, the curve continued its upwards trend such that $S_{21} > 1$ beyond 2.5 THz, which is not possible as this would imply amplification of the THz signal. As there are no active sources in the HFSS model, this result was suspicious; it was subsequently found to be incorrect after introduction of a more suitable second airbox[73] for far-field calculations.

Two alternative electromagnetic field simulators that may be more suited for the 2D problem presented in this study are COMSOL (by COMSOL AB) and the Multiple Multipole Program[74] (Hafner 1995, Hafner 1999). The latter simulator is most suited for 2D problems, particularly periodic surfaces. Unfortunately due to cost, neither simulator was available for this study.

8.11 Conclusion

In this study, we have presented novel THz-TDS measurements of subwavelength fibreglass arrays, and have utilised a full-wave electromagnetic field simulator to model our measurements. We have also included a comparison of the performance of analytical solutions for scattering, and modelling arrays. The plotting capabilities of the full-wave electromagnetic field simulator has permitted us to investigate the electric field distribution caused by the presence of the test sample, providing an extra dimension of information that would otherwise be lacking in transmission-mode experiments.

[73] The use a second airbox that does not touch the PML surface was only discovered in this study through HFSS technical discussion websites, such as <www.edaboard.com>.

[74] An evaluation version of the Multiple Multipole Program (MMP) is available at: <http://alphard.ethz.ch/Hafner/mmp/mmp.htm>

8.11.1 Future Work

One potential use of this study is to extend the investigation to include spheres. A 3D model containing a periodic array of spheres in one dimension would simulate powders and other spherical scatterers commonly encountered in THz experiments. Another potential extension of this study is to explore THz scattering from surfaces, such as walls and skin. The influence of surface roughness in the THz regime would be interesting in the realm of THz communications and medically-inspired THz applications. The HFSS , COMSOL and MMP simulators could be used in parallel in order to compare complementary results.

8.12 Chapter Summary

This study has explored the use of analytical (exact) solutions and a full-wave electromagnetic field simulator to model novel THz measurements of near-periodic fibreglass arrays. The THz measurements show that the orientation of fibrillar (cylindrical) structures is an important consideration, resulting in significantly different measured THz transmission signals.

The HFSS simulator allows in-depth investigation of the THz transmission profiles of such arrays to be performed with relative ease. Subtle changes to the structure of the arrays can be modelled to explain features in the THz measurements, facilitating the understanding of how periodic cylindrical structures behave in the THz frequency regime. Although several problems were encountered in modelling a 2D structure in a 3D simulator, the use of symmetrical and periodic boundaries can aid in overcoming these hurdles. However, the reports generated by HFSS need to be used with caution and should be verified with theory, such as antenna theory, if possible. Other commercial simulators, such as COMSOL and MMP may be more suited for modelling 2D problems such as those presented in this study.

Commercial full-wave simulators may be attractive tools for studying electromagnetic phenomena, however their licencing cost can make them prohibitive. The steep learning curve needed to understand the wide range of functions of these powerful and versatile simulators, and the need for external verification with theory, can make these simulators overwhelming for new users. At times, analytical and numerical models

exist that can perform as well, if not better, than full-wave simulator. Although analytical (exact) solutions did not perform as well as the full-wave electromagnetic simulator in this Chapter, in many instances they can. The next Chapter presents a study that utilises exact solutions to verify THz transmission and reflection measurements from a stratified environment.

Chapter 9

Modelling Terahertz Propagation in Stratified Media

IN order to advance the use of THz spectroscopy and imaging for medical diagnosis, more studies are needed to understand the interaction of THz radiation with biological matter. In the previous Chapter, a full-wave electromagnetic field simulator was used to study THz interaction with a periodic array. Simplification of the problem space is needed given the limitations of computer hardware and computation time. For biotissue that contains stratified layers (fat, muscle, *etc*.), modelling this complex test environment on a full-wave electromagnetic field simulator can pose even more of a challenge when computing resources are limited.

Analytical (exact) mathematical models have been developed to study electromagnetic propagation and scattering from simplified biotissue environments, assuming homogeneity within layers, and often reducing the problem space from 3D to 1D. This Chapter presents a study that utilises exact solutions to verify THz transmission and reflection measurements from stratified media.

9.1 Introduction

In Chapter 6, novel experiments involving excised snap-frozen brain samples were presented. The early results reported in Section 6.5 are encouraging, although improvements to experimental technique and histological co-registration are needed. With regards to the quality of THz measurements, snap-frozen excised biotissue has its merits over freshly excised biotissue . However, excision of any type of biotissue is invasive; for the case of brain tissue, the samples are usually[75] only available *postmortem*.

In vivo examination of biotissue is obviously less invasive, but from the review of medical and pharmaceutical THz applications presented in Section 4.5, *in vivo* examination is often not possible due to high THz attenuation by liquid water. However, two types of biotissue—skin, and tissue located underneath skin—appear to be promising for *in vivo* THz inspection.

9.1.1 Motivation

One motivation of this Thesis, as stated in Section 1.5, is to contribute towards the pool of new medical THz applications. A question that arises from the investigation in Chapter 6 is whether THz spectroscopy or imaging can be used for *in vivo* examination of layers of scalp, or perhaps the outermost layer of the brain where protein plaques associated with Alzheimer's disease are located. Layers of the scalp may be sufficiently close to the surface of the skin for THz sensing. Non-invasive screening of the head has widespread application in medicine. This Chapter aims to ascertain if THz spectroscopy is feasible for this task.

This Chapter also aims to address the other motivation of this Thesis: to further the understanding of THz interaction with biotissue. The penetration and propagation of THz radiation through the layers of the head need to be understood in order to ascertain if *in vivo* THz diagnosis can be performed. A mathematical analytical (exact) model is used to achieve this task.

[75] Brain biopsies can be performed on living patients, but only very small quantities of biotissue is removed for pathological examination (Hall 1998).

9.1.2 Objective Summary

The study presented in this Chapter utilises a simple yet effective analytical model in Section 9.3 to elucidate THz propagation through biotissue located several millimeters beneath the skin. Since no novel THz measurements are conducted in this study, the accuracy of the analytical models are validated in Section 9.5.1 by comparing the empirical results with measurement performed by other authors.

The analytical model utilised in this study was developed for the microwave frequency range, but can be applied to other frequencies. Many other models exist, particularly in the microwave frequency range, for studying different aspects of biotissue. A brief overview of other models is presented in Section 9.2.

Optical properties (or *dielectric properties*) of biotissue at or around the frequencies under investigation are required in the model used in this study. Optical properties of biotissue in the THz frequency range is sparse. The converse is true for the IR and microwave frequency ranges. Since THz lies between the IR and microwave ranges, the IR and microwave optical properties are particularly relevant to THz research. In Section 9.4, relevant optical properties from the IR and microwave frequency ranges are introduced and extrapolated into the THz range.

9.2 Review of Modelling Methods

In this Section, an overview of existing research into electromagnetic wave propagation in stratified media is presented. Research at the microwave frequencies is most prolific, possibly because of the long propagation range and penetration depth of microwave radiation. For example, models have been developed to study the propagation of microwave radiation in motion sensors, and for microwave land mine detection (Trang 1996). The heating effect of microwave radiation has also spurred studies into biotissue heating from exposure to microwave radiation, particularly heating of the head (Abdalla and Teoh 2005). Optical properties of different layers of the head at microwave frequencies presented by Abdalla and Teoh (2005) are a good source of information for THz studies of the head. This will be elaborated on in Sections 9.3 and 9.4.

There is a wealth of information available for modelling microwave propagation in the body. Ellipsoidal models and the Methods of Moments (MoM) technique were

traditionally used to model the body as a whole, but more recent analytical methods such as the Finite Element Method (FEM) and Finite Difference Time Domain (FDTD) have allowed voxelisation of the body (Dawson *et al.* 2001). In the THz frequency regime, a FDTD model is used by Pickwell *et al.* (2004a) for modelling one and two layers of skin (Pickwell *et al.* 2004a, Pickwell *et al.* 2004b). To model THz propagation in wire waveguides, FEM modelling has been used (Deibel and Mittleman 2006). Other model types, such as the Monte Carlo and thin film models, have been used to simulate THz propagation through a tissue simulating phantom (Walker *et al.* 2003, Walker *et al.* 2004).

For completeness, it should be noted that research into the propagation of visible light ($\nu \approx 417$–750 THz, $\lambda \approx 720$–400 nm) in skin is another active area of research. Examples of investigations are light scattering by biotissue (Maximov *et al.* 2001), modelling rough interfaces using skin tissue phantoms (Lu *et al.* 2000), and modelling the dielectric properties of normal and irradiated skin (Tamura *et al.* 1994). Although optical properties measured at the visible light frequencies are not easily extrapolated into the THz frequency range, many of the modelling techniques are applicable for the THz range.

The next Section presents one such mathematical model that is often used at radio frequencies. This model, based on the impedance model from transmission line theory (Wait 1996), is used in this Thesis to simulate THz propagation into the stratified layers of the human head.

9.3 Transmission Line Model for THz Propagation

Figure 9.1(a) shows the propagation of electromagnetic radiation into a stratified medium. Both the electric and magnetic field vectors (drawn with thick arrows) are in the plane of propagation. The z-axis extends down the depth of the layers, while the x-axis is along the length of the layers. The y-axis is perpendicular to the drawing plane. For an electromagnetic wave with electric field vector in the plane of incidence (xz plane), the differential form of Maxwell's equation can be written as

$$\nabla^2 H(x,z,t) = \frac{\partial^2 H(x,z,t)}{\partial x^2} + \frac{\partial^2 H(x,z,t)}{\partial z^2} = \mu\sigma\frac{\partial H(x,z,t)}{\partial t} + \mu\epsilon\frac{\partial^2 H(x,z,t)}{\partial t^2}. \quad (9.1)$$

NOTE:
This figure is included on page 263
of the print copy of the thesis held in
the University of Adelaide Library.

Air	
Skin	100 μm
Adipose Tissue	1000 μm
Cortical bone	10,000 μm
Dura Mater	250 μm
CSF	200 μm
Gray Matter	2000 μm
White Matter	∞

(a) Stratified medium with M homogeneous layers (b) Approximate head tissue thickness

Figure 9.1: Schematics of stratified medium and tissue layers in the head. (a) The dotted line indicates the incident and reflected path. The thick arrows signify the electric field and magnetic field vectors. Both vectors are in the plane of propagation. After Wait (1996). (b) Approximate thickness of tissue layers in the head. After Abdalla and Teoh (2005) and after Nolte (2002).

In the frequency domain, where $\omega = 2\pi\nu$ and ν is the frequency in units of Hertz, Equation (9.1) becomes:

$$\begin{aligned} \nabla^2 H(x,z,\omega) &= i\omega\mu\sigma H(x,z,\omega) - \omega^2\mu\epsilon H(x,z,\omega) \\ \left[\nabla^2 - (i\omega\mu\sigma - \omega^2\mu\epsilon)\right] H(x,z,\omega) &= 0 \\ \left(\nabla^2 - \gamma^2\right) H(x,z,\omega) &= 0\,, \qquad (9.2) \\ \left[\frac{\partial^2 H(x,z,\omega)}{\partial x^2} + \frac{\partial^2 H(x,z,\omega)}{\partial z^2} - \gamma^2 H(x,z,\omega)\right] &= 0\,. \qquad (9.3) \end{aligned}$$

Equation (9.3) is the Helmholtz equation, and the square of the propagation constant γ is equal to:

$$\gamma^2 = (i\omega\mu\sigma - \omega^2\mu\epsilon) = -\hat{k}^2 = -\{k\,\hat{n}\}^2 = -\{k(n - i\kappa)\}^2\,, \qquad (9.4)$$

and $\hat{k}$ is the complex wavenumber, $k = 2\pi/\lambda$ is the wavenumber, $\hat{n}$ is the complex refractive index with real and imaginary components n and κ respectively. For a multilayered surface, the square of the propagation constant of the mth layer is equal to:

$$\gamma_m^2 = i\omega\mu_m\sigma - \omega^2\mu_m\epsilon_m\,. \qquad (9.5)$$

The general solution of Equation (9.3) for the mth layer, which is derived in Appendix G, is expressed here as:

$$H_m(x,z,\omega) = a_m(\omega)e^{-z\sqrt{\gamma_m^2+\beta^2}-i\beta x} + b_m(\omega)e^{z\sqrt{\gamma_m^2+\beta^2}-i\beta x}$$

$$= \; a_m(\omega)e^{-u_m z - i\beta x} + b_m(\omega)e^{u_m z - i\beta x}\,, \tag{9.6}$$

where $u_m^2 = \beta^2 + \gamma_m^2$ and $a_m(\omega), b_m(\omega)$ are constants. The dummy variable β can take any value that ensures $\Re(u) > 0$. At the zeroth layer, the general solution of Equation (9.3) is expressed as:

$$H_0(x,z,\omega) \; = \; a_0(\omega)e^{-z\sqrt{\gamma_0^2+\beta^2}-i\beta x} + b_0(\omega)e^{z\sqrt{\gamma_0^2+\beta^2}-i\beta x}\,. \tag{9.7}$$

The equation of a three dimensional stationary plane wave with magnitude $A(\omega)$ is defined by Hecht (2002) as:

$$H(x,z,\omega) \; = \; A(\omega)e^{-ik(\sin\theta)x - ik(\cos\theta)z}\,. \tag{9.8}$$

For the plane wave shown in Fig. 9.1(a) propagating in the zeroth layer where $\hat{n} \approx 1 - i0$, Equation (9.4) becomes:

$$\gamma^2 \; = \; -\left\{k\,\hat{n}\right\}^2 \; = \; -k^2 \; \Rightarrow \; \gamma \; = \; ik\,. \tag{9.9}$$

Substituting Equation (9.9) into Equation (9.8), and letting $\gamma_m = \gamma_0$ at the zeroth layer, gives:

$$H_0(x,z,\omega) \; = \; A(\omega)e^{-\gamma_0(\sin\theta)x - \gamma_0(\cos\theta)z}\,. \tag{9.10}$$

Comparing Equations (9.7) and (9.10), it can be observed that at the zeroth layer:

$$\begin{aligned} a_0(\omega)e^{-z\sqrt{\gamma_0^2+\beta^2}-i\beta x} &= A(\omega)e^{-\gamma_0(\sin\theta)x-\gamma_0(\cos\theta)z} \\ \text{where } a_0(\omega) &= A(\omega) \\ i\beta &= \gamma_0\,(\sin\theta) \\ \sqrt{\gamma_0^2+\beta^2} &= \gamma_0\,(\cos\theta)\,. \end{aligned} \tag{9.11}$$

Equation (9.11) describes the transmitted wave from the zeroth layer into the $m = 1$ layer. Since the direction of z in $b_0(\omega)e^{z\sqrt{\gamma_0^2+\beta^2}-i\beta x}$ is opposite to that in Equation (9.11), $b_0(\omega)e^{z\sqrt{\gamma_0^2+\beta^2}-i\beta x}$ therefore describes the reflected wave at the interface between the zeroth and $m = 1$ layer.

Referring to Fig. 9.1(a), let the tangential fields be continuous at the boundaries of interfaces $z = 0, z = z_1, \ldots, z = z_{m-1}$. In terms of the magnetic field H and the electric field E, the boundary conditions mean that:

$$H_{m\text{-}1}(x,z,\omega) \; = \; H_m(x,z,\omega)\,, \tag{9.12}$$

or in terms of the electric field:

$$\begin{aligned} E_{m\text{-}1}(y,z,\omega) &= E_m(y,z,\omega) \\ \frac{1}{\sigma_{m\text{-}1}+i\omega\epsilon_{m\text{-}1}}\left(\frac{\partial H_{m\text{-}1}}{\partial z_{m\text{-}1}}\right) &= \frac{1}{\sigma_m+i\omega\epsilon_m}\left(\frac{\partial H_m}{\partial z_{m\text{-}1}}\right), \\ \text{where } E_m(y,z,\omega) &= -\frac{1}{(\sigma_m+i\omega\epsilon_m)}\left(\frac{\partial H_m(x,z,\omega)}{\partial z}\right) \end{aligned} \tag{9.13}$$

and $m = 0, 1, 2, \ldots, M-2, M-1$.

Let the lowest layer (Mth layer) have infinite thickness ($h_M = \infty$). By setting the condition that outgoing waves are only allowed in this lowest layer, then all reflected waves $b_m(\omega) = 0$, except $b_0(\omega) \neq 0$. Solving the general solution Equation (9.6) with the boundary conditions given in Equations (9.12) and (9.13), the resulting particular solution is equal to:

$$\begin{aligned} \frac{\text{Amplitude of reflected wave}}{\text{Amplitude of incident wave}} = \frac{b_0(\omega)}{a_0(\omega)} &= \frac{K_0 - Z_1}{K_0 + Z_1} \\ \text{where} \quad Z_1 &= K_1 \frac{Z_2 + K_1 \tanh(u_1 h_1)}{K_1 + Z_2 \tanh(u_1 h_1)} \\ Z_2 &= K_2 \frac{Z_3 + K_2 \tanh(u_2 h_2)}{K_2 + Z_3 \tanh(u_2 h_2)} \\ &\vdots \\ Z_m &= K_m \frac{Z_{m+1} + K_m \tanh(u_m h_m)}{K_m + Z_{m+1} \tanh(u_m h_m)} \\ &\vdots \\ Z_{M\text{-}1} &= K_{M\text{-}1} \frac{K_M + K_{M\text{-}1} \tanh(u_{M\text{-}1} h_{M\text{-}1})}{K_{M\text{-}1} + K_M \tanh(u_{M\text{-}1} h_{M\text{-}1})}, \end{aligned} \tag{9.14}$$

and $Z_M = K_M$ because the lowest layer (Mth layer) is assumed to have infinite height. In addition,

$$K_m = \frac{u_m}{\sigma_m + i\omega\epsilon_m}, \quad \text{and} \quad u_m = \sqrt{\beta^2 + \gamma_m^2} = \sqrt{\beta^2 + i\omega_m\mu_m\sigma - \omega^2\mu_m\epsilon_m}\,.$$

The optical properties σ, ϵ and μ in Equation (9.14) are frequency dependent, thus it is necessary to use appropriate terahertz parameters. However, there is a dearth of THz optical properties in existing literature with regards to human tissue. In Berry *et al.* (2003a) and Fitzgerald *et al.* (2003), refractive indices and attenuation coefficients in the 0.5–1.5 THz range are reported for ten types of excised biotissue, including skin, adipose tissue and cortical bone. This information is very useful but insufficient to model the layers of the head as shown in Fig. 9.1(b). Without access to excised biotissue, extrapolation of microwave and IR data into the THz range is one possible option. The

next Section highlights existing microwave and IR optical properties, and verification methods employed to ensure extrapolated data is accurate.

9.4 Optical (Dielectric) Properties of Biotissue

In Sections 4.3–4.5, a comprehensive review of medical applications in the IR, microwave and THz frequency ranges was presented. The breadth of IR and microwave medical applications is extensive compared to those in the THz frequency range. This is also true with regards to the availability of biotissue optical properties. This Section presents IR and microwave studies salient to this investigation. Studies conducted in the submillimeter frequency range are also briefly mentioned where applicable.

9.4.1 Infrared and Submillimeter Regions

Many biologically inspired IR studies are related to skin investigations, particularly the scattering effects of IR radiation in the top layers of skin (Troy and Thennadil 2001, Viator *et al.* 2003). However, IR studies in the far-infrared range are limited, although some studies have been performed on water. Hasted *et al.* (1987) has reported on the use of dispersive Fourier transform spectroscopy to obtain optical constants of water; this includes data between 5.9–13.7 cm^{-1} ($\approx$ 0.2–0.4 THz). This study has been cited in a microwave paper (Barthel *et al.* 1990) as well as an early THz paper on water (Kindt and Schmuttenmaer 1996). Cross-referencing literature from neighbouring frequency ranges is therefore a *bona fide* way of sourcing information. However, without reliable far-infrared optical properties of biotissue, the submillimeter and microwave regions provides the next best sources of information for the THz range.

Three studies conducted in the submillimeter range are mentioned here as they are most related to biotissue studies. Two of the three studies concern water: the molecular dynamics of water (Bursulaya and Kim 1998), and the permittivities of ice and liquid water (Jiang and Wu 2004). The latter study is primarily for remote sensing applications, hence may be more applicable to long-range THz security applications, such as at checkpoints, rather than ice or liquid water in biotissue.

The third study relating to optical properties of skin in the submillimeter range (ν = 0.07–0.1 THz) is reported by Alabaster (2004). A vector network analyser and two horn antennas were used to empirically measure freshly excised human, bovine and

porcine skin (all fixed in 10% buffered formalin). The results from this experiment yielded complex permittivity values that are quite different at 0.1 THz when compared to extrapolated data reported by Gabriel and Gabriel (1997a) of freshly excised human skin without formalin fixing: $6.87 - 9.39i$ (microwave) compared to $8.5 - 3.2i$ (sub-millimeter). The discrepancy between the two reported values is due to the different preservation methods used in the two studies (formalin-fixed versus fresh). Since this study is interested in fresh biotissue, optical properties recorded by Alabaster (2004) are unsuitable. The microwave region is therefore the remaining source of information for the THz range.

9.4.2 Microwave Region

Microwave data of biological materials is far more plentiful than IR data. An extensive list optical properties of various human and animal tissue types has been compiled by Gabriel *et al.* (Gabriel *et al.* 1996a, Gabriel and Gabriel 1997a) and references made therein. In Gabriel and Gabriel (1997a), data has also been extrapolated to 0.1 THz, hence these studies are most useful for THz investigations.

Optical properties of biotissue can also be found in microwave studies conducted on skin with various skin conditions (Sunaga *et al.* 2002), the dielectric properties of skin (Raicu *et al.* 2000), new phantom materials for modelling biotissue (Robinson *et al.* 1991), and admittance models for open ended coaxial probes (Gabriel *et al.* 1994).

Literature that falls into the microwave category covers a wide range of frequencies, often from below 10^9 Hz up to 10^{11} Hz. However, individual studies usually only cover a small subset of this wide frequency range. It is therefore not uncommon for data interpolation to be performed to link data from two or more studies. One of the most common interpolation techniques is to model the dielectric spectrum of biotissue using the Debye expression:

$$\hat{\epsilon}(\omega) = \hat{\epsilon}(\infty) + \frac{\Delta\hat{\epsilon}}{1 + i\omega\tau} = \hat{\epsilon}(\infty) + \frac{\hat{\epsilon}(0) - \hat{\epsilon}(\infty)}{1 + i\omega\tau}, \tag{9.15}$$

where τ is the relaxation[76] time, $\hat{\epsilon}(0)$ is the static relative complex electric permittivity, and $\hat{\epsilon}(\infty)$ is the high frequency relative complex electric permittivity. The single τ term

[76]The relaxation time of polar liquids is defined in Debye (1929) as "the time required for the moments to revert to a random distribution after the removal of the impressed field." In the context of engineering, τ is akin to the time constant of a resistive-capacitive (RC) circuit.

in the Debye expression is sufficient for modelling polar liquids, but is insufficient for modelling biotissue. Two improved models are the Cole-Cole (Cole and Cole 1941) and the modified Debye model (Hurt 1985). The Cole-Cole includes a distribution parameter η to account for dispersion in the sample; the modified Debye model includes a static ionic conductivity σ_i term, and multiple τ terms. The Cole-Cole and modified Debye models are expressed respectively in Equations (9.16) and (9.17) as:

$$\begin{aligned}\hat{\epsilon}(\omega) &= \hat{\epsilon}(\infty) + \frac{\Delta\hat{\epsilon}}{1+(i\omega\tau)^{1-\eta}} \\ &= \hat{\epsilon}(\infty) + \frac{\hat{\epsilon}(0)-\hat{\epsilon}(\infty)}{1+(i\omega\tau)^{1-\eta}} \qquad (9.16)\end{aligned}$$

$$\begin{aligned}\hat{\epsilon}(\omega) &= \hat{\epsilon}(\infty) + \left(\sum_{g=1}^{G}\frac{\Delta\hat{\epsilon}_g}{1+i\omega\tau_g}\right) + \frac{\sigma_i}{i\omega\epsilon_0} \\ &= \hat{\epsilon}(\infty) + \left(\sum_{g=1}^{G}\frac{\hat{\epsilon}(\omega_g)-\hat{\epsilon}(\omega_{g+1})}{1+i\omega\tau_g}\right) + \frac{\sigma_i}{i\omega\epsilon_0}, \qquad (9.17)\end{aligned}$$

where ϵ_0 is the permittivity *in vacuo*, $\omega_{g=1} = 0$, $\omega_{G+1} = \infty$. In two THz studies, the modified Debye model without the static ionic conductivity term, and $G = 2$ is used to model liquid water (Kindt and Schmuttenmaer 1996, Rønne *et al.* 1999). In another THz study, a model based on the Cole-Cole model is used to predict the absorption coefficients of a mixture of distilled water and propanol-1 (Walker *et al.* 2004); a comparison of the results from this model with measurements show that the model is accurate for only the lower THz range, implying that models based on the Cole-Cole model needs to be used with caution at the higher THz frequency range.

A hybrid of the Cole-Cole and modified Debye models is the multiple Cole-Cole model shown in Equation (9.18):

$$\begin{aligned}\hat{\epsilon}(\omega) &= \hat{\epsilon}(\infty) + \left(\sum_{g=1}^{G}\frac{\Delta\hat{\epsilon}_g}{1+(i\omega\tau_g)^{1-\eta_g}}\right) + \frac{\sigma_i}{i\omega\epsilon_0} \\ &= \hat{\epsilon}(\infty) + \left(\sum_{g=1}^{G}\frac{\hat{\epsilon}(\omega_g)-\hat{\epsilon}(\omega_{g+1})}{1+(i\omega\tau_g)^{1-\eta_g}}\right) + \frac{\sigma_i}{i\omega\epsilon_0}. \qquad (9.18)\end{aligned}$$

A 4-term multiple Cole-Cole model is used to model the dielectric spectrum of many biotissue types in Gabriel *et al.* (1996c). In order to extrapolate data from the microwave to THz frequency range in this Thesis using the MATLAB software, data from Gabriel *et al.* (1996c) is reproduced in MATLAB using the 4-term multiple Cole-Cole model, using values of $\hat{\epsilon}(\infty)$, $\Delta\hat{\epsilon}_g$, τ_g, η_g, and σ_i as given in Gabriel *et al.* (1996b), Gabriel *et al.* (1996c) and Gabriel and Gabriel (1997b). Results from extrapolation using this model are presented in the next Subsection.

9.4.3 Interpolating Optical Properties: Between Microwave and THz

To reproduce the real (ϵ') and imaginary (ϵ'') terms of the complex permittivities $\hat{\epsilon}(\omega)$ of various biotissue reported by Gabriel *et al.* (1996c), the 4-term Cole-Cole model presented in Equation (9.18) is used together with the variables in Table 9.1. However, the optical properties in Fitzgerald *et al.* (2003) are presented in terms of attenuation coefficient $\alpha(\omega)$ (also known as extinction coefficient as defined in Section 7.5.1). Therefore Equations (9.19) and (9.20) are needed to convert between ϵ', ϵ'', and α as follows:

$$\hat{\epsilon}(\omega) = \epsilon'(\omega) - i\epsilon''(\omega) = \hat{n}^2 = [n(\omega) - i\kappa(\omega)]^2 \tag{9.19}$$

$$\alpha(\omega) = \frac{2\omega\kappa(\omega)}{c}. \tag{9.20}$$

To convert between α, ϵ', and conductivity σ values reported by Gabriel *et al.* (1996b), Equation (9.21) is used as follows:

$$\sigma(\omega) = \frac{\omega\kappa(\omega)n(\omega)}{2\pi}, \tag{9.21}$$

where for a dielectric, $\sigma(\omega) = 0$; for metals, $\sigma(\omega) > 0$. The plot of $\epsilon'(\omega)$ and $\sigma(\omega)$ of adipose tissue is shown in Fig. 9.2(a). Figure 9.2(b) presents the optical properties of skin obtained from Gabriel *et al.* (1996c)[77] and Fitzgerald *et al.* (2003); the black dotted line is the 4-term Cole-Cole model converted from $\hat{\epsilon}$ to α.

In order to interpolate between the two data sets, the built-in MATLAB function `interp1` is used on the real and imaginary permittivity values. The reason why the real and imaginary permittivity values are used for interpolation is because the interpolated plots should have profiles that are consistent with dielectric γ-dispersion theory for a medium with high water content (Grant *et al.* 1978). One example outcome of the interpolation process is shown in Figs. 9.3(a) and 9.3(b).

When only microwave data is available (e.g. dura mater, cerebrospinal fluid or CSF, grey matter, and white matter), microwave data from Gabriel and Gabriel (1997a) is extrapolated using the 4-term Cole-Cole model. However, as evident from Fig. 9.2(b) and as consistent with the observation highlighted in Section 9.4.2, the Cole-Cole model is most accurate for low THz frequencies, hence data extrapolated using the 4-term Cole-Cole model are expected to be accurate up to 1 THz only.

[77] In Gabriel *et al.* (1996c), data for *dry* and *wet* skin are available. Since the type of skin in Fitzgerald *et al.* (2003) is not specified, it is assumed to be freshly excised from the body such that at least one surface is dry. Therefore, data from dry skin is utilised from Gabriel *et al.* (1996c).

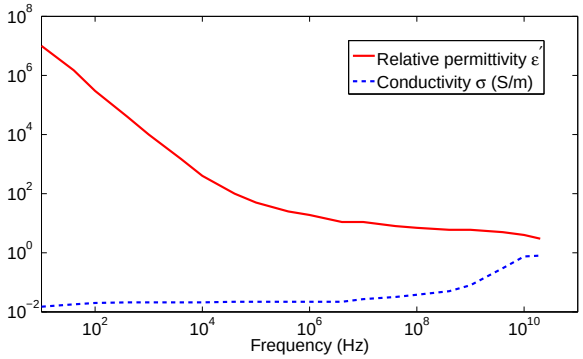

(a) Real permittivity ϵ' and conductivity σ of adipose tissue

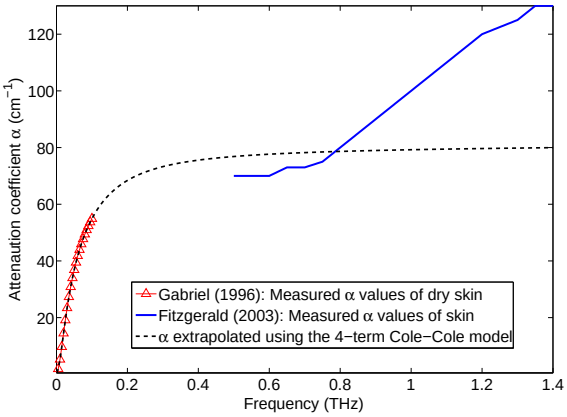

(b) Attenuation coefficients of skin

Figure 9.2: Optical properties of adipose tissue and skin. (a) Reproduction of plots of ϵ' and σ in the microwave frequency range. After Gabriel *et al.* (1996b). (b) The red triangles depict the data reported in Gabriel *et al.* (1996c), converted from ϵ' and σ to α using Equations (9.19–9.21); the thick blue line depicts the data reported in Fitzgerald *et al.* (2003). The black dotted line is the 4-term Cole-Cole model converted from $\hat{\epsilon}$ to α, which appears to be only accurate for low THz frequencies.

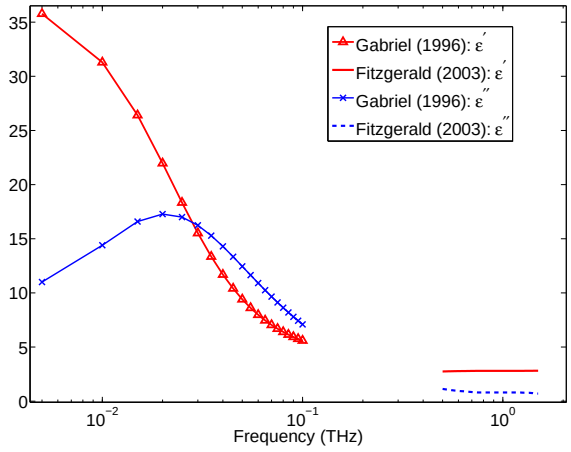

(a) Real and imaginary permittivity terms of skin before interpolation, plotted on a log x-axis

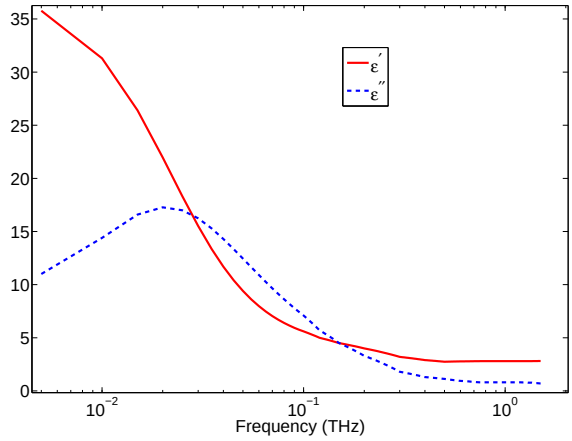

(b) Real and imaginary permittivity terms of skin after interpolation, plotted on a log x-axis

Figure 9.3: Interpolating optical properties of skin. (a) Given that the data reported in Gabriel *et al.* (1996c) covers the microwave range up to $\approx$ 0.1 THz, and the data reported by Fitzgerald *et al.* (2003) covers the lower THz range down to $\approx$ 0.5 THz, the optical properties of skin is unknown in the region between 0.1 and 0.5 THz. (b) To estimate the optical properties of skin between 0.1 and 0.5 THz, interpolation of the real and imaginary permittivity (ϵ' and ϵ'') terms between the microwave and THz frequency ranges is performed using the built-in MATLAB function `interp1`.

Biotissue	$\hat{\epsilon}(\infty)$	$\Delta\hat{\epsilon}_1$	τ_1 (ps)	η_1	$\Delta\hat{\epsilon}_2$	τ_2 (ns)	η_2	$\Delta\hat{\epsilon}_3$	τ_3 (μs)	η_3	$\Delta\hat{\epsilon}_4$	τ_4 (ms)	η_4	σ_i
Dry skin	4.0	32	7.234	0.0	1100	32.481	0.2	0	0	159.155	0.2	0	15.915	0.0002
Bone (cortical)	2.5	10	13.26	0.2	180	79.58	0.2	5×10^3	159.155	0.2	10^5	15.915	0	0.02
Dura mater	4.0	40	7.958	0.15	200	7.958	0.1	10^4	159.155	0.2	10^6	15.915	0	0.5
Cerebrospinal fluid (CSF)	4.0	65	7.958	0.1	40	1.592	0	0	159.155	0	0	0	15.915	2
Grey matter	4.0	45	7.958	0.1	400	15.915	0.15	2×10^5	106.103	0.22	4.5×10^7	5.305	0	0.02
White matter	4.0	32	7.958	0.1	400	7.958	0.1	4×10^4	53.052	0.3	3.5×10^7	7.958	0.02	0.02

Table 9.1: Summary of variables used in the 4-term Cole-Cole model. After Gabriel *et al.* (1996c) and after Gabriel and Gabriel (1997b).

Biotissue	Average relative permittivity ϵ'	Average conductivity σ	Relative magnetic permeability μ
Skin	5.6	0.39	1
Adipose tissue	20	0.9	1
Bone (cortical)	1.5	0.1	1
Dura mater	6	0.48	1
Cerebrospinal fluid (CSF)	9.3	0.77	1
Grey matter	7.75	0.53	1
White matter	6	0.4	1

Table 9.2: Optical properties compiled or interpolated from literature for the 0.1–1 THz frequency range. After Gabriel *et al.* (1996b), Gabriel *et al.* (1996c), Gabriel and Gabriel (1997b), Berry *et al.* (2003a), and Fitzgerald *et al.* (2003).

Table 9.2 presents a summary of the optical properties used to solve Equation (9.18) of various biotissue related to this study. These values, which are either compiled directly from literature or are interpolated between the microwave and THz frequency ranges, tend to be constant over the low THz frequency range (0.1–1 THz), hence only the average values are presented. It is noted here that the THz optical properties of snap-frozen grey matter measured in Chapter 6 are unsuitable for use in this Chapter because optical properties of fresh grey matter are required instead.

9.5 Test and Results

This Section presents the outcome from simulations using the transmission line model in Equation (9.14) to model THz propagation and reflection through layers of the human head as depicted in Fig. 9.1(b). In order to verify if the results generated by the transmission line model are accurate, the results from the topmost layers of the head are compared in Sections 9.5.1 and 9.5.2 with measured results reported in Pickwell *et al.* (2004a) for skin in the forearm. By establishing the validity of the transmission line model, Section 9.6 then examines the plausibility of transmitting THz radiation into the head for diagnostic purposes.

It is acknowledged here that as seen in Chapter 6, biotissue may introduce scattering. However, from the study conducted in Chapter 5 of freshly excised biotissue, THz attenuation due to moisture content is the dominant loss effect in THz spectroscopy of biotissue. Scattering is therefore not considered in this study. Additionally, this study assumes *in vivo* THz spectroscopy of the head, so variations in moisture content over time for excised biotissue (as discussed in Chapter 5) are not applicable.

9.5.1 Test Conditions: Empirical and Simulated

In Pickwell *et al.* (2004a), a Terahertz pulsed imaging (TPI) system operating in reflection mode is used. The incident signal was a short pulse with width of 0.3 ps at half the maximum voltage level, an average power of 100 nW, and a repetition rate of about 80 MHz. Three parts of the forearms of volunteers are scanned with THz radiation, namely the palm, volar, and dorsal forearm. In order to maintain a flat scanning area, the arms of volunteers are pressed against a quartz plate, thus there is an extra propagation time due to the plate's thickness and its refractive index (if thickness of the

plate is 1 mm, $n_{\text{quartz}} = 2.1$, propagation time ≈ 7 ps). Measurements of the volar forearm presented in Fig. 9.4(a) clearly show the mean time response, with first and second reflections. It should be noted that the time axis in this figure is possibly reversed. Figure 9.4(b) provides an overview of skin variation among the volunteers.

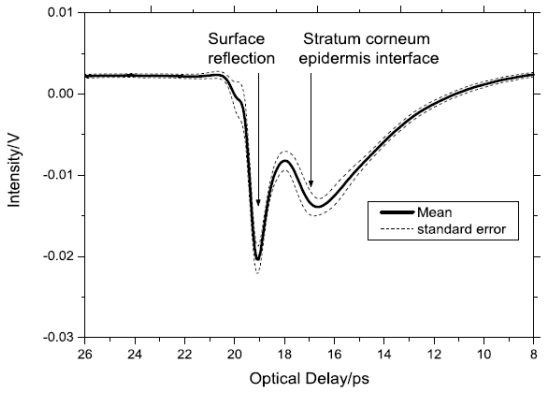

(a) Mean THz time response of the volar forearm

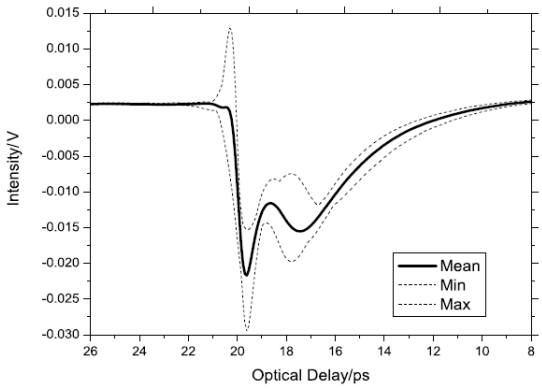

(b) Mean, maximum and minimum time response

Figure 9.4: Reflected signals from the skin of the forearm. These figures are extracted from Pickwell *et al.* (2004a). Note that the time axis may have been possibly inverted accidentally; this inversion does not affect the following qualitative discussion. (a) Empirical data of the mean reflected signal from the skin of the volar forearm buffered by a quartz plate. The mainlobe on the left is due to the surface reflection, while the lobe on the right is from the underlying *stratum corneum*-epidermis interface. (b) The mean, maximum and minimum time response from all volunteers shows some variation in volunteers' skin. The positive peak is reported as the effect of dry[78] skin in some volunteers.

In the study presented in this Thesis, a pulse $\delta(t)$ of width 0.43 ps at half-maximum voltage level is used. By taking the Fourier transform of $\delta(t)$, the incident wave $a_0(\omega)$ as described in Equation (9.14) is obtained. Optical properties used to solve the Z_m and K_m terms in Equation (9.14) are as discussed in Section 9.4.3. The optical property of skin found in literature does not separate skin into its constituent layers (i.e. *stratum corneum*, epidermis, dermis, etc.), hence skin is treated as a single layer. The quartz plate mentioned above is included as one of the layers in Equation (9.14).

The term $b_0(\omega)$ is solved from the transmission line model. Since this is the reflected wave from the topmost stratified layer ($m = 0$), the reflections from skin that are captured in $b_0(\omega)$ should, in theory, be equal to the results from Pickwell *et al.* (2004a).

However, $b_0(\omega)$ is in the frequency domain, while results from Pickwell *et al.* (2004a) are presented in the time domain. The inverse Fourier transform of $b_0(\omega)$ is therefore performed, giving the time-domain reflected wave $B_0(t)$.

9.5.2 Simulation Results using the Transmission Line Model

The reflected wave $B_0(t)$ described in Section 9.5.1 is as shown in Figs. 9.5 and 9.6 for 7 layers of the head depicted in Fig. 9.1(b).

In order to associate the reflections with the respective layer interfaces, Equation (9.22) is used to calculate the propagation time inside each layer, and Equation (9.23) to find the cumulative to and fro travel time, i.e. time taken to traverse from the uppermost tier to the interface of interest, and back upwards again to exit the uppermost tier:

$$\text{Delay due to quartz plate} = t_{\text{quartz}} = \frac{2h_{\text{quartz}}\, n_{\text{quartz}}}{c} \approx 14 \text{ ps}$$

$$\text{Propagation time inside layer } m = t_m = \frac{2h_m\, n_m}{c}, \tag{9.22}$$

$$\text{Cumulative travel time for layer } m = T_m = t_m + t_{m\text{-}1} + \cdots + t_1 + t_{\text{quartz}}, \tag{9.23}$$

where h_m is the thickness of layer m, n_m is the real refractive index of layer m, and c is the speed of light *in vacuo*. The values calculated using Equations (9.22) and (9.23) are tabulated in Table 9.3.

Figure 9.5(b) shows that the simulated result under 20 ps has a similar qualitative shape to the empirical results in Fig. 9.4(a). The decay of the second trough to zero is however less pronounced than the empirical one—this could be due to the exclusion in the simulation of the effect of the water concentration gradient across the thickness of the skin. It is interesting to also note that only one homogeneous layer of skin is utilised in this investigation, whereas skin is separated into *stratum corneum* and epidermis in Pickwell *et al.* (2004a). Despite this difference, the shape of Figs. 9.5(b) and 9.4(a) are similar. This could therefore imply that a single skin layer is sufficient for modelling purposes.

Subsequent reflections are as shown in Figs. 9.6 and 9.7. The third, fourth and fifth reflections shown in Figs. 9.6(a)–9.6(c) are likely to be from latter internal reflections within the adipose tissue-bone interface because they occur at constant 30 ps intervals. For example, the third reflection at $\approx$ 44 ps is 30 ps after the second reflection at 14 ps (see Fig. 9.5(b)), while the fourth reflection at $\approx$ 74 ps is 30 ps after the third. This

30 ps interval is the propagation time t_2 inside the adipose tissue tier. As subsequent reflections are not mentioned in Pickwell *et al.* (2004a), it is assumed that the adipose-bone interface is responsible for this repeated phenomenon.

Evidence of the bone-dura mater-CSF-grey matter interfaces is present in the sixth reflection as shown in Fig. 9.6(d). These reflections, together with the next expected

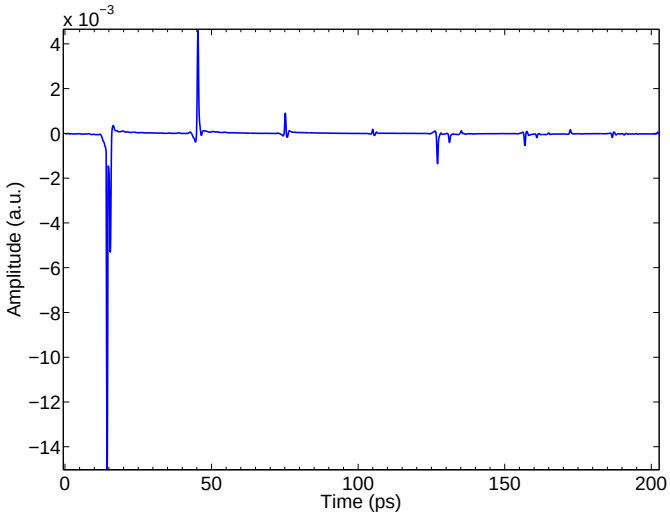

(a) Reflected THz signal $B_0(t)$ from the topmost stratified layer ($m = 0$)

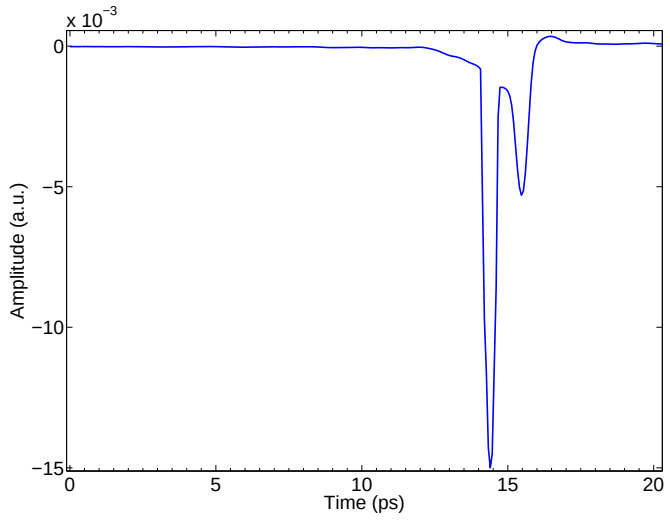

(b) Zoomed view of the first and second reflections

Figure 9.5: Transmission line model simulated reflected signal from 7 tissue layers in the head. (a) Time response of the reflected signal from the surface of the skin. (b) By zooming into the first and second reflections, they can be compared with the results in Fig. 9.4(a). The zoomed view shows that the first trough is due to the air-skin interface, while the second trough is due to the skin-adipose interface.

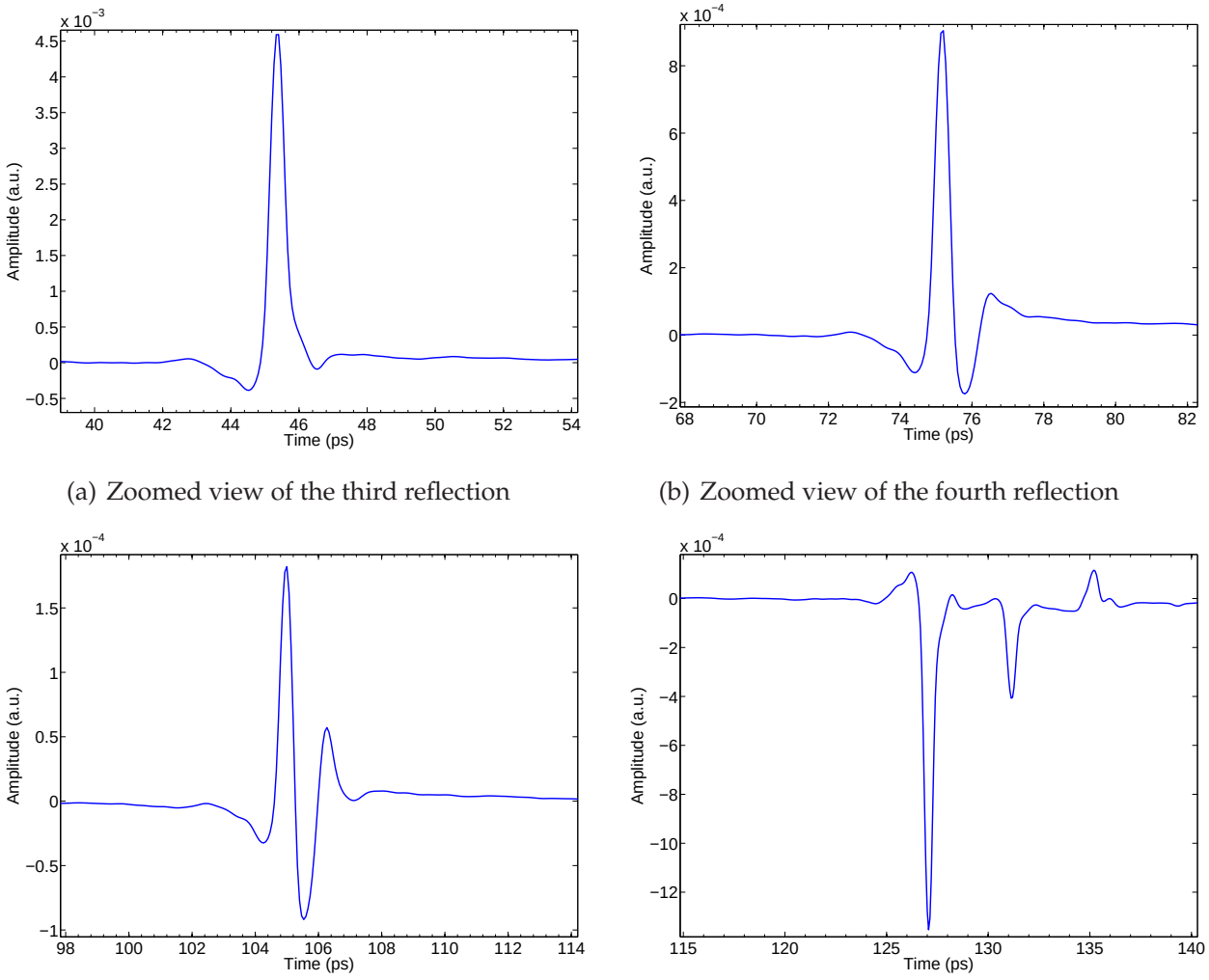

(a) Zoomed view of the third reflection

(b) Zoomed view of the fourth reflection

(c) Zoomed view of the fifth reflection

(d) Zoomed view of the sixth reflection

Figure 9.6: Third to sixth reflections from the transmission line model. (a) The third reflection is likely from the secondary reflections at the adipose-bone interface because it occurs at $t_2 = 30$ ps after the second reflection. (b) The fourth reflection is also likely due to the secondary reflections at the adipose-bone interface because it occurs at $t_2 = 30$ ps after the third reflection. (c) Similarly, the fifth reflection is likely from the secondary reflections at the adipose-bone interface because it occurs at $t_2 = 30$ ps after the fourth reflection. (d) The sixth reflection finally shows evidence of the bone-dura mater-CSF-grey matter interfaces. As shown in Table 9.3, the time occurrence of these reflections are very similar, thus the individual reflections are not easily distinguishable. In addition, the next adipose-bone repetition is expected at 135 ps, thus making it harder to separate the individual reflections.

adipose-tissue reflection, all occur around 133 ps. The individual reflections are therefore not easily distinguishable. Nonetheless, it is encouraging to be able to observe these reflections, which have not been reported to date in literature.

Layer	Layer number m	Approximate propagation time t_m inside layer m (ps)	Approximate cumulative to and fro travel time T_m (ps)
Skin	1	$t_1 = 4$	18
Adipose tissue	2	$t_2 = 30$	48
Bone	3	$t_3 = 82$	130
Dura mater	4	$t_4 = 4$	134
Cerebrospinal fluid (CSF)	5	$t_5 = 4$	138
Grey matter	6	$t_6 = 37$	174
White matter	7	$t_7 = \infty$ (1633)	∞ (1808)

Table 9.3: Propagation and cumulative travel times. Propagation times due to the different layers, including the quartz plate.

The final reflection from the grey matter-white matter interface at ≈ 174 ps is as shown in Fig. 9.7(a). The strong signal at 158 ps may be from the next adipose tissue-bone reflection; this may be investigated in future experimental work beyond this Thesis. Since the white matter is assumed to be of infinite thickness, with infinite propagation time, the reflections after 174 ps as shown in Fig. 9.7(b) are not of interest in this investigation. Future work beyond this Thesis may also investigate why these reflections are more random and more numerous.

As mentioned in Section 9.5.1, the repetition rate of a typical Terahertz Pulsed Imaging (TPI) system is about 80 MHz (period = 12,500 ps). This repetition rate is far longer than t_6 = 174 ps, thus it is possible to capture all the reflections of interest in an actual THz system without interference from the next incident pulse.

9.6 Feasibility of In Vivo Terahertz Diagnosis of the Head

In Fig. 9.5(a), the reflections correspond to calculated return times from known layer thickness. Figure 9.5(b) shows the expected strong reflection from the surface of the skin and the next underlying skin-adipose interface. This plot agrees with reported results in Pickwell *et al.* (2004a).

The third and fourth reflections shown in Fig. 9.6(a) appear to be from the adipose-bone interface. Assuming the average incident THz power level is 1 mW in an amplified laser-based THz system, then the average power of the third and fourth reflections are

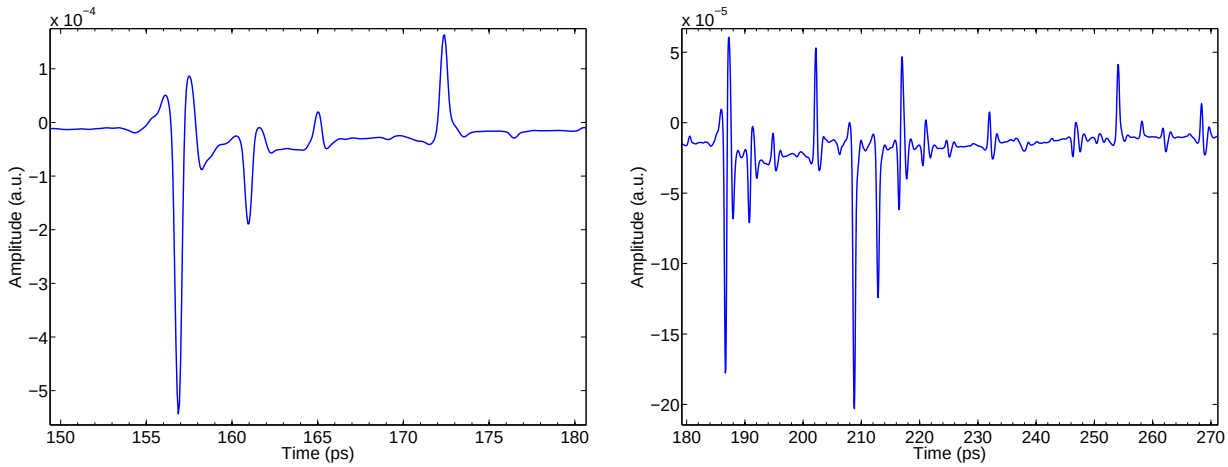

(a) Zoomed view of the seventh reflection

(b) Zoomed view of the reflections beyond t_6

Figure 9.7: Seventh and eighth reflections from the transmission line model. (a) The seventh reflection at 174 ps is possibly from the grey matter-white matter interface. The strong signal at 158 ps may be from the next adipose tissue-bone reflection. (b) Interpreting the subsequent reflection beyond t_6 becomes more challenging as there are increasing numbers of strong peaks. The presence of these peaks could be due to the simulation algorithm. They are less of a concern because the reflections of interest have already passed. Furthermore, these reflections have very low amplitudes, thus are easily masked by noise in an actual THz test system.

approximately 82 μW and 3.3 μW respectively. It is plausible that these two reflections can be detected with present-day technology. However, subsequent reflections shown in Figs. 9.6(b)–9.7(b) are below 1 μW, thus they are unlikely to be detected by present THz detectors without an increase in incident power.

Higher THz power levels up to 1 kW (Xu *et al.* 2006b) may be obtained through the use of synchrotrons and free electron lasers (FELs), but they raise the question of safety. The maximum permissible exposure (MPE) limit derived from animal cornea study with THz has been reported to be 94 W (average power per pulse), although for the human body < 20 W is recommended (Walker *et al.* 2002). Another study investigating ionisation, chemical activation energy, and sample heating of water due to THz heating has shown that pulsed laser-based THz systems are considered safe, but synchrotrons and FELs are not (Kristensen *et al.* 2010). Therefore, unattenuated THz power generated by synchrotrons and FELs is unsafe for direct *in vivo* use on humans.

Although not all the reflections obtained using the transmission line model are practically detectable, the model is still valid for studying the propagation of THz in stratified media, and can assist us in developing better detection techniques for future THz systems. It would appear that that as we approach an input power of 20 W, most of the return pulses as predicted in Fig. 9.5(a) are detectable. This is promising for future THz scanning of the human head—however, a caveat is that extrapolated parameters from the microwave frequency range have been used in this study for dura mater, cerebrospinal fluid (CSF), grey matter, and white matter. Another caveat is that the optical properties of excised biotissue are used, which may differ from living biotissue. Nevertheless, this result provides the motivation for future work to directly measure the THz optical properties of these biotissue types.

9.7 Conclusion

In this study, a novel study of THz propagation through layers of the human head has been presented. The propagation is based on mathematical modelling using the transmission line model. As this model requires optical (dielectric) properties of the different tissue types in the head, several of which are unavailable in the THz frequency range, a review of related work in the microwave, submillimeter, and IR frequency ranges has been included. A comprehensive database of microwave optical properties is available in the public domain; data from this database is used indirectly in this study through extrapolation into the lower THz frequency range (< 1 THz) with the 4-term Cole-Cole model.

The results from this study correlate well with those reported by other authors for the upper layers of skin. Furthermore, the time occurrence of additional reflections generated by the transmission line model appear to agree with calculated propagation times in the various biotissue layers. However, many of these reflections have small signal strengths when compared to the dominant reflections from the upper layers of skin. Therefore, a discussion of the plausibility of detecting these smaller reflections with present THz detectors has been included. Although not all the reflections are practically detectable, the transmission line model is still useful for studying THz propagation in stratified media, and can be expanded for use in other biologically and non-biologically related stratified media, such as soils (THz land mine detection), walls (THz communication), and textiles (THz security).

9.7.1 Future Work

The assumptions made in this study are that all layers are homogeneous and flat. In order to extend this study so that it is applicable to any stratified medium, the inclusion of heterogeneity and structure, such as surface roughness, is required.

To improve modelling accuracy, direct measurements of biotissue THz optical properties are required. Another extension of this study is to investigate other more rigorous propagation models. One possible approach is the pseudospectral time domain (PSTD) algorithm (Liu 1997, Liu 1999b, Liu and Fan 1999, Liu 1999c, Liu 1999a, Lee and Hagness 2004). This algorithm solves Maxwell's equations using the fast Fourier transform (FFT) to represent spatial derivatives. This is unlike conventional Finite Difference Time Domain (FDTD), which utilises finite differences to represent spatial derivatives. The use of the HFSS software described in Chapter 8 to model THz propagation through stratified media is one other possible avenue for enhancing our understanding of THz interaction with complex test environments.

9.8 Chapter Summary

This study has presented one method of modelling THz propagation through stratified media. Since one focus of this Thesis is the investigative use of THz spectroscopy in Alzheimer's disease diagnosis, the human head is the object of this study. Past studies by other authors have shown THz reflections from the surface and underlying layers of skin, thus this study aimed to explore if reflections can be reliably detected from layers of tissue located underneath skin. As expected, strong attenuation of the THz signal occurs given the high water content of biotissue, but this study has revealed some reflections, which correlate well with calculated propagation and reflection times. However, the signal strength of further reflections are small and cannot realistically be detected given present THz input power levels. With future improvements to THz power levels, detection may be possible but safety concerns will need to be addressed.

This study has exposed many gaps in the global THz community's knowledge of biotissue optical properties. The breadth of information available in the microwave frequency range is currently the most appropriate resource for THz researchers interested in biotissue optical properties, but mathematical extrapolation of data is required. As more THz researchers embark on biologically inspired research involving biotissue, more data will be generated, eventually contributing towards the establishment of a diverse and reliable database similar to that compiled by microwave researchers.

Chapter 10

Conclusion and Recommendations

THIS Chapter brings together the conclusions from the work described in this Thesis, and recommends directions for future work that extends the overarching theme of this Thesis, which is improved understanding of biotissue through THz spectroscopic studies, with the aim of broadening the application of THz in medicine.

10.1 Introduction

The conclusions in this Chapter are drawn from Chapters 1–9. Recommendations for future work arise from Chapters 5–9 as well as four preliminary studies presented in Appendix A.

10.2 Thesis Conclusions

The conclusions presented in this Section are derived from Chapters 1–9, and are provided as follows in order of the Chapters.

10.2.1 Review of Terahertz Systems

The wide variety of THz systems are introduced and discussed in Chapters 1–3. The range of frequencies considered in this Thesis as being in the THz band is defined as well as illustrated in Chapter 1. An in-depth review of the historical landscape of THz technology is provided in order to appreciate the development of modern THz systems used to generate results for this Thesis. Terahertz systems that vary significantly from those utilised in this Thesis, such as those for astronomical surveys, are included in the review to highlight the rich body of THz research being conducted today.

Systems that are not based on electro-optic (EO) or photoconductive (PC) THz generation are presented in Chapter 2. This group includes both continuous wave (CW) and pulsed THz systems that vary considerably in terms of their sizes, types of hardware used, types of THz generation and detection techniques utilised, and their real-world applications. Smaller systems, such as quantum cascade lasers (QCLs) and backward-wave oscillators (BWOs), are gaining popularity in THz research laboratories despite their lack of frequency tunability (QCLs) and narrow bandwidth (BWOs). Although significantly larger systems, such as synchrotrons and free electron lasers, may not be easily accessible worldwide, they are becoming in integral part of the THz research landscape in countries where they are available.

Systems that do rely on EO or PC THz generation are introduced in Chapter 3. Since these systems are used in the generation of results in this Thesis, a significant portion of this Chapter is devoted to explaining the underlying principles of optical rectification of crystals with second order nonlinearity, and transient photoconductivity. Since

EO and PC THz generation hinges on the generation and detection of subpicosecond pulses, this Chapter also includes a thorough review of the development of this technology over the past 4 decades. Furthermore, auxiliary optical hardware required by both EO and PC THz systems are briefly described to provide a holistic understanding of these systems.

10.2.2 Review of Medical Spectroscopy

Given the multidisciplinary nature of this Thesis, a review of medical spectroscopy and imaging research in the THz, IR, and microwave frequency regimes is introduced in Chapter 4—this is included because medically-inspired THz research is still in its infancy when compared to the medically-inspired IR and microwave research. There is much to be gained from reviewing past and present IR and microwave work because IR and microwave measurement techniques, as well as data, can often be adapted or expanded for use in the THz range; this becomes evident later in Chapter 9.

Since many bodies of THz, IR and microwave work involve identifying the unique spectral features of samples under investigation, Chapter 4 includes a discussion of spectral fingerprints, and provides key spectral identifiers of group frequencies in the IR range. This discussion aims to highlight the rich complementary information that can be obtained in the IR frequency range, which when used together with THz spectroscopy, can provide both the group and fingerprint information of a sample.

In conjunction with the introduction of salient medically related IR and microwave research in Chapter 4, parallel work in the THz field, including the original contributions of this Thesis, are presented. Since a large number of medically inspired THz research involves samples in liquid or moist environments (e.g. biomolecules in solution, biotissue), the influence of liquid water and water vapour are discussed in this Chapter. In addition, techniques employed in THz liquid spectroscopy are highlighted. Finally, work done by other authors relating to THz spectroscopy of fresh and formalin-fixed biotissue is introduced.

10.2.3 Experiments: Analysis of Biotissue Hydration

Terahertz measurements of biotissue has in the past involved formalin-fixed or cooked samples. More recently, freshly excised biotissue is favoured because they are more

similar to *in vivo* conditions. However, the high moisture levels in fresh biotissue complicates handling and THz measurements. Chapter 5 provides a thorough study of how hydration levels in freshly excised biotissue influences THz measurements. In doing so, handling and storage protocols that are lacking in existing literature are elaborated on. In light of the handling and measurement difficulties of freshly excised biotissue, Chapter 5 proposes a possible storage technique that preserves the integrity of the sample.

Prior to presenting the measured THz data, Chapter 5 elaborates on how THz data is collected and processed. The same data collection and processing technique is utilised in Chapters 5–8, and in Section 10.3.8. Definitions, such as system bandwidth and dynamic range, are given. This is then followed by detailed description of the sample preparation techniques.

Results from fresh biotissue measurements show that it is easy to misinterpret data due to high water content in the samples. Furthermore, measurements in a nitrogen-purged environment causes the fresh biotissue to dehydrate over time, resulting in variations in the measured THz data. One alternative to fresh samples is proposed in the form of lyophilised biotissue. Lyophilisation avoids problems arising from variability in hydration, thickness, freshness and structure. Additionally, lyophilised biotissue samples are easier to handle and mount than supple fresh ones. Lyophilisation is therefore a viable option for THz spectroscopic studies of biotissue.

10.2.4 Experiments: Differentiating Health of Biotissue

The handling and measurement challenges posed by freshly excised biotissue warrants exploration of other types of preparation techniques that preserve the integrity of the biotissue. Lyophilisation introduced in Chapter 5 is one possibility, snap-freezing is another. Chapter 6 presents a study that utilises snap-frozen human brain tissue to achieve two aims: *(i)* to investigate if snap-frozen healthy and diseased snap-frozen brain tissue can be distinguished using THz spectroscopy given that the measured signal is less affected by attenuation by water, and scattering from large ice crystals; and *(ii)* if distinction between healthy and diseased tissue types is possible, then to determine the cause(s) of the distinction.

In order to understand the diseased tissue under investigation, this Chapter includes a background into the type of disease afflicting the tissue: Alzheimer's disease (AD);

this background is salient to both Chapters 6 and 7. An explanation is also given with regards to how the human tissue is obtained for this study, including accompanying pathological reports.

The experiments conducted in this Chapter draw from experience gained from the study of fresh and lyophilised biotissue in Chapter 5. Tissue handling and storage protocols are established to ensure the integrity of the samples. Experimental protocols are also developed for measuring the samples in a cryostat; issues such as the pros and cons of vacuum evacuation of the cryostat are discussed.

Terahertz spectroscopic measurements of the healthy and diseased samples show some distinction in the THz absorption spectra of the two types of samples, which could be attributed to pathological changes in the diseased tissue. However, the difference in gradients between the THz absorption coefficient plots of healthy and diseased tissue is the only distinguishing feature. Visual examination of the diseased tissue reveal tissue atrophy, which may contribute towards the observed difference between the two groups of THz absorption spectra. Furthermore, the presence of blood vessels in both sample types may scatter THz radiation.

These early results are encouraging but many challenges and uncertainties need to be overcome before more conclusive statements can be made about the feasibility and reliability of using THz spectroscopy to distinguish between healthy and diseased brain tissue. The challenges are discussed in detail in Section 6.5.1, including suggestions for future work. A summary of these suggestions are provided in Section 10.3.2.

10.2.5 Experiments: Differentiating Microstructures in Gels

In Chapters 5 and 6, the use of whole biotissue samples creates many challenges to producing consistent and repeatable THz measurements. When compared to simple biomolecules such as proteins (measured in powdered form), biotissue is extremely complex, consisting of several sub-systems of proteins, lipids, water, *etc*. The collective responses of these sub-systems are sensed in THz spectroscopy, making it difficult to isolate the influence of a specific sub-system of biotissue. Given that one aim of this Thesis is to sense the pathogens of Alzheimer's disease, Chapter 7 narrows the focus down to one of the alleged pathogens of Alzheimer's disease: protein plaques. The unique β-pleated structure of protein plaques is one of its most distinguishable

features, thus this Chapter investigates whether this biological microstructure can be differentiated using THz spectroscopy.

Two types of biological microstructures are synthesised in this study: fibrillar ones similar to those in diseases such as Alzheimer's disease and type II diabetes, and globular ones. Both microstructures are synthesised from β-lactoglobulin (β-lg), a by-product of whole bovine milk. When β-lg is heated above 65–70°C in a solution environment, microstructures of different shapes can be synthesised depending on the acidity of the solution environment. In this study, synthesis at pH 2, 4 and 7 result in microstructures that are fine fibrillar, globular, and coarse fibrillar respectively. Details of their synthesis are given in detail in Chapter 7. Furthermore, the presence and shape microstructures are verified using standard dyes and electron micrography (both transmission and scanning).

In order to overcome the strong attenuation of liquid water, all samples in this study are measured in the frozen state. To ensure that water activity does not interfere with the measurements, the samples are measured at 123 K (-150°C). The THz optical properties of the three types of microstructures are plotted and compared to show a strong distinction between the fibrillar and globular samples, but no distinction between the two types of fibrillar samples. The results are verified with Rayleigh models of cylinders and spheres with similar dimensions to those in the samples.

The results presented in Chapter 7 are promising because both fibrillar gels have β-pleated sheets resembling those in diseases involving amyloid-β fibrils, such as Alzheimer's disease. This means that it is possible to use THz spectroscopy to identify amyloid-β fibrils in brain tissue if the tissue is devoid of blood vessels and other granular matter, such as homogenised tissue. The results also suggest that other diseases, such as type II diabetes, may benefit from the development of a THz spectroscopic diagnostic tool.

10.2.6 Experiments and Modelling: Scattering from Cylinders

In Chapters 6 and 7, isolating proteins in whole tissue through homogenisation is proposed as a means of ensuring composition uniformity in a sample. The fibrillar structure of the proteins of interest, namely amyloid-β fibrils, have been shown to have distinct THz optical properties. Before embarking on homogenising more donor tissue, it is useful to first gain an understanding of how THz radiation interacts with

these fibrillar structures. Characterising the scattering and transmission profiles from fibrillar structures is the focus of Chapter 8.

In Chapter 7, the random orientations of synthesised fibrillar structures in the form of gels can only be observed at present using electron microscopy. To simplify the study of these fibrillar structures, cylindrical fibreglass strands with subwavelength diameters are used as an alternative, whereby the orientation of the strands can be easily manipulated. The dimensions of the strands also allow them to be practically modelled using a numerical solver, such as the High Frequency Structure Simulator (HFSS) software.

A periodic array of fibreglass strands is created by orientating all the strands in the same direction, and securing their tips to a frame. The array is then orientated either parallel to or perpendicular to the incident THz electric field, and measured using THz spectroscopy. The array is modelled in HFSS and the simulation results compared with the measurements. Both the measurements and the HFSS simulations show that the optical properties of the array changes with orientation. In addition, the HFSS simulations allow visualisation and quantisation of the electric field distribution caused by the presence of the array in both orientations, providing an extra dimension of information which would otherwise be lacking in transmission-mode THz-TDS experiments.

Although the HFSS software has been useful to this study, several precautions are needed when using it. To achieve accurate and valid simulation results, the user needs to be aware in advance of what test parameters are appropriate, and of the HFSS software's inherent limitations. Checks are performed in this study to ensure that the results from HFSS agree with those from analytical (exact) solutions.

10.2.7 Modelling: Propagation and Scattering from Layers

In Chapter 8, the Mie analytical model was used in the attempt to verify THz measurements. The analytical model was shown to be limited, whereas a commercial full-wave numerical solver was shown to be more successful at modelling the test scenario. Although the analytical model did not perform satisfactorily in Chapter 8, in many instances analytical and numerical models can perform as well, if not better, than full-wave simulators. Furthermore, the licensing cost of commercial full-wave simulators,

plus their steep learning curve, may limit their effectiveness for studying electromagnetic phenomena. Chapter 9 presents a study that utilises exact solutions to verify THz transmission and reflection measurements from a stratified environment.

Since one focus of this Thesis is the investigative use of THz spectroscopy in Alzheimer's disease diagnosis, the human head is the stratified environment under study. The impedance model from transmission line theory is used in Chapter 9 as the technique for modelling THz propagation and reflection in the head. Past studies by other authors have shown THz reflections from the surface and underlying layers of skin, therefore this study aims to explore if reflections can be reliably detected from layers of tissue located underneath skin. Furthermore, as this study involves only mathematical modelling, the modelled results are compared against THz skin measurements conducted by other authors.

In order to construct the mathematical model, THz optical properties from various biotissue types are required. Due to the lack of reported data in THz literature, microwave data is sourced and extrapolated into the THz frequency range using the 4-term Cole-Cole model. Where THz data exists, the range of THz frequencies covered is usually small, requiring interpolation of both microwave and THz data sets to provide optical properties for the missing THz frequencies.

Results from the model agree well with the THz measurements from other authors. For the tissue layers located deeper inside the head, strong attenuation of the THz signal occurs as expected given the high water content of biotissue. However, this study reveals reflections, which correlate well with calculated propagation and reflection times. A feasibility analysis of power levels reveal that the signal strength of these reflections are small and cannot realistically be detected given present THz input power levels. With future improvements to THz power levels, detection may be possible but safety concerns will need to be addressed.

10.3 Recommendations for Future Work

This Section presents recommendations for extending the work in Chapters 5–9. In addition, four preliminary studies in various stages of development are summarised in this Section. These four studies are described in more detail in Appendix A.

10.3.1 Biotissue Hydration

One issue encountered in Chapter 5 is the formation of cracks in a few lyophilised samples. Further investigation is needed to explore optimal lyophilisation durations for specific biotissue types and if possible, quantify biotissue hydration. Monitoring changes in sample weights before and after lyophilisation (as well as before and after THz measurements) may be a good technique for tracking biotissue hydration.

Reconciling THz spectra with biotissue histology is another future work. Histological studies tend to be conducted using formalin fixed samples mounted on microscopic slides. To incorporate formalin fixed samples into this study, samples will need to be divided into four: fresh, lyophilised, necrotic and fixed. When improved lyophilisation techniques are established so that good and consistent quality lyophilised biotissue are produced, then lyophilised biotissue can be compared with confidence against formalin fixed samples.

10.3.2 Differentiating Health of Biotissue

To overcome handling issues and the poor physical condition of the diseased brains in Chapter 6, it may be more feasible to lyophilise the samples prior to measurements. Lyophilised samples can then be measured at -80°C (193 K) *in vacuo*.

Another possible future work is to isolate the protein plaques in the diseased tissue by homogenising it. This process involves grinding and centrifuging whole brain tissue in order to isolate the different components of the tissue, particularly protein plaques. This process will aid in removing blood vessels, tissue and other particulate matter which may have interfered with the results in this study. The disadvantage of homogenisation is that large quantities of brain samples are needed. Since the availability of donor brain tissue is a concern, it may be necessary to work with other researchers who work with homogenised brain tissue (e.g. RNA researchers), whereby the homogenised tissue is first examined non-destructively with THz spectroscopy.

The isolation of protein plaques raises the question of whether synthetic versions of the protein can be studied with THz spectroscopy. This has led to the study in Chapter 7. As a final note, a feasibility study of *in vivo* brain scanning using continuous wave (CW) THz radiation has been proposed in Bakopoulos *et al.* (2008) and Bakopoulos *et al.* (2009). The use of a monochromatic THz source at an optimal THz frequency that

is less affected by water absorption (e.g. < 0.5 THz) may potentially be the solution to overcoming issues with water absorption in human tissue.

10.3.3 Differentiating Microstructures in Gels

One possible extension of the work presented in Chapter 7 is the refinement of sample preparation and spectroscopic techniques (e.g. THz microscopy) in order to distinguish between fibrillar structures with different diameters. This would allow identification of different types of amyloid fibrils, allowing the study of some of the triggers that lead to the various manifestations of amyloid fibrils.

Another potential extension of this work is the morphological study of highly cytotoxic granular protein aggregates with THz-TDS. These granular protein aggregates can form fibrillar aggregates that are classified as amyloid fibrils, which are associated with Alzheimer's disease. This would provide another means of utilising THz spectroscopy to understand the triggers that cause apparently healthy protein aggregates to misfold into undesired structures.

10.3.4 Scattering from Cylinders

The study presented in Chapter 8 is the first step in understanding the interaction of THz radiation with fibrillar structures. Measurements and simulations of cylinders with narrower and wider diameters should be explored. Cylinders arranged in mixed orientations should also be investigated as this will more closely resemble the fibrillar microstructures in amyloid-β fibrils.

One potential extension of this work is to the investigate spheres. A model containing a periodic array of spheres would simulate powders and other spherical scatterers commonly encountered in THz experiments. Another potential extension of this study is to explore THz scattering from surfaces, such as walls and skin. The influence of surface roughness in the THz regime would be interesting in the realm of THz communications and medically-inspired THz applications.

Other three dimensional full-wave numerical solvers, such as COMSOL and MMP may be more appropriate for modelling structures such as the periodic arrays presented in Chapter 8, hence these other solvers could be used in parallel with HFSS to produce complementary results.

10.3.5 Propagation and Scattering from Layers

In order to improve the accuracy of the model presented in Chapter 9, and to be able to conduct a more realistic safety analysis of increased THz power levels, direct measurements of the THz optical properties of biotissue are required. Furthermore, the assumption made in this study is that all the biotissue layers modelled are homogeneous and flat. An extension of this study is to include heterogeneity and structure, such as surface roughness. More rigorous propagation models should also be investigated. One possible model, the pseudospectral time domain (PSTD) algorithm, is proposed in Section 9.7.1. Another model involving the field of inverse problems is discussed in Appendix A.

10.3.6 Preliminary Study 1: Pseudo-Phase Contrast

In keeping with the aim of this Thesis, which is to broaden the application of THz in medicine, this study presents an alternative visualisation technique for presenting THz data. This visualisation technique may be more familiar and useful to professionals from industry and medicine.

Phase contrast is an optical method that enables the recovery of a specimen's phase information by interfering two beam paths. It is a method commonly used in optical microscopy. This study, which is presented in Appendix A, is inspired by the phase contrast method. It manipulates the time-domain amplitudes of the measured signals so that the samples' thicknesses provide the contrast in the final rendered spatial image. Since this study does not utilise phase contrast in its true sense, but is only inspired by it, this study is therefore called 'pseudo-phase contrast'.

10.3.7 Preliminary Study 2: Polymer Hole Arrays

As seen in Chapter 7, one possible contribution towards improved understanding of biotissue through THz spectroscopic studies is the study of simpler bio-markers in btisb, such as proteins and lipids. When extracted from a living body through routine blood tests, the quantity of these biological markers tend to be minute—in the order of micrograms. This study, which is presented in Appendix A, explores if a sample holder consisting of a periodic array of holes is suitable for detecting minute quantities of liquids.

10.3.8 Preliminary Study 3: Etalon Removal

This study, presented in Appendix A, aims to improve the signal processing of THz measurements made from samples enclosed in holders that contribute towards Fabry-Pérot etalon effects, such as the polystyrene culture dishes used in Chapter 7. An algorithm is proposed, and preliminary results are presented so as to compare the performance of this proposed algorithm with that from existing literature.

10.3.9 Preliminary Study 4: Inverse Problems

The scattering issues encountered in this Thesis tend to be inverse ill-posed scattering problems. The use of the Tikhonov regularisation is proposed in this study to solve such problems. This study, which is presented in Appendix A, will also be beneficial for studying scattering from rough surfaces that may be encountered in THz biotissue studies.

10.4 Summary of Original Contributions

The original contributions of this Thesis were highlighted in Section 1.7 in the Introduction Chapter. These key contributions are summarised as follows:

1. Terahertz spectroscopy of fresh biotissue. Experimental studies are conducted for the first time to explore the impact of hydration and storage issues on THz spectroscopic measurements of freshly excised biotissue. These experiments reveal the susceptibilities of THz biotissue measurement to changes in environmental conditions and measurement duration, highlighting the need for storage and handling protocols in the area of THz biotissue measurements (Png *et al.* 2008a).

2. Terahertz spectroscopy of snap-frozen biotissue for the purpose of distinguishing between healthy and Alzheimer's disease-afflicted human brain tissue. Experiments involving snap-frozen human brain tissue is presented for the first time, with the novel aim of distinguishing between healthy and Alzheimer's disease-afflicted samples. Results show some distinction between the two sample types, but this distinction cannot be attributed conclusively to the disease-causing proteins in the diseased tissue because of the typically poor condition of diseased

donor brains (Png *et al.* 2009c, Png *et al.* 2009b). Isolation of the disease-causing proteins is one alternative, but at the expense of requiring larger quantities of donor tissue.

3. Terahertz spectroscopy and differentiation of synthesised proteins with soft microstructures. Proteins synthesised to have similar microstructures as naturally occurring proteins associated with Alzheimer's disease is one option to overcoming the need for more donor biotissue. Novel experiments are conducted on proteins with fibrillar and globular soft microstructures suspended in the frozen state. Results show that THz spectroscopy can be used to non-destructively differentiate between the two types of microstructures. These results are verified with analytically Rayleigh models of cylindrical and spherical scatterers (Png *et al.* 2009a).

4. Terahertz spectroscopy and full-wave electromagnetic modelling of fibrillar (cylindrical) scatterers. Novel experiments are conducted on structures containing nearly periodic arrays of fibreglass strands with subwavelength diameters (Png *et al.* 2008b). Mutual coupling between the closely-proximated adjacent strands is expected, but cannot be modelled using conventional analytical models. Novel numerical models are developed on a full-wave electromagnetic solver to elucidate the experiments, particularly how orientation of the cylinders influence scattering.

5. Modelling THz propagation through stratified heterogeneous media. This novel study utilises a simple yet effective analytical model to elucidate THz propagation, which aids in the determining the plausibility of conducting *in vivo* THz sensing of diseased biotissue located several millimeters beneath the skin (Png *et al.* 2005b, Png *et al.* 2005a, Withayachumnankul *et al.* 2007).

6. Four preliminary studies are presented in Appendix A to extend the novel work presented in this Thesis. Preliminary results and reviews from these studies aim to improve the extraction of information from THz measurements (Png *et al.* 2004), and to improve the modelling of THz propagation and scattering from biotissue.

10.5 Chapter Summary

This Chapter has provided an overview of the major conclusions of this Thesis. Recommendations for future work are also included. As summarised in this Chapter, this Thesis has made major, novel contributions to improving the understanding of biotissue through THz spectroscopic studies, broadening the application of THz in medicine and providing directions for further contributions to THz science.